ISBN: 978-94-92323-99-6

ELECTRONS, PHOTONS, & THE TIME IN BETWEEN

NIKA VAN NIELEN

ELECTRONS, PHOTONS, & THE TIME IN BETWEEN

PROBING MATERIALS THROUGH PUMP-PROBE CATHODOLUMINESCENCE IN AN ULTRAFAST SEM

NIKA VAN NIELEN

INVITATION
to the public defence and reception of the doctoral thesis

ELECTRONS, PHOTONS, & THE TIME IN BETWEEN

by
NIKA VAN NIELEN

Date
Wednesday, February 25th 2026
at 10.00 am

Location
Agnietenkapel
Oudezijds Voorburgwal 231,
1012 EZ Amsterdam

Paranymphs
Evelijn Akerboom
&
Hollie Marks

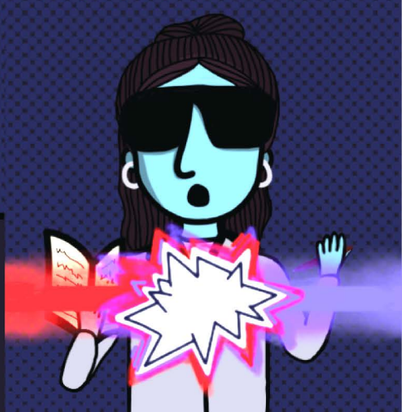

ELECTRONS, PHOTONS, & THE TIME IN BETWEEN: PROBING MATERIALS THROUGH PUMP-PROBE CATHODOLUMINESCENCE IN AN ULTRAFAST SEM

Ph.D. Thesis, University of Amsterdam, February 2026
Electrons, photons, & the time in between: probing materials through pump-probe cathodoluminescence in an ultrafast SEM
Nika Juanita van Nielen

Cover: Comic style illustration of the dark, ultrafast SEM lab, featuring one laser path triggering the electron microscope cathode, another coupled into the SEM chamber, and the operator at work.

ISBN: 978-94-92323-99-6

This work is part of the research program of the Dutch Research Council (NWO). This project has received funding from the European Research Council (ERC) under the European Union's Horizon 2020 research and innovation program, Grant Agreement No. 101019932 (Quantum Electron Wavepacket Spectroscopy (QEWS)) and Grant Agreement No. 101017720 (Electron Beams Enhancing Analytical Microscopy (eBEAM)).

A digital version of this thesis is available at https://ir.amolf.nl.

ELECTRONS, PHOTONS, & THE TIME IN BETWEEN: PROBING MATERIALS THROUGH PUMP-PROBE CATHODOLUMINESCENCE IN AN ULTRAFAST SEM

ACADEMISCH PROEFSCHRIFT

ter verkrijging van de graad van doctor

aan de Universiteit van Amsterdam

op gezag van de Rector Magnificus

prof. dr. ir. P.P.C.C. Verbeek

ten overstaan van een door het College voor Promoties ingestelde commissie,

in het openbaar te verdedigen in de Agnietenkapel

op woensdag 25 februari, te 10.00 uur

door Nika Juanita van Nielen

geboren te Leiden

Promotiecommissie

Promotor:	prof. dr. A. Polman	Universiteit van Amsterdam
Copromotor:	dr. S. Meuret	CEMES-CNRS
Overige leden:	prof. dr. P. Schall	Universiteit van Amsterdam
	dr. S.A. Mann	Universiteit van Amsterdam
	prof. dr. K. Keune	Universiteit van Amsterdam
	prof. dr. J.P. Hoogenboom	TU Delft
	dr. J. Lähnemann	Paul Drude Institute, Berlin

Faculteit der Natuurwetenschappen, Wiskunde en Informatica

CONTENTS

1

INTRODUCTION

Glass is transparent, metal is reflective, and the sky is blue. At first, the material world would appear straightforward, however, none of these observations are trivial. To truly understand the age-old question of why the sky is blue requires an understanding of Rayleigh scattering[1], which describes how the scattering cross-section of sub-wavelength particles is strongly dependent on wavelength[2], with shorter (blue) wavelengths scattering more efficiently than longer (red) wavelengths. The same laws of electromagnetism also define the field of nanophotonics, the study of nanoscale light-matter interactions. Small variations in geometry on the order of nanometers can drastically affect a materials' optical response. These properties have been harnessed unintentionally for centuries, as in the case of stained glass windows whose colours are a result of light absorption and scattering from embedded metal nanoparticles. Today, we can intentionally exploit these properties, applying them to highly relevant technologies such as lighting, lasers, sensors, photovoltaics, and electronics on the basis of both plasmonic [3] and, as is of particular interest in this thesis, semiconductor nanomaterials [4]. Yet as our devices shrink and our performance demands grow, we face increasing bottlenecks and sensitivity to defects in our materials, that necessitate the study of further advanced semiconductor systems and fabrication methods. At the heart of these efforts sits microscopy, a way to measure the physical processes governing these materials and revealing phenomena that are all far from trivial.

Besides the imaging of microstructures, optical microscopy is a versatile platform for probing various material properties, that can be selected using different detection schemes and the properties of the illuminating light. Techniques such as absorption and reflection, luminescence spectroscopy, Fourier space imaging, and Raman spectroscopy can be used to study chemical composition, electronic band-structure, emission directivity, optical and vibrational modes, and more. These measurements are ultimately linked to the refractive index of the material, that is central to why different materials interact with light so differently. Glass has a

smooth surface leading to minimal scattering at the interface, and the insulating nature means that light in the visible wavelengths doesn't have enough energy to excite electrons into the conduction band, leading to minimal losses and transparency of glass. In contrast, metals are effective conductors with a sea of free electrons in the material, that can oscillate in response to incident electromagnetic fields, and re-emit that energy as light. While these are powerful measurements to understand the properties of materials, the spatial resolution of conventional optical microscopy is fundamentally limited to approximately half the wavelength of light used in the medium, typically on the order of hundreds of nanometers[5]. This so-called diffraction or Abbe limit is insufficient to characterize many modern materials, such as probing quantum confined nanostructures, although several advanced optical techniques have been able to beat this limit in some systems, notably stimulated emission depletion microscopy[6] and scanning probe microscopy[7].

Alternatively, accelerated electron beams used in electron microscopy also enable the study of matter with high spatial resolution. The de Broglie wavelength of an electron at 20 keV is < 0.1 Å, however, in practice the spatial resolution of electron microscopes (0.5 - 300 keV) is restricted by electron optics and beam abberations[8], resulting in sub-nanometer and nanometer spatial resolutions for transmission electron microscopes (TEMs) and scanning electron microscopes (SEMs) respectively. When a swift electron interacts with a material, as depicted schematically in Figure 1.1, it gives rise to distinct signals that are the basis for different imaging techniques. For sufficiently thin samples, as studied in TEMs, electrons transmitted through the sample can be used to reconstruct real and reciprocal space images of the atomic structure, or measure electron energy loss spectra (EELS) to quantify electron-excited transitions in the material. In SEMs, inelastic interactions at the sample surface generate secondary electrons (SE) that are used to image surface morphologies. Elastic scattering produces back-scattered electrons (BSEs), sensitive to atomic mass and used to measure material composition, and the crystal structure through electron back-scatter diffraction (EBSD). A complementary signal that is emitted is cathodoluminescence, that forms a powerful bridge between electron and optical microscopy.

1.1. CATHODOLUMINESCENCE MICROSCOPY

Cathodoluminescence (CL) is the light that is emitted into the far-field when a material is excited with a swift electron. It was first observed in the late 19$^{\text{th}}$ century, when electrical currents in vacuum tubes produced so called "cathode rays", leading to the discovery of the electron[9]. Throughout the 20$^{\text{th}}$ century, cathode ray tubes were commercialized and widely utilized in TV displays, and later adopted as a research tool in the fields of geology, for the characterization of mineral samples[10, 11], and semiconductor science[12, 13]. With the advances in electron microscopy and nanophotonics, CL has become a ubiquitous method to study light-matter interactions at the nanometer scale. This technique effectively enables optical microscopy methods, such as the study of photon statistics ($g^{(2)}(\tau)$)[14],

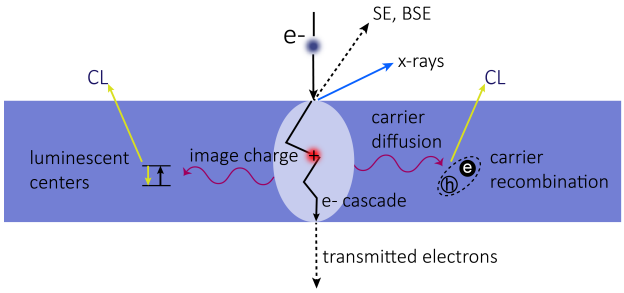

Figure 1.1: Schematic of electron-matter interactions upon electron irradiation of a semiconductor material. The incoming electron beam inelastically scatters as it propagates through the material, exciting bulk plasmons that decay into a cascade of charge carriers. These carriers can diffuse and recombine directly or through a radiative defect producing cathodoluminescence. Simultaneously, the incident electron annihilates with its image charge generating transition radiation. The electron beam can be transmitted through the sample, allowing for EELS or (S)TEM measurements, or generate secondary electrons as well as back-scattered electrons that can be used to study surface morphology.

time-resolved luminescence[15], temperature[16], phase[17], and polarization- and energy- resolved Fourier microscopy[18, 19], with the spatial resolution of the electron beam. Cathodoluminescence emission is commonly divided into two subcategories, coherent and incoherent depending on whether or not the emitted light has a fixed phase in relation to the incident electron beam.

1.1.1. COHERENT CL

Coherent emission is excited as a result of the polarization of a material in response to the electric field of the swift electron, and thus has a fixed phase in relation to the incident electron beam[20]. Importantly, coherent CL is analogous with photon-induced near-field microscopy (PINEM), as the electron probes near-field excitations that lead to the loss, gain, or emission of photons[21, 22]. Coherent CL is an umbrella term for a wide range of different emission mechanisms, one of which being transition radiation (TR). TR is emitted whenever an electron crosses the boundary between two media[23]. It can be understood as the annihilation of the electron with it's effective image charge in the metal that creates an effective dipole, and leads to far-field radiation with a dipolar emission pattern.

Another major source of coherent CL is the excitation of surface plasmon polaritons (SPPs), propagating electromagnetic waves confined to the metal-vacuum interface. The excitation of SPPs using light requires the use of phase matching techniques such as diffraction gratings or prisms, due to their momentum mismatch with light in free space. In contrast, the tight confinement of the electric fields carried by the electron in both space and time, contain broadband Fourier components[24] that can directly couple to SPPs, and resonant transitions in both plasmonic and dielectric nanostructures[25, 26]. In this case, the electron beam does not need to impinge the material directly, but can polarize it in an aloof configuration. A further example of this is Smith-Purcell radiation, that is generated

by an electron beam grazing a periodic grating[27, 28]. The interference of dipole-like emission from each grating element leads to radiation with a strong angular and wavelength dependence. The signature for coherent CL is the ability of these sources of CL emission to interfere, a property that has opened a pathway towards CL tomography for nanoscale metrology[29].

1.1.2. INCOHERENT CL

Incoherent CL has no fixed phase relation to the incoming electron beam, as it originates from spontaneous, stochastic emission processes in the material. Here, the electron beam can be primarily regarded as a source of energy that is transferred to the material through inelastic collisions. This generates a cascade of charge carriers, in a process analogous to photoluminescence (PL) excitation, although here the free carriers and excitons are excited indirectly. The electron beam is generally understood to excite bulk plasmons in the material (oscillations of the valence electrons with energies in the 5-35 eV range, depending on the material) which subsequently decay into electron-hole pairs[30–33]. These carriers are excited above the bandgap energy of the material, and consequently thermalize to the band edge emitting excess energy through phonons in the process. Thus, although much of the incident energy from an electron beam is lost through heat, a single electron can excite multiple electron-hole pairs[34] (the carrier generation rates of electron and laser beams will be discussed further in Chapter 2). As depicted in Figure 1.1, these carriers can then diffuse through the material, and recombine leading to the emission of intrinsic bandgap radiation, or become trapped in defects or colour centres, leading to the emission of extrinsic radiative recombination [13]. Additionally, the momentum of the electron beam allows it to access forbidden transitions that are inaccessible with plane wave excitation [35].

A particularly relevant feature of incoherent CL microscopy is the high-energy of the electron beam, which enables the excitation of wide-band gap semiconductors without the need for deep-UV laser sources. Consequently, among other materials, CL has become an indispensable tool for the study of III-V semiconductors, that form the basis of many 21st century technologies.

1.1.2.i. III-V SEMICONDUCTORS

Compound semiconductors composed of group III (Al, In, Ga) and group V (N, P, As) elements of the periodic table are key semiconductor materials powering modern technology, second only to silicon. Many III-Vs possess highly sought after features, including direct bandgaps, enabling efficient light absorption and emission, bandgap tunability through the infrared to UV spectral ranges, and high carrier mobilities, enabling fast (opto)electronic devices[36]. Together these properties make III-V semiconductors central to applications ranging from light-emitting diodes, lasers, solar cells, and photodetectors, to, importantly, the field of power electronics. Silicon transistors have limitations in performance for some applications as computing devices continue to shrink, due to effects of temperature and high-voltage operation[37]. In contrast, the high III-V mobility can help overcome

these issues[38]. Modern devices are composed of sophisticated heterostructures, for example photonic crystals, quantum dots, quantum wells, that can further be integrated into microrods, improving performance but increasing device complexity and sensitivity to defects.

Together with electron-beam induced current (EBIC) analysis, CL microscopy has the unique ability to both excite wide-bandgap III-V materials, and probe them at nanometer spatial resolution. This provides a means to directly identifying defects such as dislocations, stacking faults, point defects, strain variations, and the characterization of the heterostructure interfaces[34, 39, 40]. Steady-state CL provides valuable information on the spatial distribution of the material properties, but ultimately the device performance depends on dynamic processes. Understanding how carriers are generated, diffuse, trapped, and recombine in time motivates the use of time-resolved CL (TR-CL).

1.2. TIME-RESOLVED CL MICROSCOPY

The measurement of dynamic material properties with CL can be done in several different ways: in a continuous electron excitation regime using measurements of the second order autocorrelation function, $g^{(2)}(\tau)$[41, 42], or in a pulsed excitation regime using streak cameras that enable multi- and single- shot measurements[43], or using time-correlated single photon counting (TCSPC) to build an arrival time histogram by correlating the detection time of the CL on a photodetector with the known excitation time of the sample. In all these approaches, the recombination dynamics of excited carriers are measured. The radiative decay rate, γ, and corresponding decay lifetime, τ, are determined by the oscillator strength and the local density of optical states (LDOS). In practice, the effective lifetime is limited by non-radiative recombination processes, that depend on the trap density, trap cross-section, and carrier mobility.

Measuring the lifetime as a function of position on the sample can map the material quality, as regions with defects typically exhibit a shorter effective lifetime due to the increased contribution of non-radiative recombination channels. In practice, the rate equation model describing CL emission is much more complex than described above and has to be tailored to the material studied. For instance, samples with multiple emitters could result in a decay described by a sum of exponentials with different lifetimes, while disordered materials would exhibit a stretched exponential distribution[44]. It is also important to account for carrier generation and transport within a material, which can influence the dynamics and necessitate that drift-diffusion equations are included into the model[45]. In doped semiconductors, it may be important to distinguish the rate equation for minority and majority carriers. As some recombination mechanisms scale nonlinearly with carrier density, such as monomolecular (trap-assisted), bimolecular (near-band edge), and Auger (three-body) recombination[46], it is important to consider the impact of excitation density on recombination. Furthermore, effects such as defect density, defect saturation, and photon recycling may need to be considered as well[47–49].

Hence, TR-CL can capture the dynamics of a wide range of different recombi-

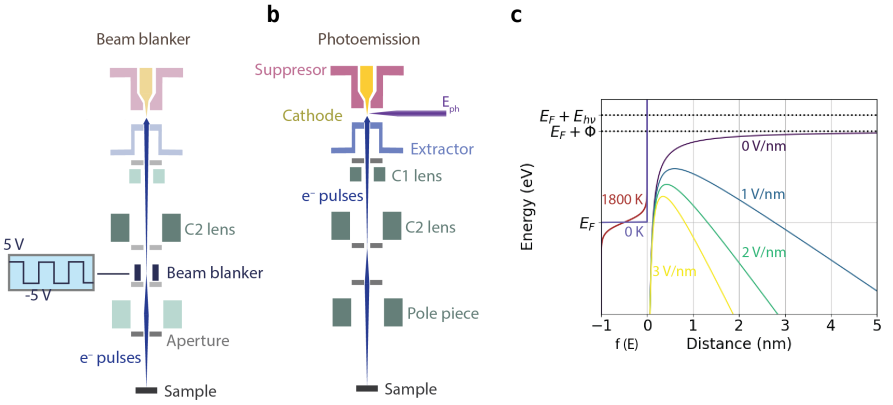

Figure 1.2: Schematics of pulsed electron beam generation techniques, adapted from [53]. (a) Electron pulse generation using an electrostatic beam blanker. The electron beam is focused between the blanking plates by adjusting the voltage of the second condensor lens (C2). A square wave voltage pulse is applied across the plates, deflecting the electron beam across an aperture inserted below the pole piece. (b) Electron pulse emission using photoemission. A pulsed laser beam is focused onto the electron cathode of the microscope, generating electron pulses. (c) Graph plotting on the left side, the Fermi-Dirac distribution of electrons at 0 and 1800 K. The electron energy barrier as a function of distance to the cathode/vacuum interface in the presence of different applied external electric fields. Figure adapted from ref [54].

nation processes and is an important tool for (semiconductor) material characterization [50–52]. Implementing TCSPC-based TR-CL in the SEM, however, requires that the electron beam is operated in a pulsed rather than continuous regime to have a precise time zero of excitation.

1.2.1. BEAM-BLANKED AND PHOTOEMISSION ELECTRON PULSES

There are two main strategies to generate a pulsed electron beam in electron microscopes, as schematically depicted in Figure 1.2.

The first strategy is beam-blanking, in which the continuous beam is chopped into pulses. This is achieved by focusing the electron beam between two electrostatic plates across which a periodically modulated voltage is applied, resulting in a periodic deflection of the electron beam. By placing an aperture below the beam blanker, the electron beam is chopped as it is swept over the aperture. This is a convenient approach as the repetition rate and duty cycle can be easily varied by tailoring the voltage waveform applied to the beam blanker, and the microscope can be readily switched between continuous and pulsed regimes. However, the temporal resolution of the electron pulses is limited by both the electronics and electron beam energy. In our system, we achieve pulse duration of about 30 picoseconds at 5keV[53] by optimizing the blanker geometry (sub-millimeter plate spacing, fast voltage edge times, and tight apertures). At higher electron beam energies, the deflection efficiency is reduced leading to pulse lengths of hundreds of picoseconds. It is worth noting that sub-picosecond electron pulses can be achieved us-

ing radio-frequency (RF) cavities and micro-electro-mechanical-systems (MEMS) deflectors[55]. However, these methods are technically demanding[56] and are rarely implemented in SEMs.

The second strategy for generating electron pulses is by photoemission, achieved by direct femtosecond pulsed laser triggering of the electron cathode. In this configuration, photon absorption excites electrons above the energy barrier of cathode, generating electron pulses. This method has been shown to generate subpicosecond electron pulses in ultrafast TEMs (UTEMs)[57–59], as well as in ultrafast SEMs (USEMs)[60, 61]. In addition to high temporal resolution, this method can generate multiple electrons per pulse, that can be interesting for studies on correlated electron number states[62], studies requiring high currents, or variable excitation densities to study non linear material properties such as carrier recombination dynamics (see section 1.2). However, due to the Coulomb repulsion between electrons in pulses containing more than one electron, this comes with a tradeoff in energy and temporal resolution.

To understand how photoemission in USEMs works, it is useful to review the physics of Schottky FEGs. USEMs are typically equipped with a zirconium oxide-coated tungsten cathode (Zr/W). The material of the cathode defines the amount of work it takes to free an electron into vacuum, i.e. the work function ϕ. In a continuous mode, the cathode is resistively heated by applying a DC current through the tip (filament current). The heating increases the thermal energy of the electrons, redistributing their energy occupation according to the Fermi-Dirac distribution f(E), as plotted in Figure 1.2 c. A fraction of the electrons have sufficient energy to overcome the work function[54]. Additionally, the presence of a strong external electric field, generated by an extractor plate about 500 μm away from the cathode, lowers the height of the potential barrier with distance via the Schottky effect and accelerates the electrons into the gun column. The potential energy of an electron at a distance z from the surface is given by[63],

$$U(z) = E_F + \phi - \frac{e^2}{16\pi\epsilon_0 z} - eFz \tag{1.1}$$

where E_F is the Fermi energy, e^2 the elementary charge, ϵ_0 the permittivity of vacuum, and F the applied external electric field. As plotted in Figure 1.2 c, increasing F from 0 to 3 V/nm reduces the effective work function and narrows its width, thus increasing electron emission not only through thermal energy but also through tunneling. In addition to the extractor plate, the electron gun also includes a suppressor electrode positioned above the cathode, biased at -500 V. Its role is to prevent electrons from being emitted along the length of the cathode and confine emission to the tip of the cathode, thereby improving coherence.

To achieve photoemission, the tip temperature is reduced to suppress continuous thermionic emission. In our microscope, this is done by decreasing the filament current from 2.41 to 1.2 V, corresponding to a tip temperature of < 1200 K[64]. However, the reduction in thermionic emission is not immediate and the tip requires on the order of an hour to cool during which the emission gradually

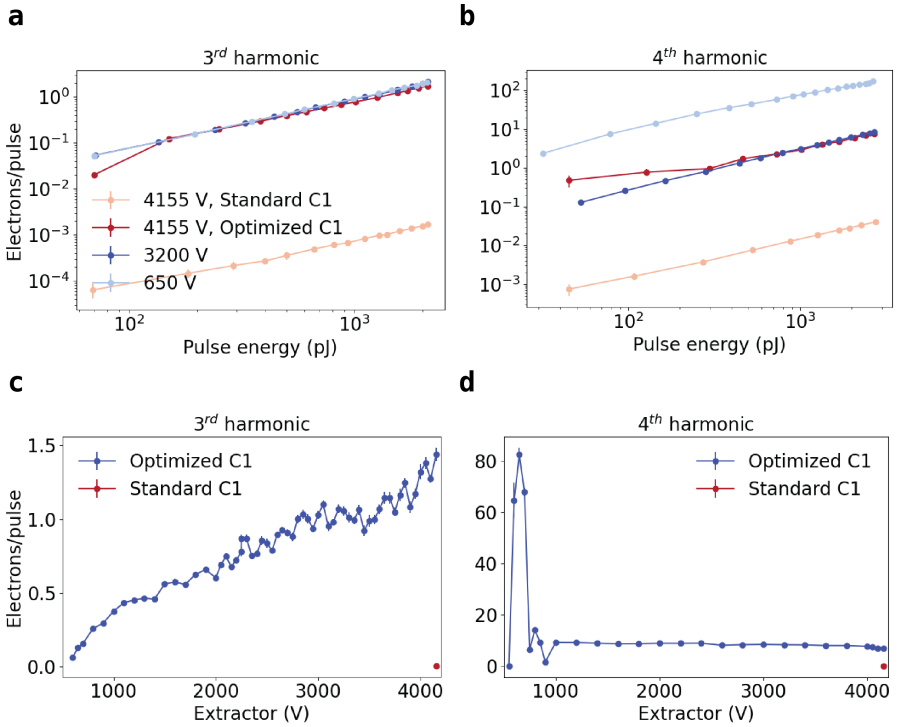

Figure 1.3: Number of electrons per pulse generated by photoexcitation of the Schottky FEG cathode with a 50 μm aperture as a function of laser pulse energy at four extractor voltage and C1 settings, for excitation with photon energies of (a) $E_{h\nu} = 3.59$ eV (3$^{\text{rd}}$ harmonic of a 1034 nm laser) and (b) $E_{h\nu} = 4.82$ eV (4$^{\text{th}}$ harmonic of a 1034 nm laser). (c) and (d) show the corresponding dependence of number of electrons/pulse on extractor voltage, measured at a fixed laser pulse energy of 2.1 and 2.2 nJ respectively.

decreases. A way to instantaneously suppress thermionic emission is to decrease the extractor voltage, increasing the effective work function. In our microscope, decreasing the extractor voltage from its nominal value 4155 V to 3200 V cuts the thermionic emission. Changing the extractor voltage requires a realignment of the gun column optics by changing the voltage of the first condensor lens (C1) and adjusting the gun shift/tilt to refocus the beam through the gun aperture and maximize the current at the sample. At a high extractor voltage of 4155 V, the current is maximized by optimizing the C1 setting from 1305 to 1100 V. At 3200 V, C1 is set to 930 V, and at a low extractor voltage of 650 V, C1 is adjusted to 530 V. In the cold-tip regime, the energy required to overcome the work function is supplied by the absorption of photons rather than thermal energy. When a femtosecond laser of photon energy $E_{h\nu}$ is focused on the cathode, synchronized ultrashort electron pulses are emitted.

Figures 1.3 a & b, show the number of emitted electron per pulse as a function of laser pulse energy for cathode excitation using the 3$^{\text{rd}}$ harmonic of a 1034 nm

laser ($E_{h\nu}$ = 4.82 eV) and 4th harmonic ($E_{h\nu}$ = 3.59 eV) respectively, measured using a 50 μm aperture for the four extractor configurations in our USEM. In all cases, the current increases linearly with laser pulse energy, consistent with single-photon absorption. For excitation with the 3rd harmonic, the limited excess photon energy above the work function results in a low emission efficiency, with only 1-2 electrons emitted per pulse. In contrast, excitation with the 4th harmonic results in significantly higher number of electrons emitted per pulse, with ~ 10 electrons per pulse at high extractor voltages. Decreasing the extractor voltage to 650 V increases the number of electrons per pulse to about ~100 electrons per pulse at the same laser pulse energies. Figures 1.3 c & d illustrate the dependence of current on extractor voltage. Exciting with the 4th harmonic, the current is constant over most of the extractor voltage range but it increases sharply as the extractor approaches 650 V. This rise is attributed to a focusing of the generated electrons through the extractor aperture as the voltage approaches the potential of the suppressor[65]. In contrast, for 3rd harmonic excitation the current decreases with decreasing extractor voltage. We attribute this to the limited excess photon energy above the work function, making emission strongly reliant on the lowering of the energy barrier by the extractor through the Schottky effect.

Thus, generating pulsed electron beams by photoemission opens the door to time-resolved electron microscopy techniques such as TR-CL, discussed earlier, as well as pump-probe microscopy.

1.2.2. PUMP-PROBE CL

Optical pump-probe experiments are a powerful, widely used time-resolved technique to investigate material dynamics. Such experiments involve the use of a short initial laser pulse to excite a sample (the pump), and a second time-delayed laser pulse to monitor the state of the excitation (the probe). By systematically varying the delay between the pump and probe, the evolution of the excitation in time is measured, with the temporal accuracy limited by the pulse lengths and the precision of their relative arrival times. Variants of pump probe, such as transient absorption, have been reliably used to study carrier dynamics in semiconductors [66, 67], phase transitions[68], and molecular vibrations[69], among many other processes. Unlike conventional time-resolved luminescence measurements, the pump-probe technique can measure ultrafast processes on femtosecond[70] or even down to attosecond time scales [71], surpassing the limits of the fastest photodetectors such as streak cameras, that achieve picosecond temporal resolutions.

Through the development of UTEM, configurations using a laser pump and electron probe have also emerged, combining the temporal resolution of the technique with the high spatial resolution of electron beams[58, 72]. Importantly, synchronization between the pump and probe beams is made possible by splitting a single laser into two paths; one path is used to photo-excite the electron cathode, while the other optically pumps the sample, thereby eliminating the need for electronic synchronization that would otherwise introduce additional timing jitter. Pioneering work used transmitted electrons to study spatially resolved magnetiza-

tion dynamics [73], defect and nanoparticle-assisted phonon modes [74, 75], lattice relaxations[76], and charge density waves[77]. Pump-probe approaches have also been implemented in USEMs, primarily through the analysis of secondary electron contrast to study photo-carrier relaxation [78–82].

Our group has developed a novel pump-probe cathodoluminescence (PP-CL) instrument based on an USEM. The instrument employs synchronized femtosecond light pulses and picosecond photoemission electron pulses, to measure the temporal evolution of the emitted luminescence signals, either PL or CL, to study material dynamics. The set-up can be used in two configurations by adjusting the delay scanning range, one where the electron is used as the pump, and one where the electron is used as a probe. In the former, where the electron is the pump, the electron charge can be exploited to induce transitions inaccessible to laser pulses, as was demonstrated by Solà-Garcia et al. in ref. [83] to measure the state conversion dynamics of diamond NV centers. The latter configuration, where the electron is the probe, can enable the exploitation of the high spatial resolution of the electron beam to measure PP-CL maps, as well as access to carrier injection regimes with laser excitation that are unachievable with the electron beam alone.

1.2.3. PHOTON-INDUCED NEAR-FIELD ELECTRON MICROSCOPY

Alternatively, rather than analyzing luminescence signals, the instrument can be used for a different class of pump-probe experiments, photon-induced near-field electron microscopy (PINEM). In this configuration, a laser pulse is used for optical near-field excitation, which is then probed by a synchronized electron pulse. In the previous sections, the electron was described as a localized, charged point particle, in contrast, PINEM exploits its dual wave-particle nature. As a consequence of interaction with the near-field, the electron coherently exchanges energy with the optical field via simultaneous stimulated emission and absorption of photons, leading to a modulation of the electron wavefunction into quantized energy sidebands spaced by the photon energy[84, 85]. Measuring the relative redistribution of the electron energy provides a direct measure of the interaction strength, that is defined by the time-varying longitudinal component of the electric near field. As a result, PINEM has been used to map the near field distribution in a variety of nanostructures[21, 58, 86–88].

Beyond near-field mapping, the electron-light interaction facilitated by the near-field enables the tailoring of the electron wavefunction. Several geometries have been explored theoretically and experimentally in UTEMs, with proposed applications in quantum communication[89] and attosecond electron pulse train generation [90–92]. The increasing complexity of such experimental configurations would benefit from the larger vacuum chamber of USEMs, compared to UTEM, so that advanced light incoupling and correlative CL measurements can be performed. In addition, access to the slower electron regime[93] can have the advantage of stronger electron-light coupling. In practice, this requires the integration of an electron spectrometer into the microscope, as will be demonstrated in Chapter 5 of this thesis.

1.3. THESIS OUTLINE

To summarize, CL is a powerful method for studying materials with the nanometer spatial resolution of the electron beam and the flexibility of optical spectroscopy. Beyond this, electron-light interaction through PINEM can be used to measure the near-field distribution of nanophotonic systems as well as restructure the electron wavefunction. The developments of time-resolved electron microscopy through beam blanking at photoemission has enabled the study of dynamic material properties, that can be further expanded by incorporating laser incoupling to perform pump-probe measurements. This thesis explores how different experimental modes of our USEM instrument can be used to study dynamic processes, with a particular emphasis on III-V semiconductors, and plasmonic and dielectric near fields.

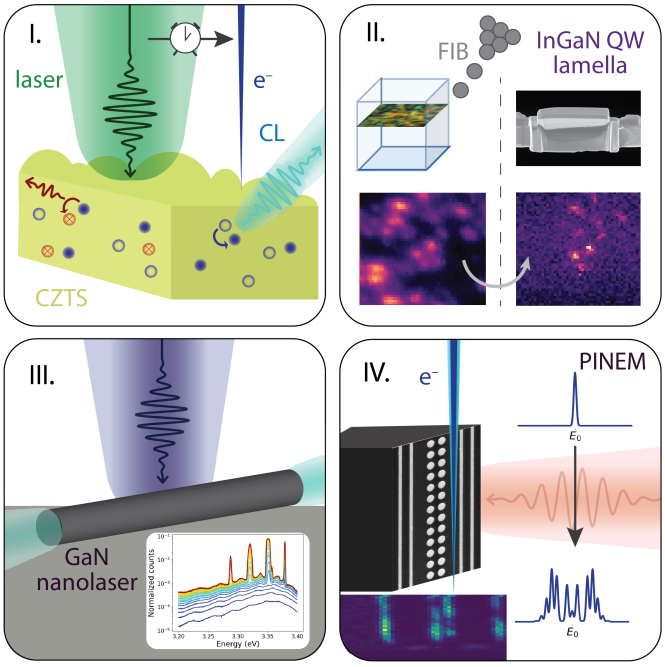

In **Chapter 2**, we introduce our USEM instrument, and utilize PP-CL with the electron beam as a probe to study carrier recombination dynamics in Cu_2ZnSnS_4, a semiconductor of interest for thin film photovoltaics using earth-abundant materials. We develop an analytical model describing the material response and extract the recombination rates of both radiative and non-radiative defects in the material.

In **Chapter 3**, we combine correlative CL spectroscopy and TR-CL using pulsed electron beams generated via electrostatic beam blanking, to investigate an InGaN/GaN quantum well (QW) structure before and after lamella preparation using focused ion beam (FIB) milling. While FIB is a popular method of sample thinning for TEM studies, we demonstrate how the optical properties of InGaN/GaN are significantly impacted. We find that despite measures taken to circumvent ion-

induced damage, QW luminescence is quenched and its emission lifetime reduced.

In **Chapter 4**, we use the light-incoupling capabilities of the PP-CL instrument to investigate the lasing properties of individual GaN nanowires (NWs). We study the lasing dependence on the single nanowire morphology, accessed using SE imaging, and intrinsic material properties, accessed with CL spectroscopy and TR-CL over a range of temperatures. We find that the lasing threshold is strongly dependent on the substrate and aspect ratio, and that recombination is limited by surface defects.

Finally, in **Chapter 5**, we reconfigure the pump-probe microscope to incorporate a home-built electron energy spectrometer based on a retarding field analyzer (RFA), enabling PINEM and EELS measurements in the USEM in the strong coupling regime. We describe the technical implementation of the set-up and alignment procedures, and demonstrate near-field mapping of a dielectric metasurface. We then use PINEM cross-correlation measurements and energy filtering with the RFA to measure the electron pulse lengths and energy spread as a function of different gun parameters. We find a lower limit of the electron energy spread of 0.3 ± 0.03 eV, and a lower limit of the pulse length of 0.5 ps.

In summary, this thesis demonstrates how our USEM based PP-CL instrument can probe the dynamics of a variety of semiconductor and dielectric geometries at the nanoscale, enabling direct exploration of their LDOS and carrier recombination pathways. We expand the capabilities of the instrument by incorporating electron energy spectroscopy, and demonstrating PINEM in the SEM. This new geometry constitutes a powerful method of near-field microscopy in which single-electron counting provides a direct measure of the optical near-field at a resolution set by the electron beam. Together, these advances enable a new range of studies of fundamental electron-light-matter interactions.

2

PUMP-PROBE CL ON Cu_2ZnSnS_4

Our group has developed a novel pump-probe cathodoluminescence (PP-CL) microscopy instrument, enabling the study of nanoscale material dynamics and electron-light interactions. The set-up utilizes synchronized femtosecond light pulses and focused picosecond electron pulses with energies between 2 to 30 keV that are generated through pulsed laser induced photoemission in an ultrafast scanning electron microscope. In this configuration, the spatial resolution of the electron beam can be combined with the versatility and temporal resolution of optical pump probe experiments. We demonstrate the suitability of this instrument to study the carrier recombination dynamics in Cu_2ZnSnS_4 (CZTS), a promising semiconductor for photovoltaic applications. We observe that the excitation of CZTS with increasingly higher laser powers leads to a blue-shift as well as a saturation in the peak energy of the photoluminescence spectrum, which we ascribe to the filling of shallow defect states near the valence band. Using PP-CL, we measure and extract the nanosecond lifetimes of these shallow radiative defects, as well as non-radiative defects in the material, and present an analytical model describing the system. We conclude with a discussion on the limitations of the technique and suggestions for the design of future PP-CL experiments.

2.1. INTRODUCTION

In this work, we use our novel pump-probe cathodoluminescence (PP-CL) instrument to study the carrier recombination dynamics of Cu_2ZnSnS_4 (CZTS), a promising semiconductor material for photovoltaic (PV) applications. With a direct bandgap of ~ 1.5 eV, which is furthermore tuneable through alloying, it is a favourable material for standalone, thin film, and multi-junction tandem solar cells[94]. Unlike most perovskites, which are currently the forerunner in PV research, CZTS is non-toxic, and compared to its direct competitor $CuIn_xGa_{1-x}Se_2$ (CIGS), it is entirely composed of earth-abundant materials. Despite these advantages, state-of-the-art CZTS solar cells perform relatively poorly in efficiency, well below the 32.1% of the detailed balance limit[95]. This performance gap comes as a result of the material's complex atomic structure and narrow thermodynamic stability window[96], making high-quality single-phase CZTS challenging to grow and prone to high defect densities. The most common defect has been identified as Zn on Cu anti-site defects, that have been shown in literature to form shallow trap states and intrinsic p-doping [97]. Nonetheless, after a long period without major developments, a new record efficiency of 13.2%[98] was recently achieved. Advancing further requires the careful study of the defects in the material, highlighting the importance of understanding defect mechanisms and recombination dynamics further.

Pump-probe techniques offer a powerful way to access such dynamic information by exciting a material with a initial excitation pulse (the pump) and probing the dynamics of the excited state with a time delayed second pulse (the probe). While most pump-probe studies rely on two laser pulses, our PP-CL instrument uses synchronized electron and laser pulses. This approach combines the temporal resolution of the technique with the spatial resolution of the electron beam. In this chapter, we investigate the configuration where the laser serves as the pump and the electron beam as the probe, allowing us to measure the de-trapping dynamics of defects in CZTS, with CL as the signature.

2.2. EXPERIMENTAL SET-UP

Our experimental set-up, including detailed characterization and alignment procedures, is described in [99], and a schematic of the geometry is shown in Figure 2.1. In brief, the set-up is based on a modified SEM (Thermo Fisher Quanta 250), integrated with a Yb-doped fiber oscillator/amplifier laser (Clark MXR Impulse). The laser delivers 250 fs pulses with a tunable repetition rate between 200 kHz - 25.19 MHz. Its fundamental output at λ = 1034 nm is up-converted using a harmonic generator consisting of a series of beta barium borate crystals to generate the 2^{nd}, 3^{rd}, and 4^{th} harmonics, corresponding to λ = 517, 345, and 257 nm respectively. The 3^{rd} and 4^{th} harmonics can be focused onto the electron cathode of the SEM to directly generate electrons by photoemission, although the 2^{nd} harmonic can also be used to generate photoelectrons through two-photon absorption. In parallel, the fundamental or any of the harmonics can be routed through a delay stage (Newport M-IMS600PP), coupled into the SEM chamber via a vacuum win-

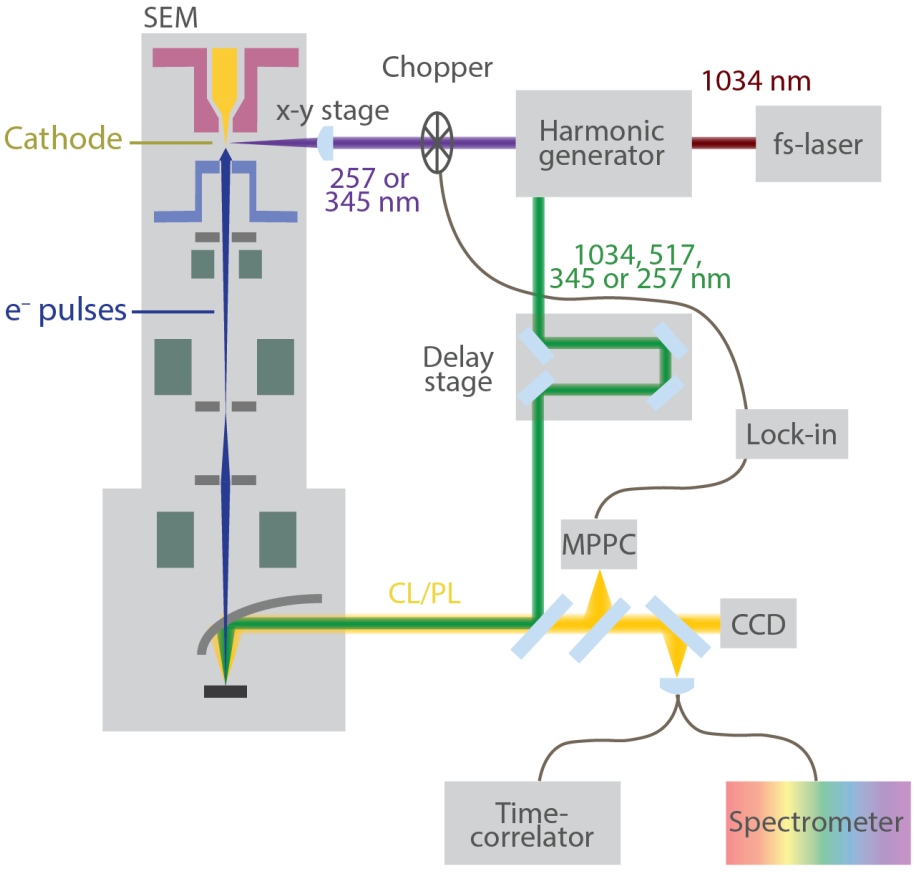

Figure 2.1: Schematic of the pump-probe CL setup. The 3rd, or 4th harmonics (λ = 345, 258 nm) of a 250 fs laser are modulated using an optical chopper and focused onto the electron cathode of an SEM to photo-induce picosecond electron pulses that are focused onto the sample. A parallel laser path, of the fundamental output or any up-converted harmonic, is coupled into the SEM chamber via a parabolic mirror to synchronously photo-excite the sample. The arrival time of the laser pulse with respect to the electron pulse is controlled via a delay stage. The emitted CL and PL is collected and directed to an optical set-up.

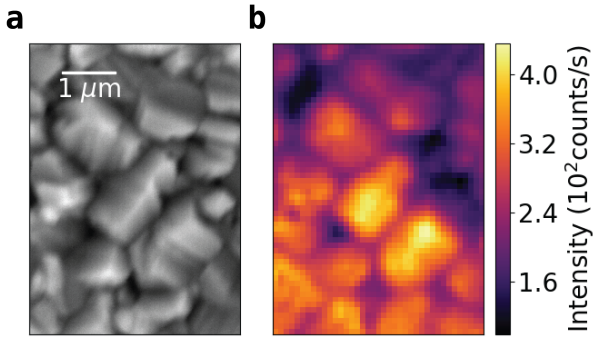

Figure 2.2: (a) Secondary electron image of the CZTS sample, with (b) the corresponding CL intensity map integrated over $\lambda_c = 920 \pm 25$ nm.

dow, and focused onto the sample for photo-excitation by a parabolic aluminium mirror (acceptance angle 1.46π sr, focal distance 0.5 mm). This mirror also collects the emitted luminescence, either CL or photoluminescence (PL), from the sample and redirects the collimated beam out of the SEM to an optical detection set-up. The available detection schemes include a CCD camera for mirror imaging and sample alignment, and other photodetectors such as a multi-pixel photon counter (MPPC, Hamamatsu C14455-3050GA), fibre-coupled spectrometer (Princeton Instruments Spec10), and a time-correlated single photon counting module (Picoquant PicoHarp 300). The stability of the laser paths are maintained using an active beam stabilizer system (TEM Messtechnik Aligna), ensuring reproducibility of the alignment while scanning over the delay stage.

2.3. PL AND CL CHARACTERIZATION

The CZTS sample investigated in this study was fabricated in the group of Prof. Xiaojing Hao at the University of New South Wales, Australia, using a method similar to that described by Yan et al. in [100]. In brief, sample precursors were deposited via sputter coating onto a Mo/glass substrate, followed by rapid annealing in vacuum. This process yielded a CZTS layer of approximately 800 nm thickness, which was further passivated with a roughly 3 nm thick layer of Al_2O_3. A secondary electron image of the sample is shown in Figure 2.2a, with a concurrent CL map integrated between 895 and 945 nm shown in Figure 2.2b. The CL map was acquired under excitation with a 10 keV continuous electron beam. These figures reveal that the sample consists of grains on the order of microns in size, and that there is a notable decrease in CL intensity at the grain boundaries. Such reduction in intensities are commonly attributed to non-radiative recombination caused by concentrated defect states localized at the grain boundaries[101], however, recent work has shown that reduced out-coupling efficiency associated with the morphology of the grain can play a significant role as well[102].

To investigate the effect of excitation density on radiative recombination, the

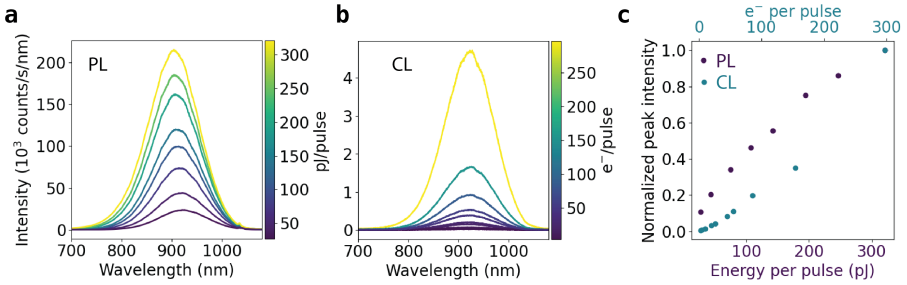

Figure 2.3: (a) PL spectra obtained by exciting a bulk CZTS sample with a λ = 517 nm pulsed laser beam of increasing pulse energy (28 pJ to 323 pJ per pulse). (b) CL spectra obtained via excitation with a 10 keV pulsed electron beam with increasing number of electrons per pulse (3 to 299 electrons per pulse). (c) Normalized peak intensities of the PL (purple) and CL (blue) spectra as a function of increasing excitation densities.

CL spectrum from the sample was measured under pulsed electron-beam excitation as a function of the number of electrons per pulse, as shown in Figure 2.3b. The electron current was controlled by varying the power of the 4$^{\text{th}}$ harmonic laser (λ = 257 nm, repetition rate = 25.19 MHz) used to drive the electron cathode, with an open aperture and low extractor voltage (V_{ext} = 650 V). For comparison, the PL spectra were measured as a function of excitation pulse energies using the 2$^{\text{nd}}$ harmonic laser beam (λ = 517 nm, repetition rate = 25.19 MHz), as shown in Figure 2.3a. Although a long pass 532 nm filter was used to block scattered laser light from reaching the spectrometer, a small peak at 1034 nm is observed in the spectra as a result of second-order diffraction from the spectrometer grating. The penetration depth of the laser light within the sample can be estimated using the Beer-Lambert law. CZTS is a strong absorber with an absorption coefficient >10^4 cm^{-1} through the visible, and $\alpha \sim 7.1 \times 10^4 \text{cm}^{-1}$ at λ = 517 nm[100], corresponding to a $1/e$ penetration depth of the laser of 141 nm, as plotted in Figure 2.4b. To maintain a similar excitation volume within the sample during electron excitation, CASINO Monte Carlo[103] simulations of the electron beam were performed, as plotted in Figure 2.4a, which showed that 10 keV electrons provide a comparable penetration depth.

At low excitation densities, both the CL and PL spectra are centered at around 920 nm, consistent with radiative recombination from shallow tail states near the valence band[67, 104]. Upon increasing excitation pulse energies, around 30 to 300 pJ per pulse, the PL spectra exhibit a blue-shift with an apparent saturation of the emission intensity. This behaviour is consistent with the Moss-Burnstein effect, that is commonly observed in intrinsically doped semiconductors with a high density of shallow trap states, and has been reported previously in literature on CZTS[67, 104]. In the weak excitation regime, monomolecular radiative recombination from these trap or tail states has a linear dependence on excitation density. As the tail states are progressively filled, this recombination channel saturates[105]. At high carrier densities, recombination shifts to bimolecular band-to-band recombination, which scales quadratically with carrier density, and results in the observed

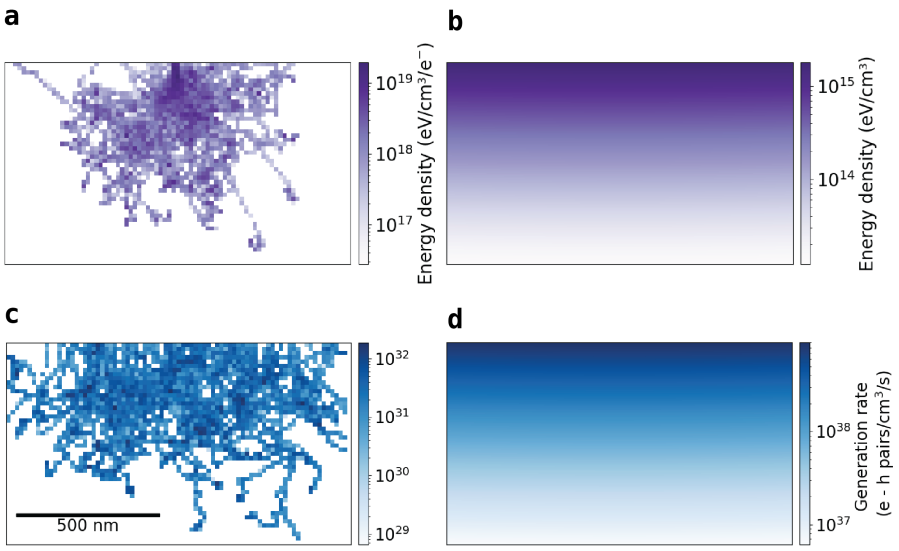

Figure 2.4: Electron- and laser- deposited energy densities (top row) and carrier generation rate in CZTS under pulsed excitation (bottom row). (a) CASINO Monte Carlo simulations of 10 keV electrons with a beam diameter of 5 nm, planarly incident on CZTS (density = 4.33 g/cm^3). The simulation volume was divided into cubic bins of 10 nm side length, to calculate the deposited energy density per electron. (b) Calculated deposited energy density by incident laser beam with λ = 517 nm and a beam of 10 μm diameter incident on CZTS (absorption coefficient $\alpha = 7.1 \times 10^4 \text{cm}^{-1}$ [100]) using the Beer-Lambert law. The laser power was scaled such that a total of 10 keV energy was deposited into the sample. (c) Calculated carrier generation rate by a 5 ps electron pulse containing 300 electrons and focused to a 900 nm diameter (d) Calculated generation rate by a 300 μJ laser pulse of 250 fs duration.

blue-shift. The reduced relative efficiency of bimolecular recombination compared to monomolecular leads to the intensity saturation.

In contrast, the CL spectra do not show any blue-shift or intensity saturation as the excitation density is increased from ~3 to 300 electrons per pulse. While the CASINO Monte Carlo simulations in Figure 2.4 demonstrate that the electron beam deposits a much higher peak energy density than the laser (on the order of 10^{19} eV/cm^3 per electron compared to 10^{15} eV/cm^3 for laser excitation with the same total energy), it should be noted that the deposited energy does not translate into carrier generation rate in the same way for electron and laser pulses. Moreover, for electron beams in the regime of hundreds of electrons per pulse, the focal spot degrades from the simulated 5 nm beam diameter to around 900 nm under experimental conditions[53], as a result of Coulomb repulsion[106]. Under electron-beam excitation, carriers are excited indirectly. The electron beam interacts with the sample through multiple inelastic collisions. The deposited energy results in the generation of bulk plasmons (estimated as 16 eV for CZTS using the Drude plasma frequency relation) that subsequently decay into several electron-hole pairs[31, 33]. In contrast, each absorbed photon with an energy above the band gap in a direct band gap semiconductor excites an electron-hole pair. Therefore, the carrier excitation efficiency per deposited energy density is greater for the laser beam than for the electron beam. Additionally, high current electron pulses have durations on the order of picoseconds, rather than the hundreds of femtoseconds for the laser, which reduces the instantaneous generation rate even further. The instantaneous carrier generation rates for an electron pulse of 300 electrons and laser pulse of 300 μJ are plotted in Figure 2.4 c & d respectively, with the calculation procedure described in Supplementary 2.6.1. From these calculations, we find generation rates on the order of 10^{31} cm^{-3}s^{-1} for the electron beam, and 10^{38} cm^{-3}s^{-1} for the laser. These results explain why, even at the highest electron-beam currents used, CL doesn't reach carrier densities sufficient to saturate tail states or induce a Moss-Burnstein shift, highlighting the electron beam's suitability as a stable probe in PP-CL.

2.4. PP-CL CHARACTERIZATION

In a pump-probe configuration, both PL and CL signals are detected simultaneously. As the PL signal intensity was so much stronger than the CL, phase sensitive lock-in detection was necessary to isolate the weaker CL signal above the PL background. Lock-in detection also serves to suppress noise arising from fluctuations in the laser intensity. For this purpose, the laser beam exciting the electron cathode was chopped at a frequency of 287 Hz, leading to a modulation of the electron pulses and the resulting CL emission at the same frequency. This frequency was chosen to avoid interference from the 50 MHz mains current and its harmonics. The chopper was used as a reference signal for the lock-in amplifier (Stanford Research Systems RS830 DSP), while the CL and PL signals were collected, filtered with a long pass 532 nm filter, and redirected towards the multi-pixel photon counter (MPPC, Hamamatsu C14455-3050G). The luminescence signals were additionally filtered

using neutral density filters to keep to MPPC output voltage < 550 mV and avoid the repetition-rate dependent saturation levels of the MPPC[99]. Despite the use of lock-in detection to improve sensitivity, the CL intensity still needed to be sufficiently strong, requiring operation at high laser repetition rates, and high currents of ~ 320 electrons per pulse.

We performed PP-CL measurements as a function of the relative delay between electron and laser pulses, Δt. For each delay point, two signals were recorded: (i) the PP intensity, the CL intensity with both the electron and laser beams exciting the sample, and (ii) a reference CL intensity, with only electron beam excitation. The results of our PP-CL measurements are plotted in Figure 2.5. On the y-axis, we report the relative change (as a percentage) of the CL intensity as a result of laser excitation, compared to the reference CL signal without laser excitation. This metric is defined as,

$$\Delta\text{CL} = \frac{\text{PP} - \text{CL}}{\text{CL}} \times 100, \tag{2.1}$$

where PP is the MPPC output voltage with both the electron and laser beams exciting the sample, and CL is the output voltage with only electron beam excitation. A positive ΔCL corresponds to CL enhancement, while a negative value indicates CL suppression as a result of laser excitation. A negative delay, $\Delta t < 0$, corresponds to the electron pulse arriving at the sample before the laser pulse, a positive delay, $\Delta t > 0$, corresponds to the electron arriving after the laser pulse, and at $\Delta t = 0$ the two pulses are coincident. To avoid artifacts as a result of sample damage, the delay positions are randomized during the scan. Owing to the stroboscopic nature of the measurements, each data point corresponds to the average of $\sim 7.5 \times 10^8$ pump-probe cycles (25.19 MHz repetition, 30 seconds integration time). Each data point is furthermore measured 4 times, with the standard deviation between measurements represented by the error bars. The reproducible observation of a delay-dependent PP-CL signal demonstrates that no progressive beam damage under these conditions, otherwise the signal contrast would be lost in averaging. Because the electron cathode is kept cold during the measurement to generate photoemission pulses, the zirconium oxide coating that enhances electron emission gradually depletes within less that an hour, leading to a reduced beam current. To maintain a stable emission current over long acquisitions, each delay scan is divided into two halves with an intermediate flashing of the tip to restore the coating.

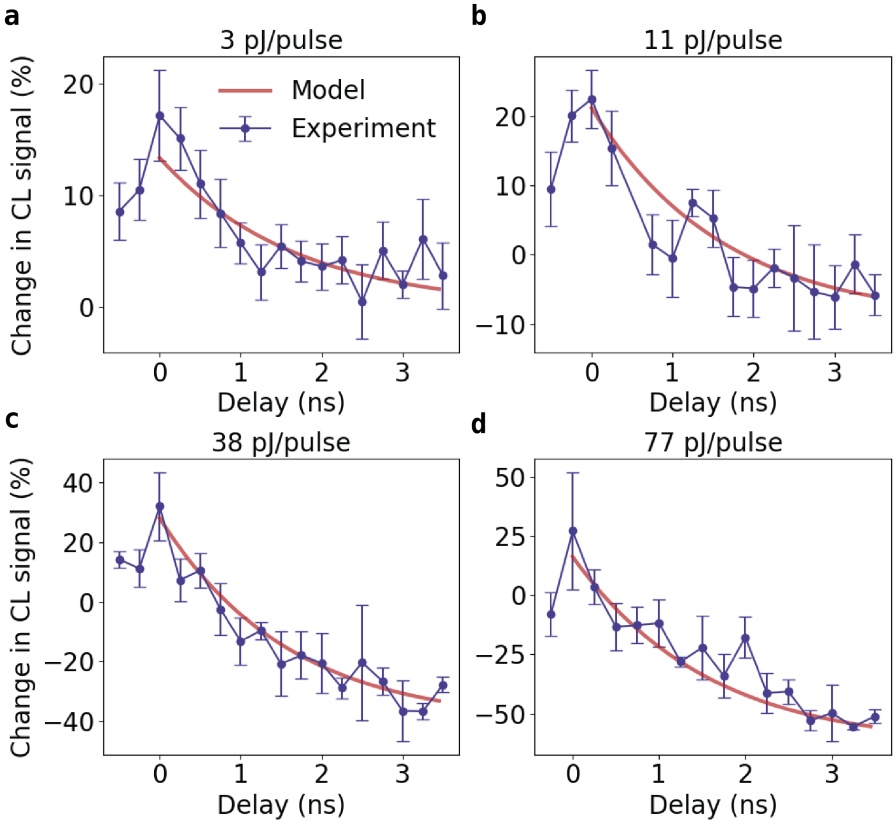

Figure 2.5: Relative change in CL signal with respect to the reference CL signal as a result of laser beam excitation as a function of delay between the laser and electron pulses, measured for different laser energies in the range of 3 - 77 pJ/pulse. A negative delay corresponds to the electron pulse arriving before the laser pulse.

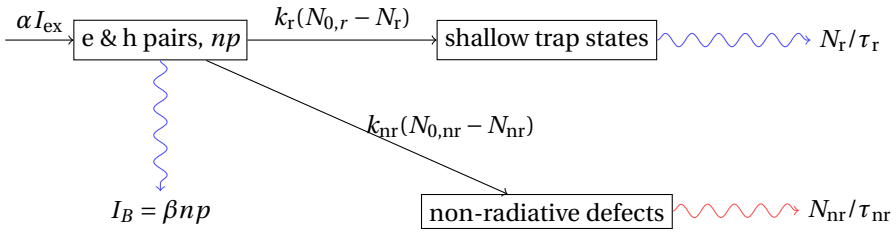

Figure 2.6: Visualization of the rate equation model describing the carrier dynamics probed with PP-CL. Each laser pulse generates free electrons and holes with carrier concentrations n and p, which can (i) undergo bimolecular radiative recombination, (ii) trapping at shallow trap states that recombine radiatively, or (iii) trapping at non-radiative defects.

At low laser pulse energies, shown in Figure 2.5 (a), we observe that the CL signal is enhanced by up to ~17% when the laser and electron beams are both coincident temporally on the sample, at $\Delta t = 0$. This enhancement decays rapidly and the CL signal reverts back to its reference intensity at later delays. With increasing laser pulse energy, as plotted in Figure 2.5 (b), the CL enhancement at zero delay increases to ~ 22% at zero delay, however, as the delay increases the signal no longer relaxes fully to it's reference intensity but exhibits a small suppression of around −10%. Finally, at higher excitations, Figure 2.5 (c-d), the maximum enhancement reaches up to~30%, and the, CL suppression becomes even stronger, reaching below ~50% at later delays.

These dynamics are well described by a standard rate equation model, similar to that in ref. [105], which is summarized schematically with a rate equation diagram in Figure 2.6. In the model, each laser pulse excites free electron-hole pairs in the material, with concentrations n and p respectively. These charge carriers can subsequently recombine through three competing pathways. Firstly, they can undergo direct bimolecular recombination, producing luminescence with intensity $I_B = \beta np$, where β is the bimolecular decay coefficient. Secondly, the charge carriers can be trapped in shallow trap states located near the band edge. We assume that these are the same states to those observed in the PL vs. excitation density measurements in Figure 2.3 (a), where the progressive filling of the traps leads to a blue-shift of the emission peak. The capture rate is proportional to the carrier density and the density of trap states in the ground state, $k_r n(N_{0,r} - N_r)$, where k_r is the capture coefficient, N_0 the nominal trap density, and N_r the density of filled trap states. Once trapped, the carriers radiatively recombine at a rate N_r/τ_r. Thirdly, the charge carriers can be trapped within non-radiative defects that exist within the sample, with a capture rate $k_{nr} n(N_{0,nr} - N_{nr})$, where $N_{0,nr}$ is the nominal density of non-radiative defects, N_{nr} is the density of filled non-radiative defects, and k_{nr} is the capture coefficient, after which they recombine at a rate N_{nr}/τ_{nr}.

The PP measurements could be understood in terms of how the laser pulse modifies the availability of non-radiative and radiative defect channels for the electron - induced carriers. When the carriers excited by the laser beam populate the non-radiative defects in the material, their capture probability is reduced, prevent-

ing carriers injected by the electron beam from capture. As a result, a greater fraction of the carriers recombine radiatively and the CL intensity is enhanced relative to the reference intensity. At the same time, the laser also fills the shallow radiative trap states. Because these monomolecular radiative traps normally provide a fast radiative recombination pathway, their progressive saturation at higher pulse energies forces electron-excited carriers into slower bimolecular recombination. As a result, the CL intensity becomes suppressed relative to the reference intensity. This also indicates that non-radiative recombination is one of the dominant channels in the materials, as even when the shallow radiative traps are simultaneously saturated, the CL intensity is still enhanced. The measurements effectively probe the de-trapping kinetics of both the non-radiative and radiative defects. Accordingly, the experimental data at positive delays could be fitted using the equation,

$$\Delta\mathrm{CL}(t) = N_{\mathrm{nr}}(0)e^{-t/\tau_{\mathrm{nr}}} - N_{\mathrm{r}}(0)e^{-t/\tau_{\mathrm{r}}} \tag{2.2}$$

A global least-squares fitting of equation 2.2 was performed on the four data sets in Figure 2.5, resulting in a non-radiative defect recombination rate with an associated lifetime of $\tau_{\mathrm{nr}} = 1.68 \pm 0.78$ ns. Due to the limited experimental delay window and slow recombination rate of the shallow traps, τ_{r}, a precise fit could not be reliably extracted. To estimate a lower bound on τ_{r}, we scanned the fitting over fixed values of τ_{r} and examined the resulting χ^2, which plateaued beyond approximately 43 ns, indicating that the data is no longer sensitive to increases in τ_{r}. Therefore, we report a lower bound of $\tau_{\mathrm{r}} \geq 43$ ns and note that the actual decay time may be longer. Important to note is that this lower bound exceeds the time between laser/electron pulses (39.7 ns at repetition rate of 25.19 MHz), suggesting that these long-lived defect states do not completely relax back to their ground state between pulses which leads to some degree of cumulative offset of the CL over many pump-probe cycles. However, τ_{r} cannot be arbitrarily long, as otherwise its contribution would appear as a flat background offset, inconsistent with the observed dynamics. To confirm this model, it would be desirable to perform spectrally resolved PP-CL measurements, however, filtering the already weak CL signal led to too strong a reduction of signal-to-noise.

2.5. CONCLUSIONS

We demonstrated PP-CL on CZTS and highlight how the technique can be used to probe recombination pathways and their dynamics. Due to the low carrier injection, the electron beam is a suitable probe that can distinguish between non-radiative and radiative recombination dynamics which are not directly accessible with TR-CL and hyperspectral measurements. However, several limitations of the PP-CL techniques appear. Under the high current conditions required for PP-CL, the spatial resolution of the electron beam degrades to hundreds of nanometers[53]. This compromises one of the advantages of using electrons in a pump-probe experiments compared to standard laser-laser based methods. Although a high spatial resolution can in principle be recovered in the limit of <1 electron per pulse, in this

regime the CL signal would not be recoverable above the PL background. Consequently, it was unfeasible in the present experiment to map the PP-CL signal across grains to investigate spatially varying decay dynamics.

Nonetheless, this provides useful insights for important design considerations of future PP-CL experiments. Since the biggest challenge of the technique is isolating the weak CL signal over the stronger PL background, future implementations of spatially-resolved PP-CL should avoid a spectral overlap between the CL and PL signals. This would enable the use of low electron currents and maintain a high spatial resolution of the electron beam. An approach to achieve this would be to design an experiment where it is possible to engineer a spectral separation between the PL and CL, for example, by studying resonant nanostructures and tuning the CL-excited (Mie) resonances away from the PL band. Another approach is by employing laser excitation wavelengths that do not excite PL at all, but instead pump the sample into a different state, for instance, via heating the sample which would enable studies of phase-transformations at high spatial resolution. Finally, PP-CL sensitivity may also be improved by reducing the effective laser-excited lateral area such that the total PL background intensity is reduced while the CL intensity is maintained. This can be achieved by studying patterned or nanostructured semiconductors as opposed to bulk semiconductor materials. However, it is important to keep in mind that the measurement procedure is time-intensive and a single delay scan can require more than one hour of measurement time. This should be considered when planning high spatial resolution PP-CL mapping requiring pixel by pixel measurements.

2.6. SUPPLEMENTARY

2.6.1. CARRIER GENERATION RATE CALCULATION

To calculate the carrier generation rate under electron excitation, the bulk plasmon energy of CZTS was first estimated using,

$$\omega_p = \sqrt{\frac{Ne^2}{\epsilon_0 m_e}} \tag{2.3}$$

where N is the valence electron density, e is the elementary charge, m_e is the electron mass, and ϵ_0 is the vacuum permittivity[30]. For CZTS, we obtain a plasmon energy of approximately 16 eV. The deposited energy density per electron was calculated using CASINO Monte Carlo simulations of a 10 keV electron beam focused to a diameter of 900 nm. Dividing the deposited energy density by the plasmon energy gives the corresponding plasmon density. The number of excited carriers per plasmon was then estimated using the pair-creation energy for compound semiconductors, ϵ given by,

$$\epsilon = 2.73E_g + 0.55\text{eV} \tag{2.4}$$

where E_g is the bandgap of CZTS[33]. Thus the number of electron-hole pairs generated per plasmon is given by $\hbar\omega_p/\epsilon$. Finally, scaling this value by the number of electrons per pulse and dividing by the electron pulse duration (estimated as 2.5 ps, see Chapter 5) yields the instantaneous carrier generation rate in units of $\text{cm}^{-3}s^{-1}$.

For laser excitation, the carrier generation was calculated using the Beer-Lambert law. The fluence assuming a Gaussian beam distribution was calculated using,

$$F(x) = \frac{2E_{pulse}}{\pi w_0^2} \exp\left(-\frac{2x^2}{w_0^2}\right) \tag{2.5}$$

where E_{pulse} is the pulse energy, and w_0 is the beam waist. The absorbed energy density as a function of depth was then calculated using the Beer-Lambert law,

$$E(x,z) = \alpha F(x) e^{-\alpha z} \tag{2.6}$$

where α is the absorption coefficient of CZTS. The carrier density was then calculated by dividing the absorbed energy by E_g, assuming unity efficiency of the photon to carrier conversion, and further divided by the laser pulse duration (250 fs) to obtain the carrier generation rate in $\text{cm}^{-3}s^{-1}$.

3

EFFECTS OF LAMELLA PREPARATION ON INGAN QW LUMINESCENCE

Despite it being a popular sample preparation technique, the optoelectronic effects of thinning bulk samples into lamella using a Ga-based focused ion beam (FIB), as is commonly performed for studies in a transmission electron microscope, have been seldom studied systematically. In this work, we confront this using correlative cathodoluminescence (CL) spectroscopy, to investigate the optical properties of high In content c-plane InGaN/GaN quantum wells, fabricated including a growth interrupting step that forms regions of quantum disc InGaN islands that behave as localized emitters and furthermore reduce the strain-induced quantum Stark effect present in majority of such heterostructures. Using picosecond electrostatically beam blanked electron pulses, we measured the decay transients as a function of position and wavelength. The sample was studied before and after undergoing preparation as lamella, demonstrating that FIB preparation affects both the spectral and temporal luminescence properties despite measures undertaken to protect the sample during fabrication. Non-radiative defects introduced by the ion beam quenched the luminescence as well as reduced the lifetime of emission, with the quantum well luminescence component particularly affected, due to the emission being weakly localized and hence allowing carriers to migrate to defect areas. These findings underscore the importance of correlating bulk and lamella properties to accurately interpret optical measurements.

3.1. INTRODUCTION

Lamella preparation using focused ion beam (FIB) milling is a powerful technique in material science, enabling the fabrication of electron-transparent and site-specific samples for atomic-scale analysis within a transmission electron microscope (TEM). This method has been applied to understand the structural and chemical features of a variety of material systems, including group III/V semiconductors. Due to its nanoscale spatial resolution and keV energy regime, cathodoluminescence (CL) has emerged as an ideal tool for optical characterization of high-energy bandgap materials, such as GaN, far beyond the optical diffraction limit [107–109]. Such measurements are routinely performed in TEMs on GaN devices [110–114], as well as other materials [115, 116]. These CL-TEM studies enable the correlation of radiative properties and defect-related emission with the structure of the material at the nanoscale. However, it is well-known that FIB lamella preparation can also introduce artefacts. The ion beam has been shown to cause localized damage such as ion implantation, sputtering, amorphization and point defect creation, including vacancies, and damage from thermal effects. As these artefacts are linked to the interaction volume of the ion beam within the material, the FIB leaves a damaged layer of several tens of nm thick[117], depending on the energy of the ion beam [118]. Hence, a large body of work has been performed to mitigate these issues and optimize the FIB parameter space[119]. This includes reduction of ion beam energy[120], thereby reducing the collision cascade, the deposition of platinum or tungsten protective layers, utilization of chemically inert plasma beams such as Xe[121], post-thinning annealing to restore the crystal structure[122], and research is ongoing. Nonetheless, some studies are emerging indicating that despite the measures undertaken to mitigate ion-induced damage, FIB lamella often do not replicate the radiative emission characteristics of their bulk counterparts[123, 124]. These differences cannot be attributed solely to the reduction of the material dimensions via thinning, that can possibly modify strain. While the implications of this research are crucial for TEM-based CL studies, where conclusions about the bulk material may be deduced from optical measurements on lamella, to the best of the authors knowledge, correlative measurements on the same material in both configurations are yet to be demonstrated. In this work, we use scanning electron microscope (SEM)-CL, to investigate the optical properties of the same region of an InGaN/GaN quantum well heterostructure in both its bulk form and as a FIB-prepared lamella. The heterostructure in our case study is composed of single quantum well (QW) and quantum disc (QD) active regions, resulting in a significant spectral variation of the CL signal with position across the sample and enabling the identification of the same region at the nanoscale before and after lamella preparation. By employing hyperspectral CL, we capture the spatially resolved emission spectra to evaluate changes in radiative spectral properties, while time-resolved CL (TR-CL) provides insight into recombination dynamics. We find that FIB preparation affects both these properties, emphasizing the need to clearly understand its impact to be able to retrieve the bulk properties from TEM-CL study.

3.2. SAMPLE PREPARATION

The sample was grown, as demonstrated graphically in Figure 3.1a, by metalorganic vapor phase epitaxy (MOVPE) on a (001) sapphire substrate using a custom Dragon family horizontal-flow episystem with an inductively heated susceptor and standard precursors[125]. Growth started from a low-temperature GaN nucleation layer followed by thick high-temperature GaN growth to reduce dislocation density. Subsequently, the temperature was lowered and a 4 nm layer of $In_xGa_{1-x}N$, where x = 25 – 30%, was deposited in hydrogen-free ambient. Prior to overgrowth with GaN, the InGaN was subjected to a growth-interruption (GI) step using exposure to a hydrogen-containing atmosphere. The details of the procedure on a similar growth and the resulting impact expected on the external quantum efficiencies (EQEs) have been described by Tsatsulnikov et al.[125]. The stoichiometry of the sample was calculated using strain-state analysis (Supplementary Figure 3.1) of $(1\bar{1}00)$ cross-sectional high-angle annular dark-field scanning transmission electron microscopy (HAADF-STEM) images which were corrected for distortion and calibration errors by applying AbStrain procedure[126–128]. As a result of the GI step, the InGaN layer is etched, transforming the homogenous layer into areas of 2D InGaN QWs, as shown in the HAADF-STEM image in Figure 3.1bi, and 3D InGaN QDs with a lateral confinement on the order of tens of nm, Figure 3.1bii. Although this is larger than the Bohr radius of excitons in InGaN (which, depending on the stoichiometry, is between the approximately 3 nm for GaN[129] and 8 nm for InN[130]), InGaN QDs of similar length scales have demonstrated blue shifting due to lateral confinement[131, 132]. This fabrication approach was originally developed to promote confinement of carriers within QD regions of the sample, mitigating carriers from migrating in the QW plane to defects and dislocations[133], and ensuring a higher EQE of resulting devices. However, it additionally prevents indium phase segregation[134], and reduces the strain-induced quantum confined stark effect (QCSE) present in majority of such structures (as will be evidenced in data shown later in the manuscript).

After full optical characterisation of two identified areas on the bulk sample, we extracted two lamellae from these areas: one in cross-section and another in plan-view. These preparations were carried out using a gallium ion source on a ThermoFisher Helios Nanolab 600i dualbeam FIB/SEM microscope at 2×10^{-6} mbar. To protect the surface of the samples, two layers of carbon and platinum (a few hundred nanometres thick) were deposited by focused electron beam induced deposition (FEBID). Then a thicker layer of about 1 μm of platinum was deposited by focused ion beam induced deposition (FIBID). The still thick lamellae were then cut and extracted using a microtip (Omniprobe 200 micromanipulator) and mounted on a TEM grid. Final thinning to a thickness of around 200 nm was performed using a graded voltage procedure, to reduce the damage caused by the FIB. The Ga beam acceleration was sequentially reduced: initially at 30 keV and 430 pA at a +1° angle, followed by 16 keV at 50 pA (+ 2°), 8 keV at 20 pA (+ 3°), 5 keV at 15 pA (+ 3°), and finally 2 keV at 20 pA (+ 4°). Each milling step was monitored live using SEM imaging and was stopped once the lamella reached desired thickness and several

tens of nm of material were removed. For the lamellae in plan-view, the protective layers previously deposited on the surface were milled using the FIB.

3.3. HYPERSPECTRAL CL MEASUREMENTS

A 2×2 μm^2 region of the bulk sample was characterized using cathodoluminescence experiments performed within a SEM equipped with a parabolic mirror for high-NA light collection and redirection to an optical spectrometer (see Supplementary Methods). The SEM was operated at 5 keV to minimize the penetration depth and the size of the electron cascade within the sample, thereby achieving a higher spatial resolution (see Supplementary Figure 3.2 for CASINO Monte-Carlo simulations[135]). The electron beam current was set to 10 pA to mitigate damage by the electron beam.

Figure 3.1c shows the measured CL map centered at $\lambda_c = 500 \pm 37.5$ nm, fitted to false-colour RGB values by splitting the wavelength range into three 25 nm channels. The spectra in Figure 3.1d corresponding to the highlighted pixels in the RGB map consistently form two discrete bands, resulting from quantum confinement effects in the inhomogeneous InGaN layer. For $\lambda_c < 500$ nm, we observe spatially localized emission visible by the blue region in Figure 1di that we associate with the QDs. Despite their physical size, the emission from the QDs is localized to emission spots of around hundred nanometres in diameter, limited by the size of the electron cascade and charge carrier diffusion (Supplementary Figure 3.2). For $\lambda_c > 500$ nm, the broader, less localized features shown in green and red colours in Figure 3.1dii and iii, are associated to the QW emission.

The strong localization of the $\lambda_c < 500$ nm band is more clearly observable in STEM-CL measurements on a cross-sectional lamella from the same sample growth, plotted in Figure 3.2. These measurements were performed in a dedicated STEM Nion at 60 keV and liquid nitrogen temperature, that achieve higher spatial resolution that SEM-CL. The position-dependent CL spectra in Figure 2a feature the same two bands observed in SEM-CL, and the CL maps filtered for $\lambda_c = 425 \pm 5$ nm and (d) $\lambda_c = 500 \pm 50$ nm in Figure 3.2c and 3.2d clearly show the spatial separation of the two bands. Furthermore,the lack of band-bending related red-shifting under electron beam excitation away from the QW[136], resulting in a lower exciation density, suggests that the QCSE are minimal, and, that any internal electric fields are largely unscreened and don't dominate the recombination dynamics. More hyperspectral measurements at room temperature and time-resolved measurements in the TEM for direct comparison to subsequent SEM-CL results are available in Supplementary Figure 3.3.

Next, we repeat the SEM-based hyperspectral CL experiments on the lamella sample; the SEM was now operated at 30 keV to achieve the highest spatial resolution, and a current of 10 pA was maintained. A representative false-colour RGB CL map is shown in Figure 3.3b with corresponding spectra in Figure 3.3c. These measurements show that the InGaN layer remains luminescent after lamella preparation, however, the integrated count rate has been significantly reduced. This is an

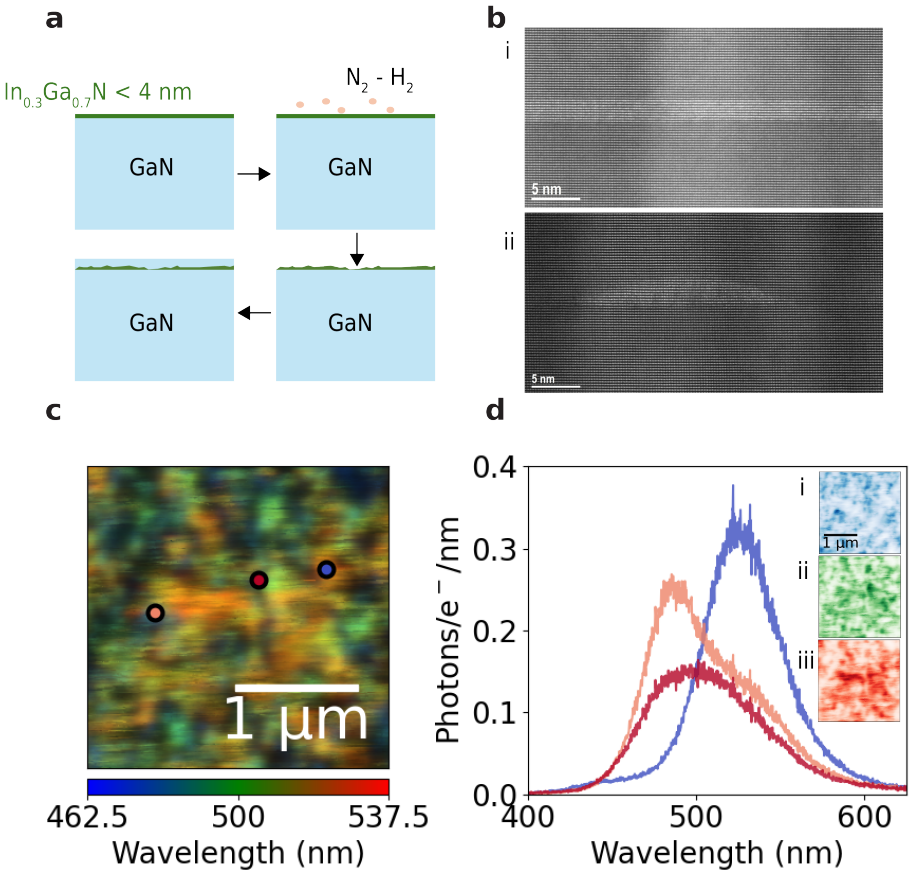

Figure 3.1: (a) Graphic demonstrating InGaN/GaN QW/QD fabrication. (b) High resolution 200 keV HAADF-STEM depicting QW (top) and QD (bottom) regions of the sample. (c) RGB SEM-CL map with pixel size 10 nm at $\lambda_c = 500 \pm 37.5$ nm of bulk sample. (d) CL spectra corresponding with measurement areas marked in (c). The insets show CL maps filtered for the three false color RGB bands, centered at λ_c = (i) 475 (ii) 500 and (iii) 525 nm, and bandwidth 25 nm.

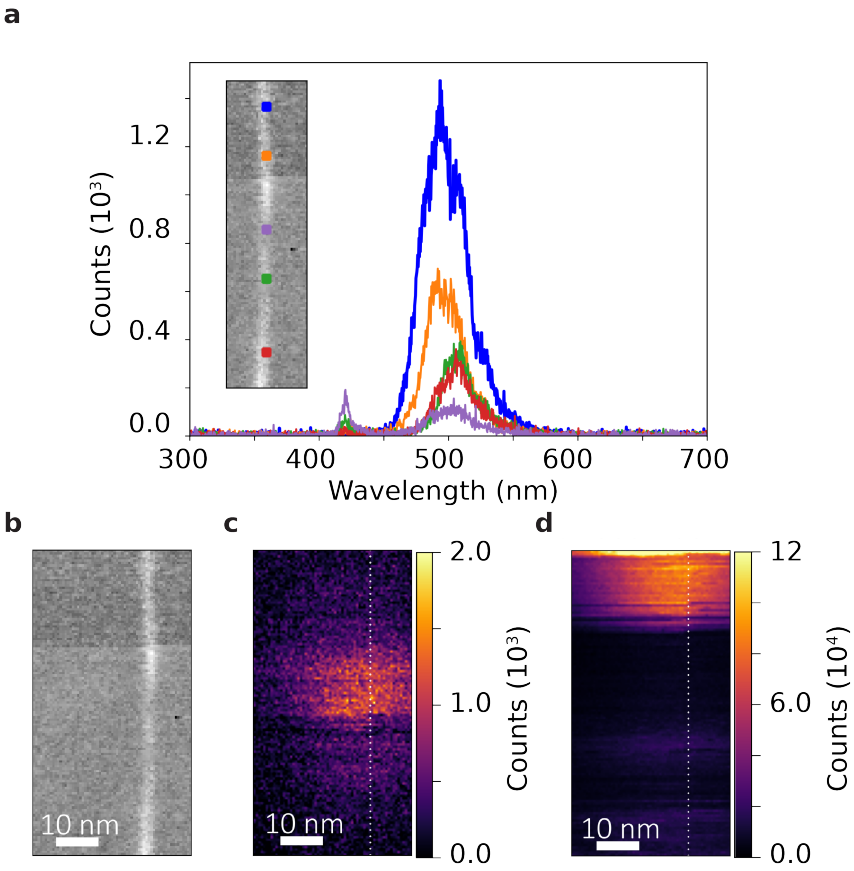

Figure 3.2: Hyperspectral TEM-CL measurements on cross-sectional lamella at 60 keV. (a) CL spectra from different positions along InGaN layer, as seen in dark field TEM image in (b), with CL measurement positions marked in the inset. (c) CL map with 0.6 nm pixel size at $\lambda_c = 425 \pm 5$ nm and (d) $\lambda_c = 500 \pm 50$ nm. The dotted lines indicate the position of the InGaN layer within the heterostructure.

anticipated feature considering that the energy deposited per electron changes by an order of magnitude as most electrons are being completely transmitted through the sample (3.2). However, the counts still drop by an additional five orders of magnitude, indicating that quenching due to defect creation has occurred. The spectra show that it is predominantly the QW emission component that has been affected and strongly optically quenched.

Due the the rich hyperspectral variation across the sample, the hyperspectral maps centered at $\lambda_c = 430 \pm 5$ nm in bulk and lamella, as seen in Figures 3.3d & 3.3e respectively, provided a unique spatially resolved signature that enables correlation before and after lamella preparation. The spectra from the same position in the two sample configurations are plotted in Figures 3.3f & 3.3g. This reveals the same trend that the QW emission is quenched and the QD emission is largely preserved. We also observe in the CL map of the lamella in Figure 3.3e, that some of the localized QDs over the scan area have dissapeared. This may be a result of the FIB milling away the platinum protective layer at an angle subsqeuntly leaving the sample partically covered with platinum, and partially milling into the InGaN layer.

3.4. TIME-RESOLVED CL MEASUREMENTS

The optical quenching observed, and thus the decrease of the quantum yield is intrinsically linked to the recombination rates of both radiative and non-radiative transitions in the material[105]. Moving from steady state to TR-CL experiments enables the study of excitation and recombination dynamics of carriers in a system[137, 138]. To measure TR-CL in our SEM, the electron beam was blanked using an electrostatic beam blanker resulting in pulses of about 30 ps (5 keV electron beam) and 100 ps (30 keV beam) widths[53]. The collected luminescence is directed towards a time-correlated single photon counting (TCSPC) module that builds an arrival time histogram.

The measurements on the bulk sample are shown in Figure 3.4a, where plots i and ii are the TR-CL maps filtered for QD and QW emission respectively. The pulsed measurements have a coarser spatial resolution, because of increased astigmatism from adjusting the gun column parameters to align the crossover position between the blanking plates[53]. However, the same trends we observed in Figure 3.1c are present - the maps filtered for the two bands are complementary, with the QD emission mostly occupying the perimeter of the scan and the QW emission localized to the centre of the scan window. Figure 3.4a iii shows the decay trace associated at the same sample position for both maps. The decay trace from the QDs can be fitted with a single exponential decay, convolved with a Gaussian to account for the instrument response function (IRF), limited by the response of the avalanche photodiodes and the electron pulse width. From our fits we extract that the bulk QD lifetime is 433 ± 1 ps. The decay of the QW emission on the other hand is fit with a biexponential equation, with a rise time, τ_{rise}, and two decay components of recombination rates τ_1 and τ_2,

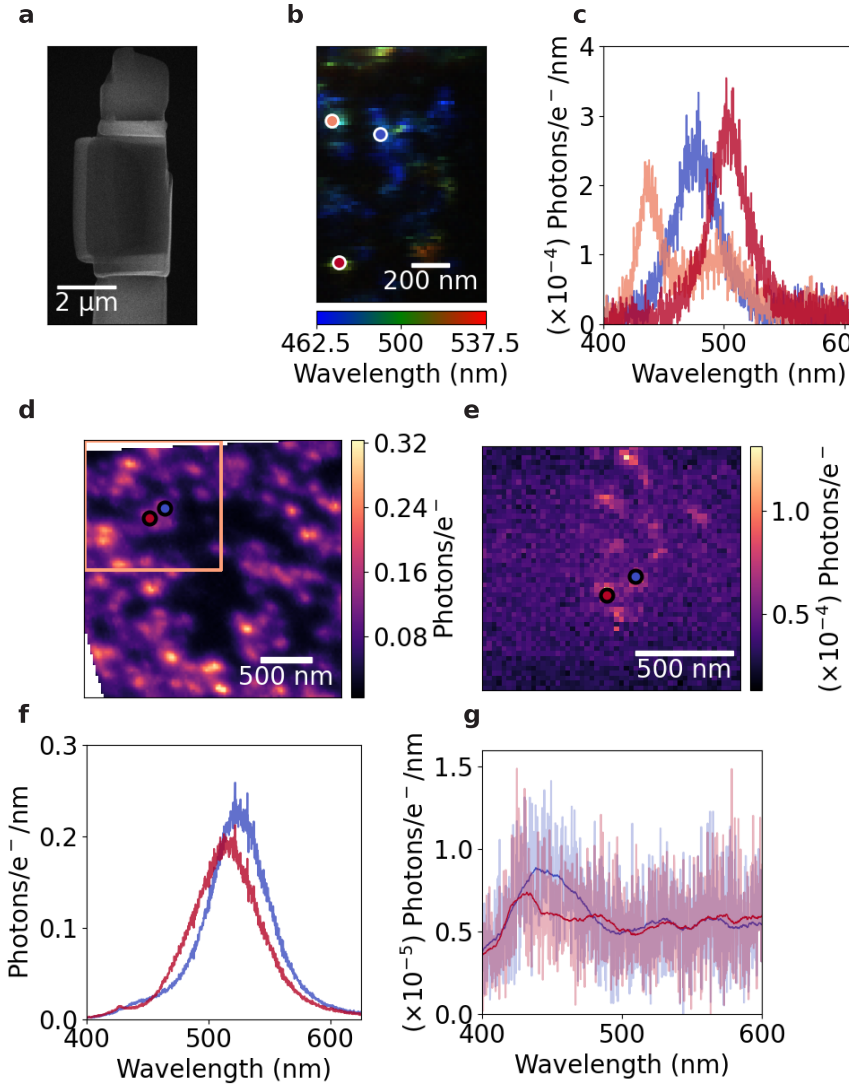

Figure 3.3: (a) SEM image of the plan view lamella sample. (b) False color RGB SEM-CL map with λ_c = 500 ± 37.5 nm, with spectra corresponding to marked positions plotted in (c). (d & e) CL maps with λ_c = 430 ± 5 nm of bulk and lamella sample respectively, with pixel sizes 10 and 25 nm. The orange box in (d) indicates the scan area in (e). The spectra from the same two positions of the sample in bulk and lamella configuration are plotted in (f) and (g).

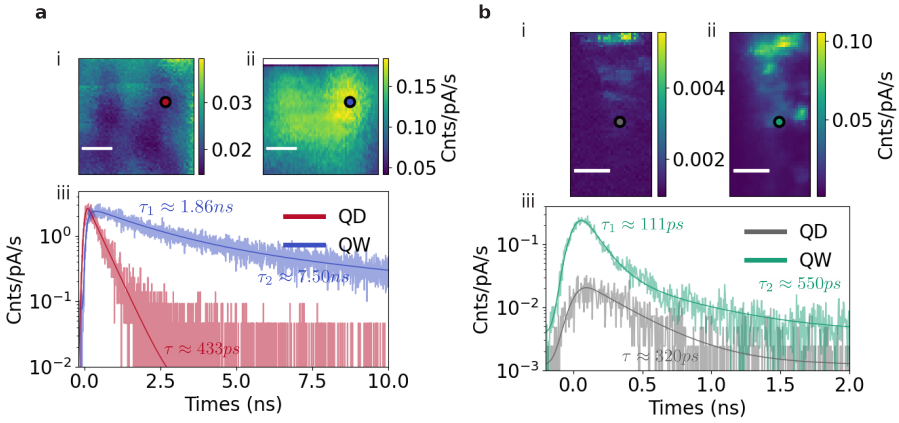

Figure 3.4: Comparing SEM-CL lifetime measurements of sample in (a) bulk and (b) lamella configuration. Intensity maps of 35 nm pixel size filtered for (i) $\lambda_c = 450 \pm 20$ nm, and (ii) $\lambda_c = 550 \pm 20$ nm emission, with markers representing positions of decay transients plotted in (iii). The scale bars are 500 nm in all images.

$$I_{QW,bulk}(t) = A_1 * (1 - e^{-t/\tau_{rise}}) * e^{-t/\tau_1} + A_2 * (1 - e^{-t/\tau_{rise}}) * e^{-t/\tau_2} \tag{3.1}$$

The results of the fits give $\tau_{rise} = 125 \pm 3$ ps , $\tau_1 = 1.864 \pm 0.031$ ns, and $\tau_2 = 7.495 \pm 0.136$ ns. The QW decay additionally has a high background because of the contribution from the yellow band emission tail of GaN, which has a lifetime in the μs range[139]. As a repetition rate of 10 MHz was used to maintain a high CL signal, the yellow band does not fully relax into its ground state and manifests as a background. Most studies fit InGaN QW recombination with a bimolecular function with a fast and slow decay, each associated with the recombination of free or weakly localized excitons, and strongly localized excitons respectively[140–142]. Similarly, the rise time of the QW peak has been previously attributed to carrier transport from weak localized states to stronger localized states[143, 144]. Our time-resolved measurements performed at liquid nitrogen temperatures (Supplementary Figure 3.4) also show that the lifetimes of both the fast and slow decay components increase, and by extension the risetime. The monomolecular QD emission imply a more uniform localization of carriers, with their smaller size increasing the e-h overlap and possibly leading to a reduction in the radiative lifetime[46, 145]. Conversely, the increased influence of the GaN surface in QDs, that has been demonstrated as a source of non-radiative defects, may also play a role in increasing the recombination rate of the QD[146].

The time resolved measurements following lamella preparation, filtered for QD and QW emission, are plotted in Figure 3.4b i and ii, with corresponding decay traces plotted in iii. The QD emission can still be fitted with a single exponential decay, and shows a reduction of lifetime to 320 ± 20 ps. The rise time of the

QW emission was reduced below the time-resolution of the experiment, and therefore could be fitted with a standard biexponential, resulting in fit parameters of about $\tau_1 = 111 \pm 7$ ps and $\tau_2 = 550 \pm 113$ ps . The decrease in lifetimes of both emission components is indicative of the introduction of non-radiative defects that quench and decrease the decay time of excited-state populations. FIB is known to introduce point defects, such as vacancies and interstitials, that are believed to generate deep-level trap states that promote non-radiative Shockley-Read-Hall recombination and quench luminescence[147]. The more pronounced quenching of QW emission, compared to QDs, can be attributed to different carrier confinement characteristics. QWs allow for lateral carrier diffusion, enabling carriers to migrate into nearby FIB-induced non-radiative recombination centres, and QDs exhibit three-dimensional confinement, localizing carriers and shielding them from defects. Despite the overall reduction in lifetime, these values still vary along the sample as can be seen in the fitted lifetime maps in Supplementary Figure 3.5.

Considering most lamellae are prepared from cross-sections of samples, we repeated our measurements on a cross-sectional lamella and tested if the optical properties are further influenced by the GaN/vacuum interface. By directly comparing the same area before and after lamella preparation (Supplementary Figure 3.6) we observed consistent results, with both plan- and cross-view configurations demonstrating the similar suppression of the QW component in hyperspectral CL measurements as well as comparable reduction in lifetime of both QD and QW emission components. However, nominally identical FIB parameters do not always exhibit identical changes in optical properties. Another plan-view lamella prepared from the same InGaN heterostructure under the same target environmental conditions, milling angles, and beam settings, showed less quenching of the QW emission, and different average recombination lifetimes (Supplementary Figure 3.7). This discrepancy highlights the sensitivity to subtle, uncontrollable factors, primarily the precision of sample and milling box alignment by FIB operators[148], and drift caused by beam and vacuum instability and sample charging effects. Interestingly, time-resolved photoluminescence (TR-PL) measurements on the lamella also filtered for QD and QW emission (Supplementary Figure 3.8) show a shorter lifetime than measured using CL. This discrepancy likely arises from differences in the excited carrier densities; the electron beam excites carriers throughout the GaN bulk that diffuse into the InGaN[149], whereas TR-PL at $\lambda = 397$ nm excites carriers directly within the InGaN.

3.5. CONCLUSIONS

In conclusion, this study demonstrates a nanoscale correlation of spectral, and time-resolved luminescence properties of an InGaN/GaN quantum well sample in both its bulk configuration and as FIB-lamellae. We observed that the spectra from bulk demonstrate two emission components, arising from the QWs and QD structures formed by the etching of the InGaN layer during fabrication. Our measurements demonstrated that while the QD emission is largely preserved, the QW emission is strongly quenched by lamella preparation, with a significant reduction

in lifetime. This effect is attributed to non-radiative defects introduced by the ion beam, which predominantly affect the QW emission due to the weak localization of carriers. Our further analysis of other lamellae prepared under nominally identical conditions of the same bulk sample reveal variable levels of optical quenching, emphasizing the irreproducibility of the artifacts introduced by the FIB. Future work should be wary of optically characterizing materials prepared as lamella without comparison to their bulk properties.

3.6. SUPPLEMENTARY

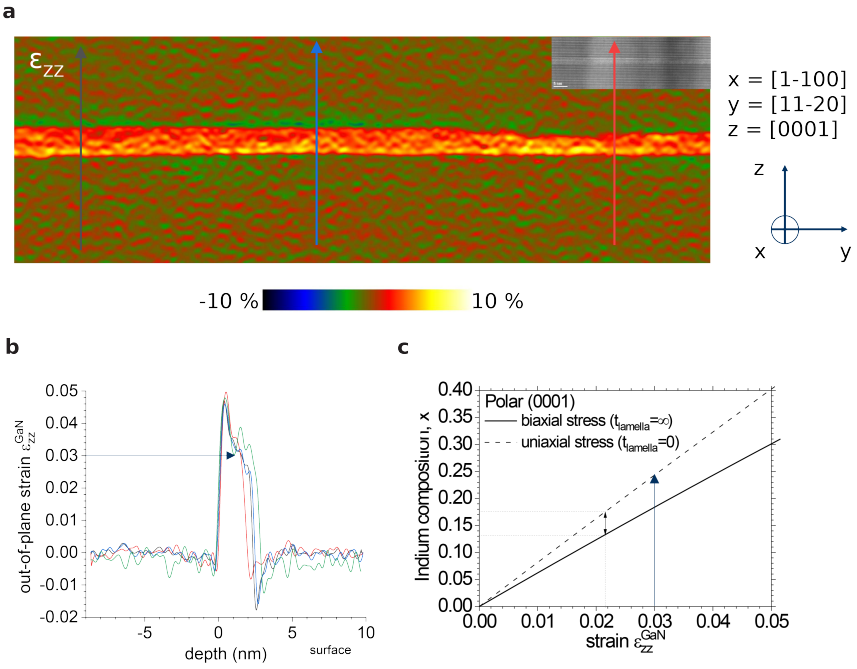

Supplementary Figure 3.1: Strain maps. (a) Normal strain component ϵ_{zz} in the z-direction, calculated using "Absolute strain" analysis from the 200 keV HAADF-STEM images in the inset. (b) ϵ_{zz} as a function of depth along three crosscuts through the InGaN layer, as indicated by the arrows in (a). (c) Indium composition as a function of ϵ_{zz}, calculated by applying Vegard's law.

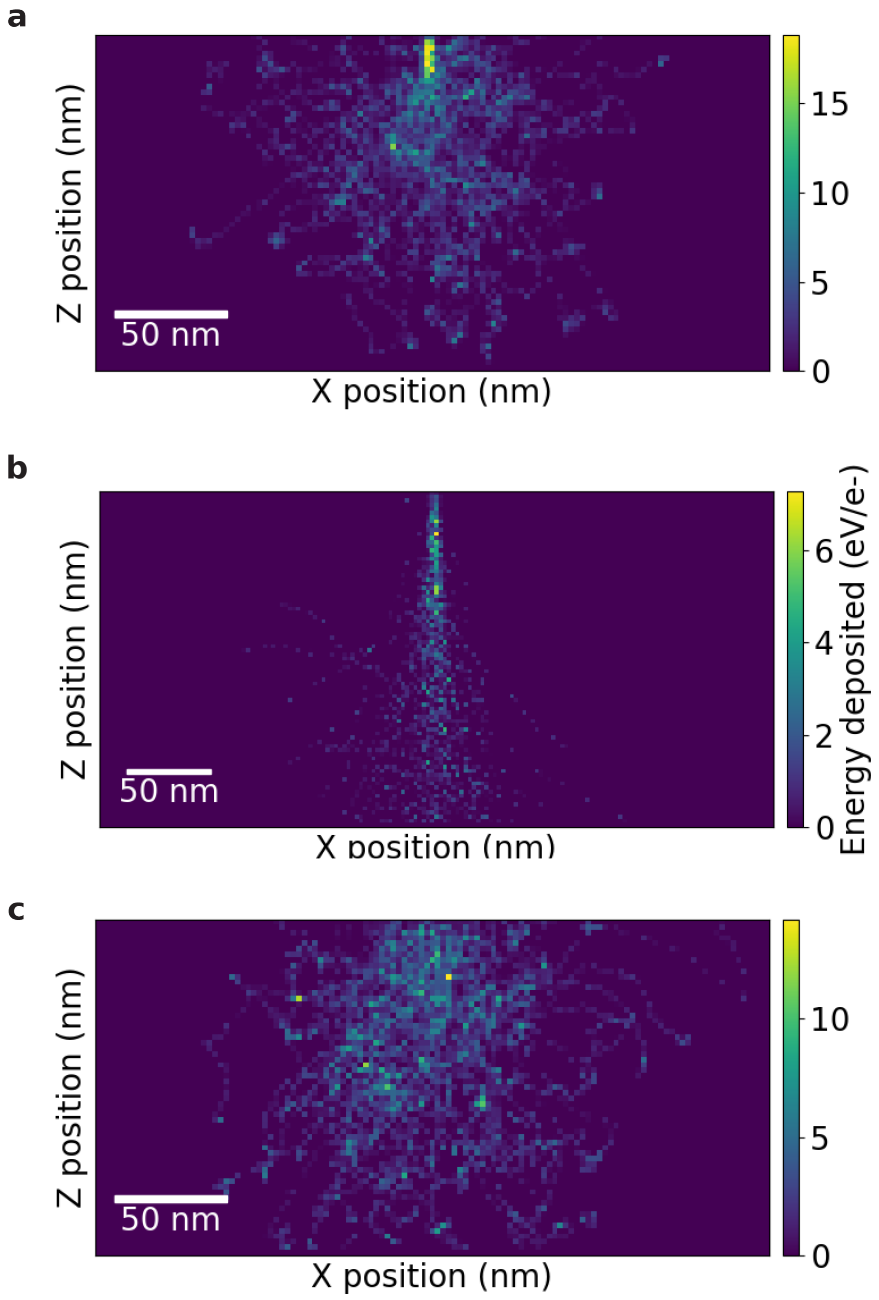

Supplementary Figure 3.2: V2.51 CASINO Monte Carlo simulations of (a) 5 keV and (b) 30 keV electron beams with beam waist of 5 nm diameter, planarly incident onto GaN (density = 6.15 g/cm^3) bulk and 200 nm thin film respectively. The simulation in (c) is of a 5 keV electron beam with beam waist of 100 nm diameter. The simulation volume was divided into cubic bins with side length of 2.5 nm, to calculate the energy deposited by unit volume per electron.

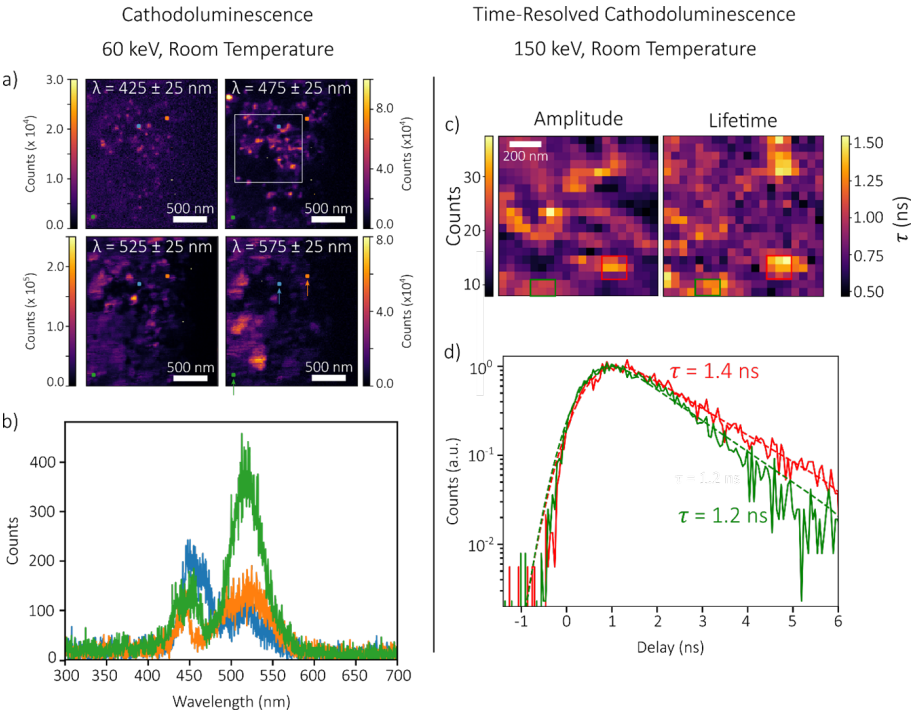

Supplementary Figure 3.3: Study of another plan view lamella from the same growth using transmission electron microscopy. (a) CL map in a scanning transmission electron microscope (STEM) at 60 keV and room temperature. We identified the two same emissions than in the main text. (b) Spectra extracted from the CL map, the pixels are represented by coloured point and arrows in (a). (c) and (d) Lifetime measurement in an ultrafast STEM at 150 keV at Room Temperature. The area studied is marked by a white square in (a). The decay traces have been fitted with the convolution of a Gaussian representing the IRF and a mono-exponential. The decay traces correspond to the two areas marked by coloured squares in (c).

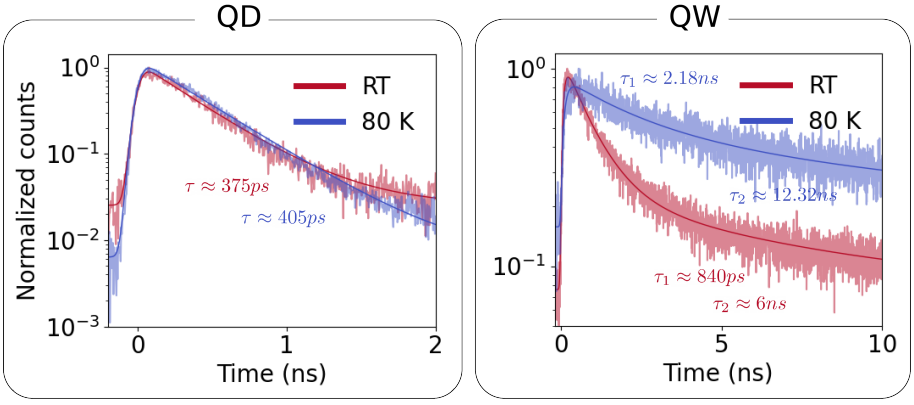

Supplementary Figure 3.4: Temperature dependent decay traces optically filtered for QD emission (left) and QW emission (right) using 40 nm bandpass filters centered at 450 and 550 nm respectively. The decay traces are averaged over several micron areas, at a different location on the bulk sample to measurements performed in the main text.

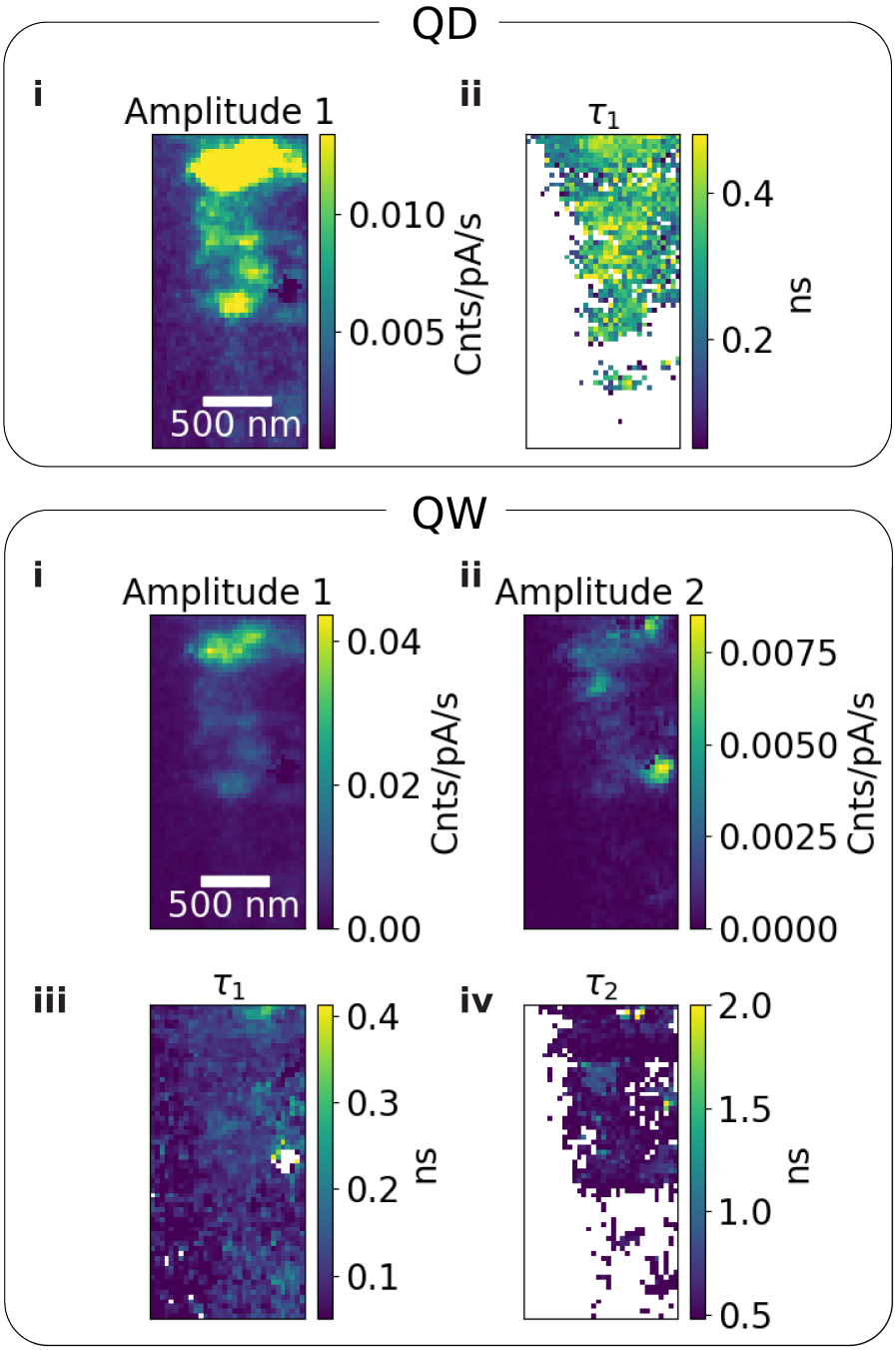

Supplementary Figure 3.5: Fitted TR-CL maps of plan view lamella sample filtered for (top) QD emission, where (i) plots the amplitude of the peak of the decay trace, and (ii) the recombination lifetime in ns. The same is plotted for QW filtered emission, with (i & ii) plotting the amplitude of the fast and slow decay components, and (iii & iv) plotting their respective recombination rates.

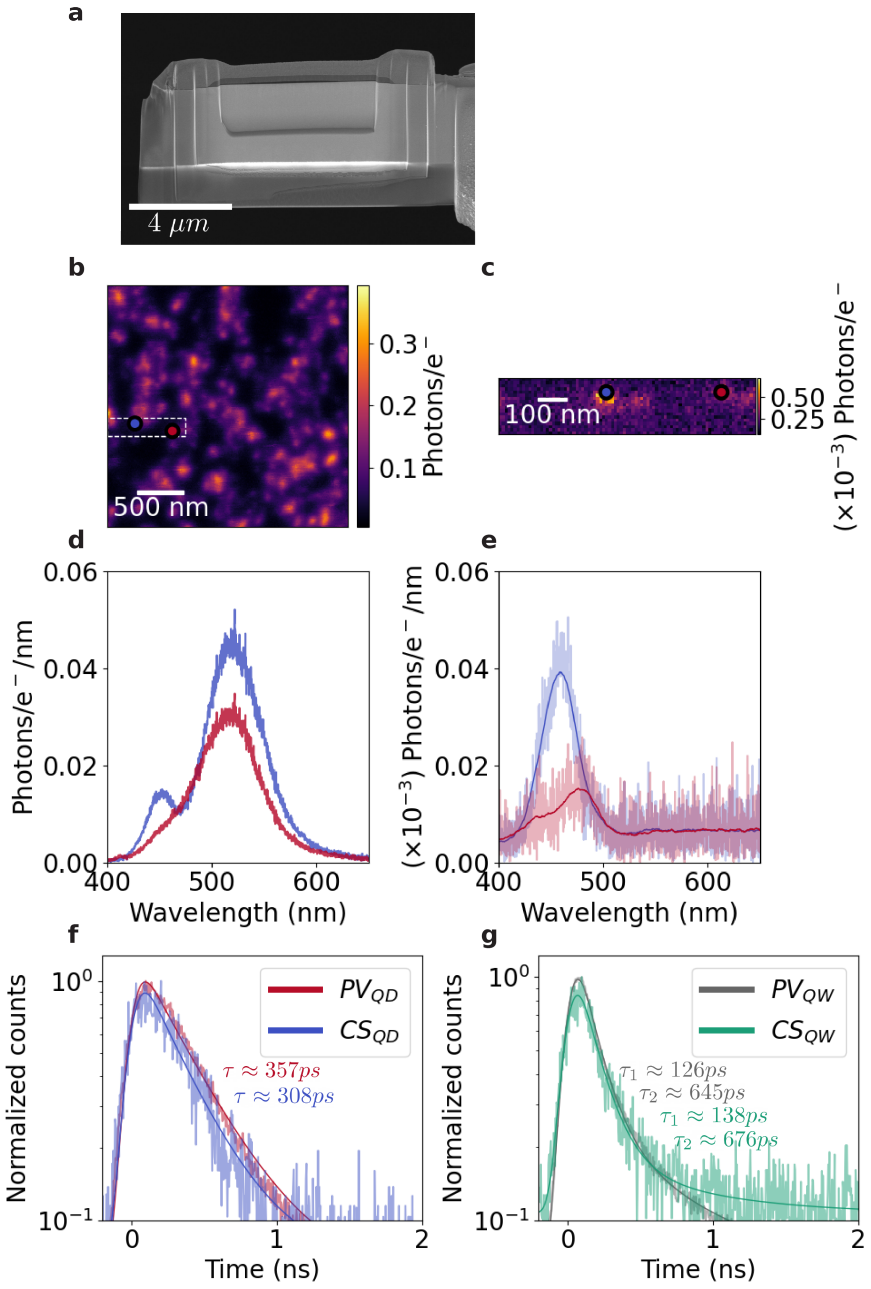

Supplementary Figure 3.6: Measurements on cross section view lamella. (a) SEM image of cross-section lamella sample. (b & c) CL maps with $\lambda = 430 \pm 5$ nm of bulk and lamella sample respectively, the dashed white box in (b) indicates the rough position where the sample was sliced into the cross-section in (c). The spectra from the same two positions of the sample in bulk and lamella configuration are plotted in (d) and (e). Average decay traces of (f) QD filtered emission and (g) QW filtered emission from plan view (PV) and cross section (CS) sample, demonstrating comparable levels of quenching in both lamella configurations.

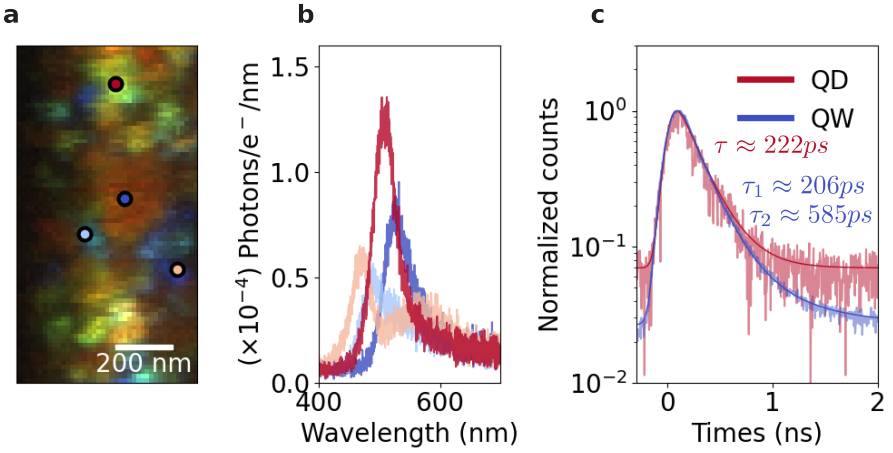

Supplementary Figure 3.7: Measurements on another plan view lamella with nominally identical FIB preparation. (a) Hyperspectral CL map centered at $\lambda = 500 \pm 37.5$ nm of plan view InGaN lamella fitted to RGB values, with spectra associated with each marked position plotted in (b). (c) Average decay traces filtered for QD and QW emission from this sample.

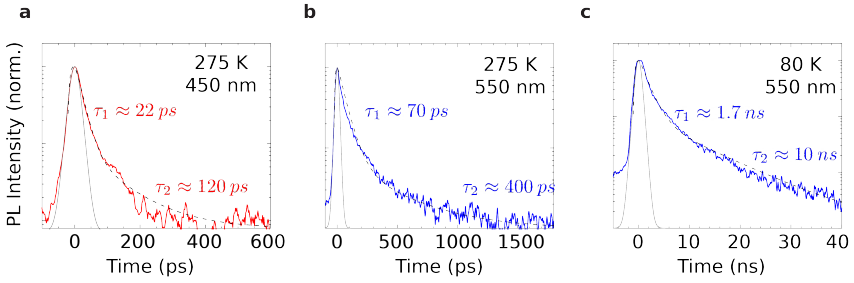

Supplementary Figure 3.8: Time-resolved photoluminescence lifetime measurements from plan view lamella studied in S7. (a) filtered at $\lambda = 450 \pm 20$ nm at 275 K; filtered at $\lambda = 550 \pm 20$ nm (b) at 275 K and (c) at 80 K. The IRF of our TR-PL setup using a streak camera are also plotted with a solid black line and differ as a function of the time window used.

Supplementary methods

(Time-resolved) SEM-CL:
The SEM-CL measurements were performed on a modified Thermo Fisher Quanta 650, equipped with a Schottky field emission gun and a Delmic SPARC optical detection system. Light was collected via a parabolic aluminium mirror with acceptance angle of 1.46π sr. For measurements on the lamella, a custom sample holder was used to minimize CL back-reflection from the holder. The spectra were corrected for the system's collection efficiency, which was measured by acquiring the transition radiation spectrum of aluminium and comparing it to its theoretically derived spectrum [150]. TR-SEM-CL measurements were performed by pulsing the electron beam using an electrostatic beam blanker. The blanking plates, spaced 0.25 mm apart, were driven by a square wave signal of 10 V, and 10 MHz repetition rate or 5 V, and 5 MHz repetition rate for a 30 and 5 keV electron beam respectively. For fully pulsed operation, the electron beam crossover was positioned between the blanking plates by adjusting the condenser lenses, resulting in pulses of about 35 ps (5 keV electron beam) and 175 ps (30 keV beam) widths. The luminescence was collected by the Delmic Sparc system, focused onto a 100 µm diameter multimode fibre, and guided to a time correlated single photon counting (TCSPC) module. Detection is performed with a PicoQuant PDM series avalanche photo diode (APD) and correlated using a PicoQuant PicoHarp 300 correlator, using the beam blanking signal as a trigger. To avoid pile up effects, the counts on the detector were limited to 0.001 photons per electron pulse using a neutral density filter.

TEM-CL:
CL-STEM experiments were performed on a Nion Hermes scanning transmission electron microscope operated at 100 keV, using an Attolight Mönch light collection/injection system, which uses an aluminium parabolic mirror. The vacuum-to-air interface in the optical system is made through a SiOx window. For optical spectroscopy, a Princeton Instrument Acton Series SP-2300 spectrometer (300 mm focal length) with a 150 lines/mm grating blazed at 500 nm was used. Light was coupled to the spectrometer a bundle of 100 µm core fibres and detected with a UV-enhanced ProEM EMCCD with 1600x200 pixels. Wavelength calibration was performed using an Ar/Hg standard lamp. The collection efficiency of the whole system as a function of wavelength was not calibrated. Samples for CL-STEM were cooled to approximately 100 K using a HennyZ single-tilt, liquid-nitrogen-cooled holder. For the CL-STEM experiments, the electron beam convergence angle was 25 mrad. The typical electron beam current was between 10 and 200 pA.

Time-resolved TEM-CL:
TRCL-STEM experiments were performed using an Ultrafast Transmission electron microscope, based on a modified Cold-FEG HF2000[151]. The tungsten tip was excited with a femtosecond laser to generate a pulsed electron beam by photoemission. The electron pulse width was approximately 400 fs, with a repetition rate of 2

MHz to allow complete relaxation of the system between pulses. The electron probe size was below 5 nm, and the current at the sample position was about 100 fA. The UTEM was operated at 150 keV. Cathodoluminescence signals were collected by a parabolic mirror and focused into a 600 µm diameter multimode fibre. The light was guided to an avalanche photo diode (Excelitas) and correlated using a PicoQuant TimeHarp260 PICO, using the laser output signal as a trigger. The count rate on the photo detector was approximately 50 cts/s. Five 1-hour scans were aligned and summed to obtain the dataset presented in Supplementary Figure 3.3. The IRF of the experiment is limited mostly by the detector time resolution (450 ps) and the modal dispersion in the optical fibre.

Time-resolved PL:
Time-resolved photoluminescence (TR-PL) experiments were performed on the lamella sample placed inside a low-vibration closed cycle He cryostat to adjust the temperature from T = 10 to T = 300 K. The sample was excited by a frequency-doubled mode-locked Ti:sapphire oscillator with ~ 1.5 ps pulses and a wavelength of 397 nm. A pulse picker was used to reduce the repetition rate down to 4 MHz. The typical size of the excitation/detection spot in the micro-TR-PL experiments is 1 mm. The time-resolved spectra and kinetics are recorded with a Hamamatsu S20 photocathode streak camera coupled to a spectrometer. The streak was used either in triggered mode with an overall instrument response time resolution (IRF) of ~ 1 ns or in synchroscan mode to achieve an overall instrument response time resolution (IRF) of ~ 20 ps.

4

NANOSCALE CL STUDY OF GAN NANOWIRE LASING

In this work, a scanning electron microscope (SEM) combining time-resolved cathodoluminescence (TR-CL), secondary electron imaging, and optically pumped lasing measurements enables comprehensive characterization of individual GaN nanowires in a single microscope. Temperature-dependent CL and TR-CL using 30 keV electrons is first used to provide direct insight into the optical properties of the gain medium. These measurements reveal non-monotonic spectral shifting and temperature -independent lifetimes, demonstrating that recombination is limited by nonradiative surface defects and that exciton localization to shallow defects impact emission. It was then investigated how cavity gain influences the lasing threshold. When transferred onto a uniform Si substrate, nanowires with a larger length/width aspect ratio exhibited systematically lower thresholds. In contrast, nanowires on a nonuniform lacey carbon TEM grid exhibit no systematic dependence on geometry, highlighting how local substrate/environment conditions strongly affect the lasing threshold and can dominate over nanowire geometry. Finally, the impact of electron beam irradiation on the lasing characteristics of the nanowires was examined. While the lasing threshold of the primary mode remained unchanged upon 30 keV electron irradiation, the number and relative intensity of higher order modes were altered, suggesting that the electron beam perturbs local gain and reshapes mode competition. Together, these results demonstrate how an integrated SEM-CL platform can provide fundamental insights into semiconductor nanowire lasers at the nanoscale.

4.1. INTRODUCTION

Semiconductor nanowire (NW) lasers, where the nanowire functions as both the gain medium and a Fabry-Perot type cavity, have gained significant attention for applications in miniaturized integrated optoelectronic devices. Breakthrough work using ZnO[152], followed closely by work on GaN[153] NWs, showed how the NW geometry supports strong optical confinement, using the high reflectivity due to the refractive index contrast between the semiconductor and free space at the end facets to create an effective cavity. While ZnO remains an important material for nanolaser studies, the relative ease of integrating III-V semiconductors with Si technology make GaN a particular material of interest[154] as well. Since the first proof of principle, research has explored a wide range of architectures including single-mode GaN lasers[155–157], electrical modulation of GaN NWs[158], and InGaN/GaN electrically pumped nanolasers[159]. Despite the demonstration of these elegant devices, large-scale measurements on III-V NW-based lasers show that there are inhomogeneities in geometry and material composition of individual NWs[160–162]. Given that lasing properties are directly related to these properties, as well as their local environment, studying individual GaN NWs offers valuable insights.

The GaN NWs used in this study were prepared by B. Damilano from CREHA using a top-down fabrication method described in ref [163, 164]. Bulk GaN was grown on a (0001) sapphire substrate using metalorganic chemical vapor deposition (MOCVD). This was done in two phases to optimize the nucleation of the GaN to the substrate. First, 2 μm of unintentionally doped GaN was grown, followed by 5 μm of a Si-doped (5×10^{18} cm^{-3}) GaN layer. The GaN was then patterned with a nanoscale mask of SiO_x nanodots using displacement Talbot photolithography through an optical mask of hexagonally arranges holes. By controlling the mask dimension and dose, the diameters of the SiO_x nanodots could be varied. The sample was then etched using selective-area sublimation (SAS), i.e. exposure to a high-vacuum and high-temperature oven that sublimates the material, forming hexagonal arrays of vertical 7 μm long GaN NWs, as depicted in Figure 4.1a. The main benefit of top-down fabrication with SAS is the precise control of geometry over large areas, which can be directly applied to high-quality bulk GaN without having to develop new bottom-up growth methods. Moreover, SAS is low-cost, easily scalable, and because it relies on sublimation rather than ion-based etching, it avoids ion-induced damage to the NW surface. The NW samples have been shown to lase at room temperature[163] under optical pumping, however, the reported PL spectra measurements represent ensemble-averages over large areas of the array. While this provides useful information about device performance, it obscures variability between individual NWs. This measurement can be achieved by first transferring the NWs to a substrate, imaging, isolated NWs using electron microscopy, and then transporting them to an optical set-up for PL measurements, as demonstrated in Figure 4.1b. Besides the lasing spectrum, a key lasing property is the lasing threshold, the pump power density at which a sharp increase in emission intensity and narrowing of emission linewidth occurs, signaling the transition from spontaneous to stimulated emission. This threshold can be determined from the characteristic

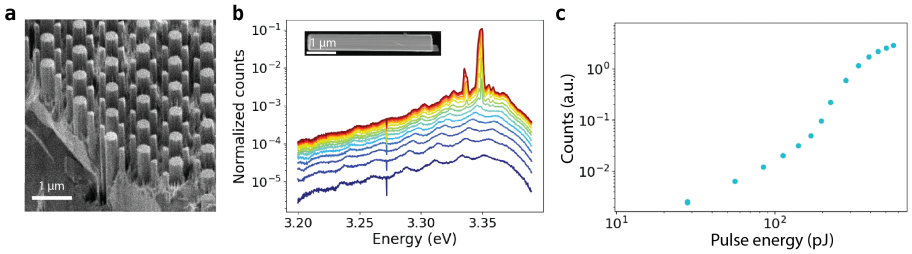

Figure 4.1: (a) SE image at a 45 °tilt of a crosscut of the bulk GaN nanowire sample fabricated using SAS. (b) Lasing photoluminescence spectra from the shaved NW depicted in the SE inset image, at different optical pumping energies ranging from 28 to 562 pJ. The experiments were performed by C. Santini in μ-PL set up in the group of T. Guillet at the Laboratoire Charles Coulomb in Montpellier, using a pulsed laser source with $\lambda = 355$ nm, pulse length of 4 ns, repetition rate of 7 kHz, and a spot diameter between 1.1 - 1.6 μm. Inset: SEM image of the single NW. (c) Fitted amplitude of the main lasing peak in (b) as a function of pumping energy.

S-shaped curve in a log-log plot of emission intensity as a function of pump power, as depicted in Figure 4.1c.

However, characterizing individual nanolasers using electron microscopy for structural analysis followed by optical measurements in a separate PL set up is tedious and can introduce alignment errors or environmental changes. In this work, we exploit the light-incoupling capabilities of our time-resolved SEM-CL set-up to perform hyperspectral CL, TR-CL, and PL measurements on the same sample. This approach allows us to directly visualize NW geometries at nanoscale spatial resolution, link this to macroscopic lasing behaviour, and gives us access to nanoscale spontaneous emission properties using CL to characterize the material.

4.2. TEMPERATURE-RESOLVED CL ON A SINGLE NANOWIRE

The performance of a NW laser is fundamentally governed by the gain coefficient of the semiconductor, that is determined by the electronic band structure of the material [165, 166]. Although manipulating the gain coefficient is not an option for optimizing devices, the quantum efficiency of a given nanowire is strongly influenced by the presence of defects of which the nature and density can vary depending on fabrication methods. As defect-assisted non-radiative recombination channels in a material directly compete with radiative processes, this can reduce the net material gain. Thus, it is essential to probe the emission properties of individual NWs to assess their variability. By employing hyperspectral CL, we can study radiative spectral properties such as band edge emission and defect related radiative channels, whereas TR-CL adds dynamic information about carrier lifetimes.

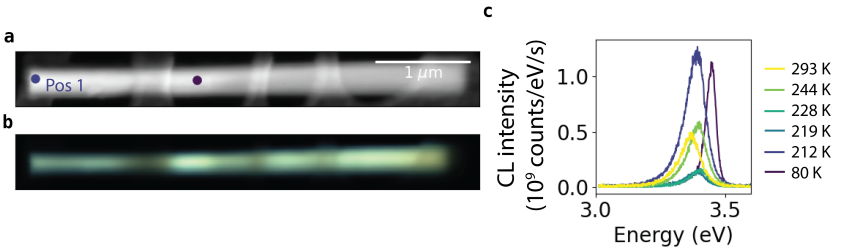

Figure 4.2: 30 keV CL spectra at different temperatures for a single nanowire. (a) SE image of the nanowire on a lacey carbon membrane with (b) a concurrent room-temperature CL map at $\lambda = 369 \pm 5$ nm fitted to false color RGB values. (c) CL spectra as a function of temperature at position 1 indicated on (a).

4.2.1. HYPERSPECTRAL

We first characterized an individual GaN NW shaved from the bulk sample onto a lacey carbon TEM grid using hyperspectral CL for different temperatures, as summarized in Figure 4.2. Temperature-dependent optical studies provide insights into band structure, exciton dynamics, and the role of defects in recombination. Typically at low temperatures, phonon interactions are suppressed, leading to enhanced excitonic emission with narrow linewidths, while defect-related non-radiative pathways are deactivated[167]. Our measurements were performed using a 30 keV electron beam, for maximal spatial resolution, and a liquid-nitrogen cooled stage with the sample thermally coupled to the stage using silver paste. The stage temperature is read with a precision of ±1 K, and the sample was left to equilibrate for ~ 15 minutes at each temperature before acquisition. Figure 4.2a shows the SE image of the nanowire positioned on the lacey carbon support, with the concurrent, room-temperature false-color RGB CL map with $\lambda = 369 \pm 5$ nm in Figure 4.2b. Due to the high acceleration voltage of the electron beam, we can image the support film through the NW. The CL map demonstrates that the carbon optically quenches part of the CL emission, attributed to carbon adsorption-induced surface recombination [168]. Furthermore, the right-end side of the NW shows a small relative redshift of approximately 0.35 eV that we attribute to the variation in doping during growth[169].

Figure 4.2c shows temperature-dependent CL spectra recorded at a fixed position labeled Pos. 1 in Figure 4.2a, recording the evolution of the emission from room to liquid nitrogen temperature. Interestingly, the peak energy of the emission from this nanowire does not monotonically blueshift with decreasing temperature (as anticipated for semiconductors due to the contraction of the lattice, described by Varshni's equation[170]). At 293 K, the emission is centered at approximately 3.37 eV. As the temperature is reduced to 244 K, the emission blueshifts to 3.4 eV, consistent with bandgap shrinkage due to lattice contraction. Further cooling to 228 K yields no shift in peak energy, however, the emission intensity is reduced by 70%. To a degree, this can be influenced by variations in system alignment between measurement sessions, however, these variations typically do not exceed 30% [171].

As the temperature is decreased to 219 K, the peak energy redshifts to 3.39 eV with a further decrease in amplitude. Cooling further to 212 K produces a steep intensity increase, and finally at 80 K the spectrum blueshifts to 3.45 eV. This irregular progression in the emission energy indicates the presence of multiple competing radiative channels that are strongly temperature dependent. In GaN, it is well established that below ~ 50 K, emission originates from donor-bound excitons that then transition to free exciton emission at higher temperatures[172, 173], a feature also observed in Si-doped GaN[174]. While our cooling stage cannot access those cryogenic temperatures, further measurements plotted in Figure 4.3 point to excitons localized to another defect state in this nanowire. Notably, previous studies from our lab on similar nanowires showed a strictly monotonic blueshift with decreasing temperature, consistent with Varshni's model [16].

Evidence for such a defect-related radiative channel emerges from the hyperspectral measurements performed at 212 K and 219 K. Figure 4.3a shows the spectrum acquired at the position labeled Pos. 2 on the NW depicted in the SE image in Figure 4.3b. Compared with spectra from other positions and temperatures, this spectrum exhibits an additional emission peak, that is found by fitting the spectrum with a sum of three pseudo-Voigt functions. We attribute Peak 3 to the near-band edge (NBE) free exciton emission [175] that shifts with position along the nanowire, and Peak 1 to its phonon wing[176, 177]. Peak 2 is the additional peak that we observe, that we attribute to a shallow defect within the bandgap. To examine the spatial distribution of each component, the three-peak fitting model was applied to every pixel in the hyperspectral CL dataset. The resulting amplitude maps of each peak are plotted in Figure 4.3(c-e). These maps reveal that a radiative defect is localized to the central region of the nanowire. As this defect is absent in previous measurements of the nanowires, it indicates it is not a universal feature of the material. One explanation is that it arises from the growth of the GaN material in two different doping phases, that could introduce point defects at the interface. Further research is needed to investigate this.

4.2.2. LIFETIME MAPPING

To determine whether the thermally activated radiative defect (peak 3) resulted in changes in carrier recombination dynamics, we performed TR-CL measurements on the same nanowire as a function of temperature using the electrostatically beam-blanked set up described in Chapter 3. Figure 4.4(a-c) shows lifetime maps at three representative temperatures: 293 K, 200 K, and 80 K. The decay traces were fitted with a sum of two exponential decays convolved with a Gaussian instrument response function (IRF), consisting of a dominant fast component of 65 - 75 ps, and a weak longer component of 200 - 300 ps. At each temperature in Figure 4.4, we plot (i) the short lifetime component and CL intensity as a function of position along the length (x-axis) of the NW, (ii) the CL intensity map and (iii) the fitted short lifetime map. Despite the substantial spectral changes observed in the spectral data, the measured lifetimes remain essentially unchanged across all temperatures. We note, however, that the extracted lifetimes are comparable to the

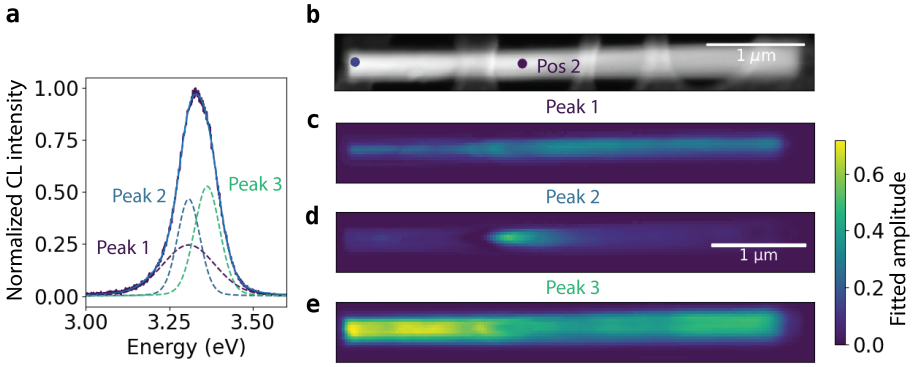

Figure 4.3: (a) Normalized CL spectrum at T = 212 K at position 2 indicated on SE image of nanowire in (b), with fitted Pseudo-Voigt emission components. (b) SE image of the NW on a lacey carbon membrane, the same NW as studied in Fig 4.2. (c-e) Maps of fitted amplitudes of the three emission components indicated in (a).

IRF of our set up, which is determined by the timing resolution of the avalanche photodiode used. Although it is often quoted that lifetimes as short as 1/10 of the IRF full-width-half-maximum (FWHM) can be recovered through fitting the convolution function[178, 179], a variation of the lifetime may still not be resolvable in our measurements due to limited signal to noise. Nevertheless the lack of lifetime increase with decreasing temperature, behavior typically observed in semiconductors as non-radiative channels become inactive due to a thermal barrier, suggests that the recombination is limited by temperature-independent non-radiative surface defects as has been reported in GaN previously [146, 180].

To test whether the recombination was limited by surface states, we measured the average decay transients as a function of NW diameter, as plotted in Figure 4.5a. An example of the decay trace with a bi-exponential decay fit is plotted in Figure 4.5b. As is clear in Figure 4.5c, thinner wires display systematically shorter lifetimes than thicker wires. This inverse dependence on diameter is the signifier of surface limited recombination[181], as the thinner the NW, the larger the surface to volume ratio and effect of surface defects. In the following section, we examine how these same NWs perform as optical gain media by studying their lasing characteristics under optical pumping.

4.3. LASING UNDER OPTICAL PUMPING

4.3.1. ASPECT RATIO

As mentioned previously, each NW functions as a Fabry-Perot cavity, with the end facets acting as partially reflecting mirrors. In such a cavity, the lasing threshold is reached when the modal gain, g_{modal}, experienced by light propagated by the cavity exceeds the round-trip losses[182],

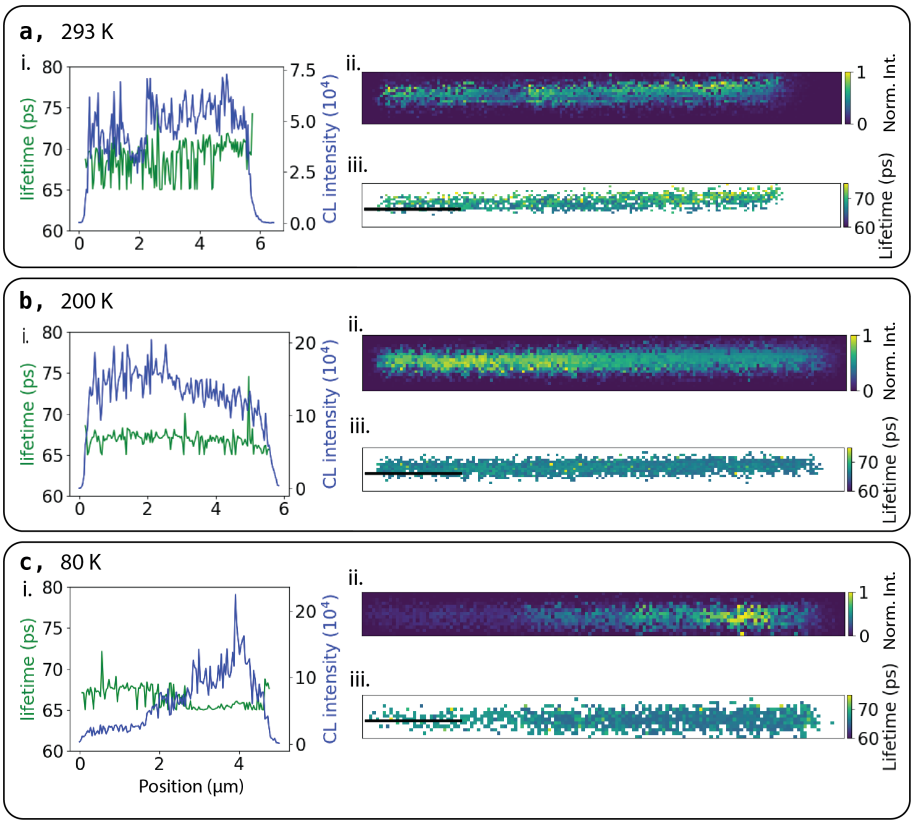

Figure 4.4: TR-CL measurements on the same single GaN NW at different temperatures. (a) T = 293 K, (b) T = 200 K and (c) T = 80 K. For each temperature we plot maps of (ii) the normalized CL intensity integrated over all wavelength of the bandpass filter ($\lambda = 370 \pm 18$ nm), and (iii) the fitted decay lifetime maps. The lifetime was only derived at positions with sufficient CL intensity. In (i), we plot the average lifetime and CL intensity as a function of position along the length of the same nanowire studied in Figure 4.2. The scale bars in the plots correspond to 1 μm.

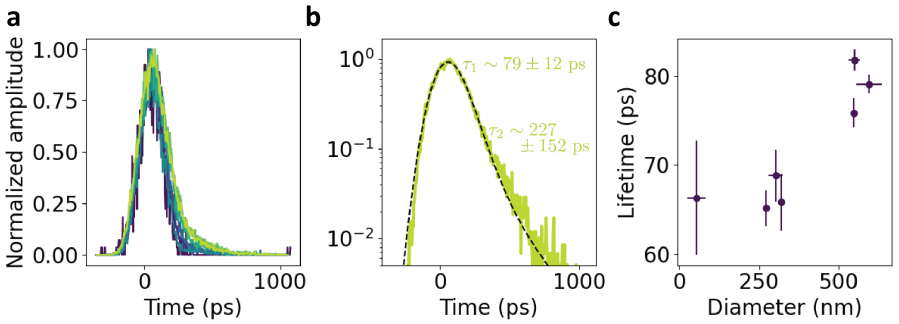

Figure 4.5: (a) Average decay transients of seven different nanowires of increasing diameter from d = 53.5 ± 28.5 nm to d = 594 ± 40 nm. (b) Measured decay trace from NW with d = 594 ± 40 nm, with bi-exponential decay fit and extracted fast and slow lifetime components indicated. (c) Lifetime (fast component) as a function of NW diameter.

4

$$g_{\text{modal}} > \alpha_{\text{mirror}} + \alpha_{\text{loss}} = \frac{1}{2L}\ln(\frac{1}{R_1 R_2}) + \alpha_{\text{loss}} \tag{4.1}$$

where α_{mirror} represents the mirror losses, $\alpha_{\text{loss}}$the material absorptivity, L the length of the cavity, and R_1 and R_2 the reflectivities of the end facets. From this equation, it follows that increasing NW length decreases the lasing threshold. The cavity length also controls the longitudinal mode spacing, $\Delta\lambda$, defined as[154],

$$\Delta\lambda = \frac{\lambda^2}{2n_{\text{eff}}L} \tag{4.2}$$

where n_{eff} is the effective refractive index. As a longer NW leads to smaller mode spacing, this allows more modes to fit within the gain spectrum, which can further decrease the lasing threshold. However, there is a trade off in cavity. Ultimately, if L gets too long then material propagation losses start to dominate and increase the lasing threshold again.

The NW diameter, d, influences the lasing threshold in three ways. Firstly, a larger diameter increases the fraction of the optical mode overlapping with the gain medium, Γ_0. This in turn increases the optical confinement factor, Γ, and therefor g_{modal}, according to the relation[183],

$$g_{\text{modal}} = \Gamma \times g_{\text{material}} = \frac{n_g}{n_b}\Gamma_0 \times g_{\text{material}} \tag{4.3}$$

where g_{material} is the material gain, n_g is the group index, and n_b is the refractive index of GaN. At larger diameters, the optical mode is better confined to the material, thereby decreasing the lasing threshold. Secondly, a larger diameter reduces optical diffraction at the end facets and increases reflectivity, lowering the mirror loss term in Equation 4.1[184]. Thirdly, efficient optical excitation of the cavity requires a good overlap between the pump beam and NW cross-section. For small

diameters, a significant fraction of the pump light is not coupled into the NW and reduces the carrier density generated per unit of power. However, if the NW diameter becomes much larger than the pump wavelength, the excitation of higher-order transverse modes and mode hopping may become significant.

To investigate how geometry influences optical gain in our GaN NWs, we measured the optically pumped lasing threshold of the same NWs studied in Figure 4.5. The NWs were transferred onto a Si substrate to maintain a uniform dielectric environment, and are depicted in the SE images in Figure 4.6(a-f) in order of decreasing aspect ratio (diameter/length). Because the NWs are slightly tapered, their diameters were defined as the average between the diameter of the two end facets. The optical pumping and detection measurements were performed using an optical set up integrated with our SEM-CL system in Figure 2.1. The same Al parabolic mirror used for CL outcoupling was employed to incouple and focus the pump beam from a frequency-tripled Nd:YAG laser (InnoLas Picolo, λ = 355 nm, 1.4 ns pulse width, 1 kHz repetition rate) to a spot size of $\sim$ 10 μm diameter on the sample[99]. The incident pump energy was varied between 0 to 30 μJ per pulse using a gradient neutral-density filter. The emission from the NWs was collected by the parabolic mirror, collimated, and focused into a 550 μm core multimode fibre, which guided the signal to a Czerny-Turner spectrograph (Princeton Instruments Spec10, 1200 lines/mm, blaze 500 nm). A $\lambda > 355$ nm long-pass filter was inserted to block scattered pump laser light. For each nanowire, emission spectra were recorded as a function of pump power to determine the lasing threshold. This procedure was performed for all NWs, however, Figure 4.6 plots representative results for three of the NWs depicted in panels (a), (d), and (f). In Figure 4.6 (g), emission spectra are plotted for increasing pump powers on a linear intensity scale, in (h) on a log-log scale, and (i) presents the fitted amplitude of the dominant lasing peak as a function of pump power. Because the pump power steps were relatively coarse compared to a dedicated μ-PL set-up, the resulting amplitude power plots do not allow precise S-curve fitting. Instead, the lasing thresholds were estimated from the pump level at which the emission linewidth narrowed and peak intensity increased sharply. Despite the coarse sampling of pump powers, the estimated lasing threshold plotted as a function of aspect ratio in Figure 4.7(c), shows a clear trend. NWs with a larger aspect ratio (d/L) exhibit systematically lower lasing thresholds. To separate the contributions of diameter and length we examined the threshold as a function of each parameter individually. This comparison showed that the trend is correlated with diameter (Figure 4.7b), confirming the geometric dependence anticipated from theory, as increasing diameter enhances the optical confinement and pump incoupling, thereby decreasing the threshold. In contrast, no correlation is found for the threshold and NW length (Figure 4.7a). Within the geometry range studied we do not reach the regime where further increase in size would lead to higher thresholds. The single apparent outlier in Figure 4.7, is the data point with the largest aspect ratio, shown in red and corresponding to the NW in panel (a). Upon closer inspection, this sample actually consists of two NWs stacked together, effectively increasing scattering, reducing cavity quality. This explains why its high lasing threshold is an anomaly compared to the trend.

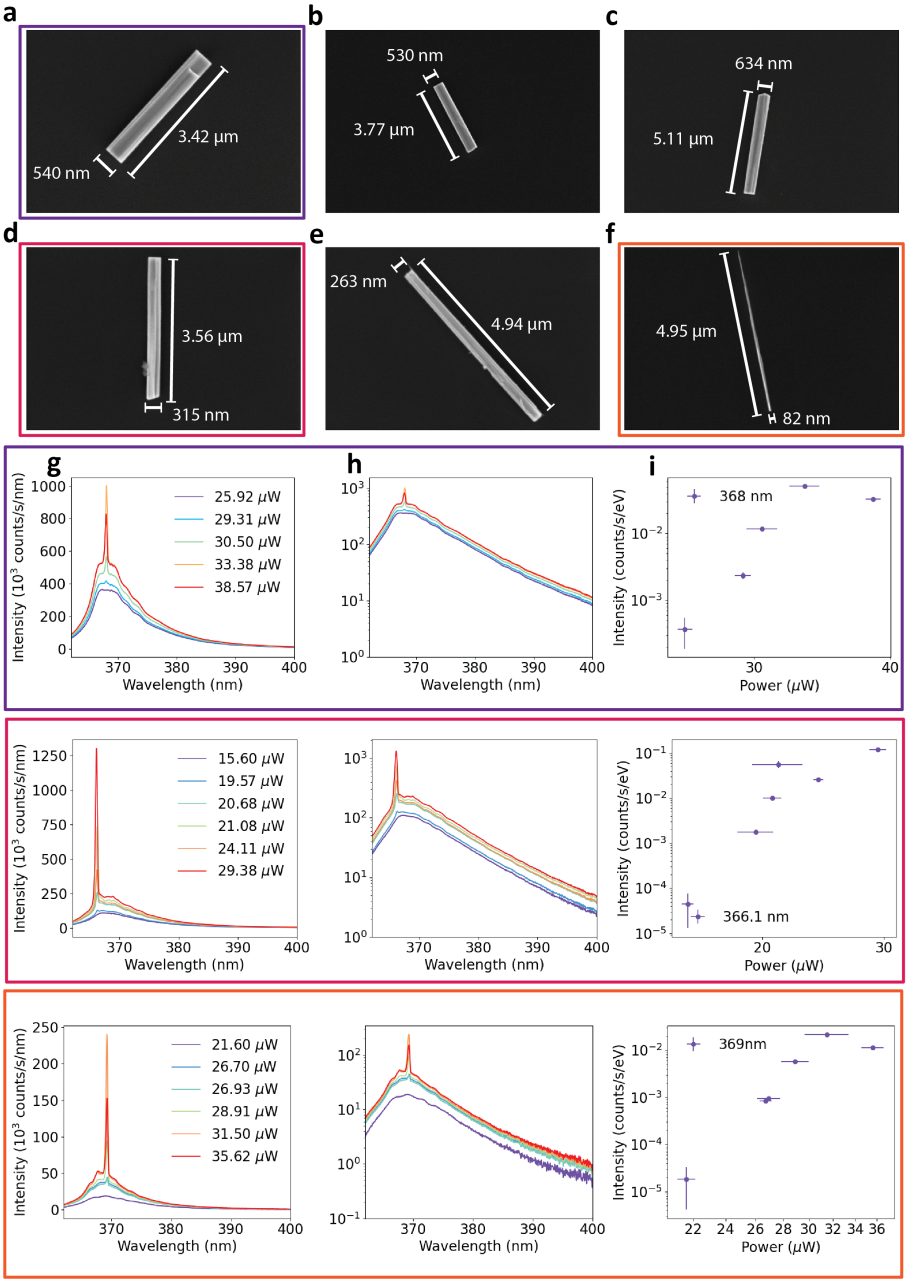

Figure 4.6: (a-f) SE images of shaved GaN NWs on a Si substrate, in order of decreasing aspect ratio. Lasing spectra of three nanolasers depicted in (a), (d), and (f) respectively are plotted on a (g) linear scale, (h) log scale, and as (i) fitted peak intensities. Prior to fitting, the spectra were converted from wavelength to energy (eV) scale by applying the Jacobian transformation[185]. The lasing wavelengths are indicated in (i).

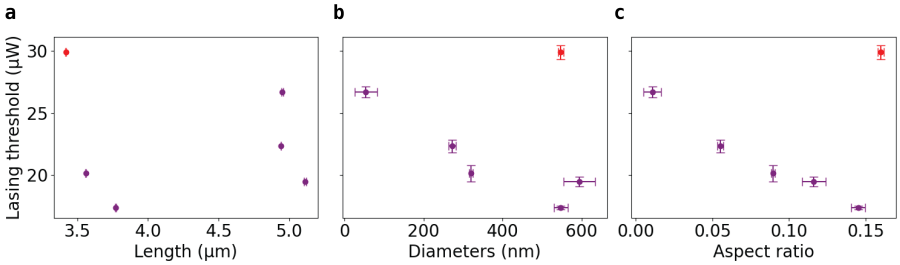

Figure 4.7: Lasing threshold as a function of nanowire (a) length, (b) diameter, and (c) aspect ratio (diameter/length) of each NW depicted in Figure 4.6. The red data point corresponds to two NWs stacked together.

This result hints that beyond the importance of nanowire geometry in determining the lasing threshold, the surrounding environment also has a strong influence. In realistic device configurations, the NWs are not isolated in vacuum or air but are embedded in or in contact with another medium, strongly influencing their optical properties as will be discussed in the next subsection.

4.3.2. SUBSTRATE

The influence of the substrate on NW lasing can be understood using the same cavity theory introduced previously, as the surrounding medium of the cavity affects both the the mirror losses, α_{mirror}, and confinement factor, Γ. As reflectivity on the end facets depends on the excited mode and the refractive index contrast between GaN and the external medium[184]. A low-index surrounding confines the mode more strongly, whereas higher-index or metallic substrates allow the optical field to leak into the substrate and reduces the overlap of the mode with the gain medium, which in turn reduces the end facet reflectivity [154]. Absorption of the evanescent fields can furthermore introduce additional non-radiative losses.

Therefore, we also studied NWs shaved onto a lacey carbon TEM grid, where individual wires rest either on the carbon support film or uneven copper regions. SE images of the individual NWs are plotted in order of decreasing aspect ratio in Figure 4.8(a-h). As previously, the emission spectra as a function of pump power were recorded for each NW, however, we plotted the results for two representative NWs from Figure 4.8 (a) and (g) respectively. In Figure 4.8 (i) emission spectra are plotted for increasing pump power on a linear scale. In (j) on a log-log scale, and (k) shows the fitted amplitude of the dominant lasing peak as a function of power. As for the NWs on the Si substrate, the lasing threshold was estimated from the excitation level at which emission linewidth narrowed and peak intensity increased sharply. For two of the NWs, in panels (e) and (h), the lasing threshold was not reached before laser induced damage took effect. The lasing threshold of the remaining NWs was plotted as a function of aspect ratio in Figure 4.9. Unlike in the case of the NWs on Si, the lasing threshold shows no systematic dependence on aspect ratio. This absence of geometric trend indicates that the additional losses in-

troduced by the substrate dominates the effects of the NW aspect ratio. Even among the NWs located entirely on copper, no trend is observed. This suggests that the degree of optical coupling to the metallic substrate varies from wire to wire, likely due to differences in local contact area/surface roughness, which produces variation in threshold.

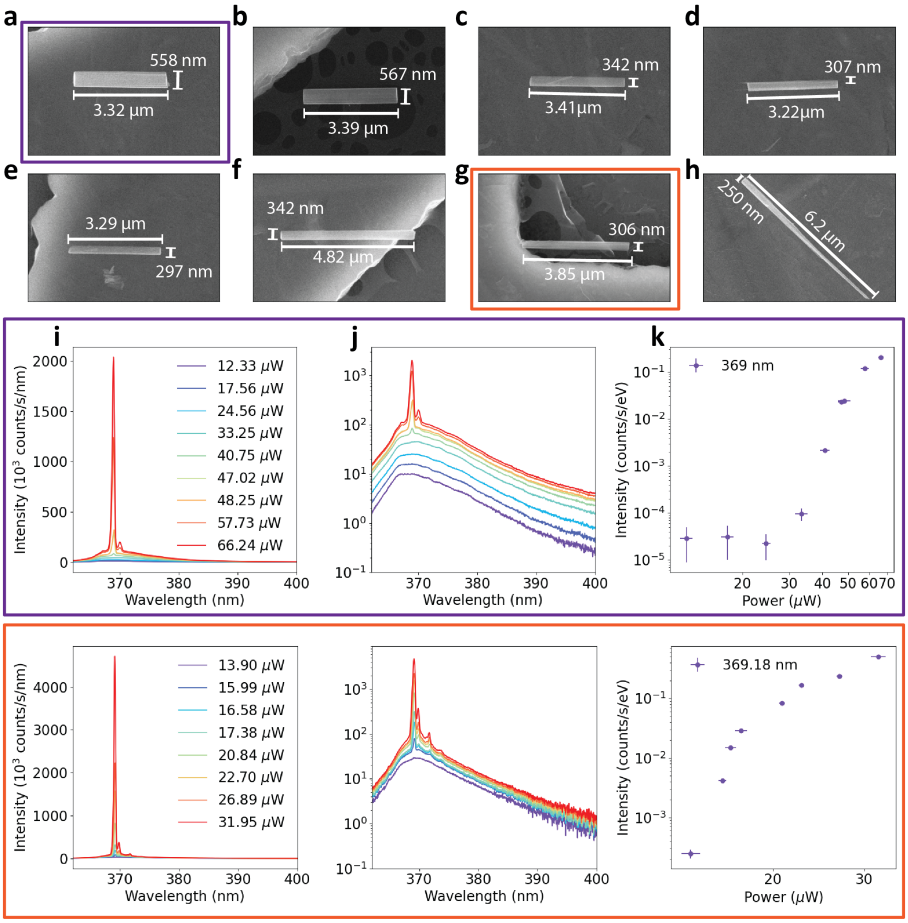

Figure 4.8: (a-h) SE images of shaved GaN NWs on a lacey carbon TEM grid, in order of decreasing aspect ratio. Lasing spectra of two nanolasers depicted in (a) and (g) respectively are plotted on (i) linear scale, (j) log scale, and as (k) fitted peak intensities. Prior to fitting, the spectra were converted to an eV scale by applying the Jacobian. The lasing wavelengths are indicated in (k).

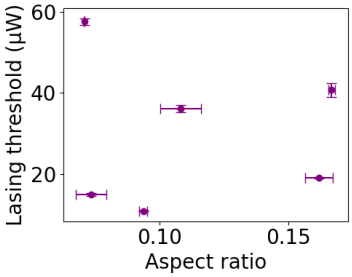

Figure 4.9: Lasing threshold as a function of aspect ratio (diameter/length) of each NW depicted in Figure 4.8.

4.3.3. TAILORING MODE STRUCTURE WITH THE ELECTRON BEAM

Finally, we investigated how prolonged electron beam exposure can alter the lasing behaviour of the GaN NWs. Electron beams are not only powerful tools for nanoscale imaging and material characterization (for example, through CL), but also offer a platform for in situ engineering of nanomaterials. The high energy electron beams used in electron microscopes can inadvertently generate defects and other undesirable artifacts in studied specimen. Such effects can sometimes be mitigated through the use of low beam currents, reduced acceleration voltage, pulsed electron beam operation, randomized scanning patterns, or cryogenic temperatures. However, several studies have demonstrated that the focused electron beam can instead be harnessed as a tool for controlled material modification. For example, electron irradiation can induce phase transformations in Sn nanowires[186], electron beam milling of metallic nanowires optimizes plasmon-phonon coupling[187], or can create color centers in hBN[188].

Building on this, we performed experiments to directly test whether sustained electron beam irradiation modifies the lasing characteristics of GaN NWs. Two representative NWs, imaged with SEs in Figure 4.10 (a-b), were first characterized under optical pumping by recording their emission spectra as a function of pump power. The spectra are plotted in Figures 4.10 (c-i) and (d-i) for the NWs depicted in (a) and (b) respectively. After these reference measurements, the centers of each nanowire were irradiated using a focused electron beam at 30 keV and a current of 65 nA for 5 minutes, before repeating the lasing measurements that are plotted in Figure 4.10 (c-ii) and (d-ii). This irradiation current is orders of magnitude higher than the standard currents used in CL experiments (typically tens to hundreds of pA).

We observe that following electron beam irradiation, the dominant lasing peak threshold and wavelength remains essentially unchanged. This indicates that the overall cavity quality and available optical gain are largely unaffected by the five-minute exposure. Follow up measurements (data not shown) have demonstrated that the CL spectrum are also unchanged. However, the multi-mode behaviour is clearly modified: the number of secondary lasing peaks, their relative intensities,

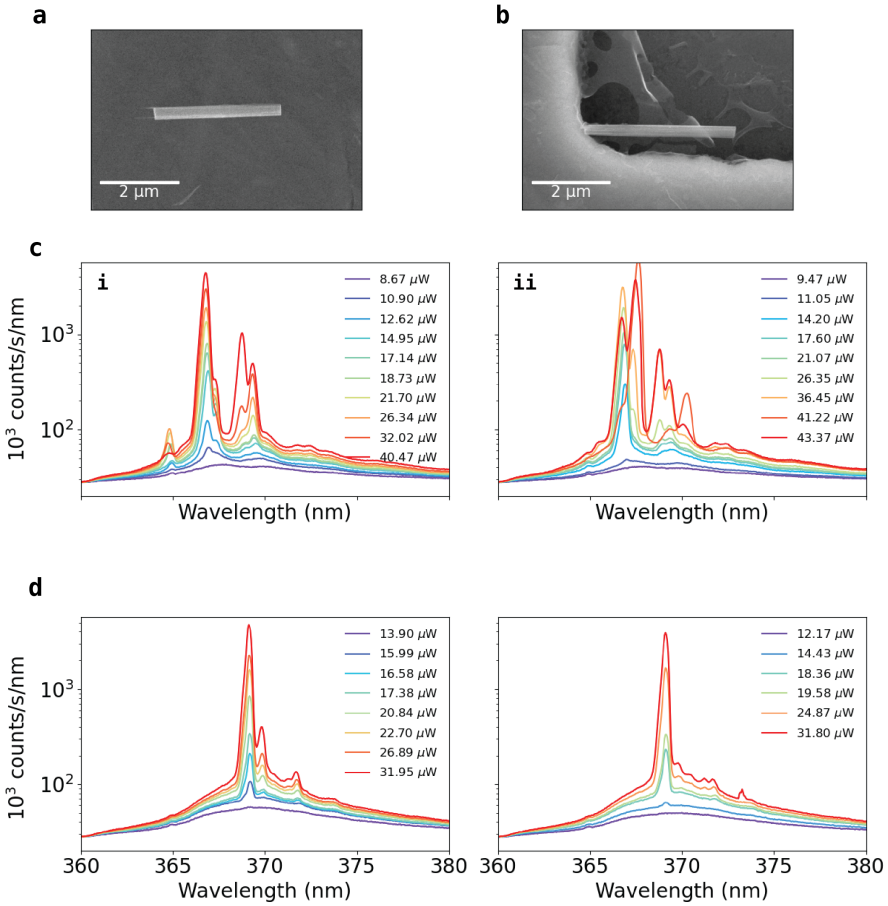

Figure 4.10: (a) and (b) SE images of shaved GaN NWs onto lacey carbon TEM grid that were irradiated with 65 nA of 30 keV electrons for 5 minutes at the centre of the nanowire. Columns (i) and (ii) show the lasing spectra before and after electron beam irradiation for (c) NL depicted in (a) and (d) NL depicted in (b).

and lasing wavelengths, are altered after electron beam exposure. This suggests that while the Fabry-Perot resonance condition is preserved, the electron beam perturbs the NW locally. This can occur through the creation of point defects in the irradiated region, increasing local losses that selectively modify certain cavity modes. Although these changes do not strongly impact the threshold of the dominant mode, they are sufficient to modify the higher-order modes, effectively acting as a means of mode selection. This raises an intriguing possibility of using electron-beam exposure as a tool for tailoring mode structure in nanowire lasers.

4.4. CONCLUSIONS

In conclusion, this study demonstrates how an integrated SEM-CL microscope, combining temperature resolved CL, TR-CL, SE imaging and PL can be used to probe the material and cavity gain properties of individual nanowires. CL and TR-CL experiments on GaN NWs revealed that non-radiative surface defects affect recombination dynamics, providing an important constraint on nanowire laser performance. Lasing measurements on NWs on a uniform Si substrate showed that the threshold reduction correlates strongly with increasing aspect ratio and primarily NW diameter which enhances the optical confinement, pump coupling, and reduces diffraction losses. In contrast, measurements of NWs deposited on lacey carbon TEM grids revealed no clear dependence of lasing threshold on geometry, demonstrating that local variations of environment introduce additional optical losses that outcompete the effects of the cavity geometry. Finally, lasing measurements before and after electron beam irradiation showed that introducing local defects with the electron beam did not alter the lasing properties of the dominant mode, but perturbs the modal distribution, opening the potential to use electron beams for mode selection.

While these results elucidate the effects of cavity gain, substrate, and electron beam irradiation on the far-field properties of NW lasers, they do not directly measure the underlying light-matter interactions at nanometer and femtosecond scales. The opportunity to access the near field of optically pumped nanolasers is provided by photon-induced near-field electron microscopy (PINEM)[189]. By coupling ultrafast electron pulses to the optical near field, PINEM would enable the spatiotemporal mapping of the lasing modes, allowing clear assignment of modes to spectral energies, and offering new insights into the impact of defects, exciton localization, and exciton-polariton coupling[190, 191]. Future PINEM studies will be continued by C. Santini and S. Meuret at CEMES.

5

PINEM IN THE SEM

Photon-induced near-field electron microscopy (PINEM) is a powerful technique for probing light-matter interactions at nanometer length and femtosecond time scales. Due to the lack of commercially available electron energy spectrometers for scanning electron microscopes (SEMs), PINEM has been almost exclusively implemented in ultrafast transmission electron microscopes (UTEMs). In this chapter, we demonstrate how PINEM can be implemented in a USEM using a retarding field analyzer (RFA) to measure the electron energy. This development makes PINEM more accessible, and offers advantages such as lower electron velocities to enhance near-field coupling strengths, and the flexibility of a larger vacuum chamber which enables the combination with advanced geometries for light incoupling and CL capabilities. We outline the implementation and realization of PINEM in the USEM, and validate the technique by performing near-field mapping of a silicon metasurface. We observe a broad distribution of coupling strengths, with electrons that gained up to 24 energy sidebands. Furthermore, we show how the combination of PINEM and energy measurements with the RFA can be used to characterize the energy spread and temporal profile of photoemitted electron pulses as a function of different electron gun parameters. By decreasing both the photon energy of the laser trigger and the extractor voltage, an electron energy resolution of $\Delta E = 0.3 \pm 0.03$ *eV can be achieved. Together these results demonstrate the feasibility of PINEM in the SEM and demonstrate it's potential as a tool for near-field mapping and ultrafast electron beam characterization.*

5.1. INTRODUCTION

In free-space, electrons and light do not interact due to their fundamental energy-momentum mismatch. This can be rectified by localizing the optical field using a resonant nanostructure. Confinement of the light into an evanescent mode, correspondingly delocalizes it in momentum space, producing a wide range of momenta. Some momentum components can match the given electrons momentum, thereby satisfying conservation laws and enabling electron-light coupling and the coherent exchange of energy. The quantum nature of this interaction manifests as electrons undergo quantized energy-gain and energy-loss interactions, spaced by the photon energy, $\hbar\omega$. The interaction strength is described by the dimensionless electron light-coupling factor, g, which is proportional to the amplitude of the longitudinal component of the electric field, E_z, along the electron propagation direction z, and given by the expression[192]

$$g(\mathbf{R}) = \frac{e}{2\hbar\omega}\int_{-\infty}^{\infty} E_z(\mathbf{R},z)e^{-i\frac{\omega}{v}z}\,dz, \tag{5.1}$$

where $\mathbf{R}$ is the transverse electron position, and v is the electron velocity. This exchange of energy is not stochastic, as if electrons were to randomly gain or lose photons the resulting distribution would simply average to the initial energy $|E_0>$. Instead, the process is coherent and can be understood as a quantum walk[193] in energy, where electron wavefunction evolves into a superposition of energy states $|E_0 \pm N\hbar\omega>$. The probability of populating the N^{th} sideband, P_N, can be derived by considering the action of the scattering operator on these states,

$$S = e^{ga^\dagger - g^* a}, \tag{5.2}$$

where $a^\dagger$ and $^*a$ are the photon absorption and loss operators respectively[85]. Solving the Hamiltonian evolution yields the result

$$P_N = J_N^2(2|g|), \tag{5.3}$$

where J_N is the Bessel function of the first kind. The same result can be derived semi-classically and using the time-dependent Schrödinger equation[194, 195].

With PINEM effectively being a form of pump-probe (PP) microscopy, where the optical near field is pumped by the laser and electron beam probes the excitation, the development of ultrafast transmission electron microscopes (UTEMs) provided the first experimental platform of exploiting the inelastic coupling of electrons and light for photon-induced near-field electron microscopy (PINEM)[84], which is now an established technique to probe the near-fields of material excitation on the nanometer length and femtosecond time scales[196–199]. Beyond near-field mapping, PINEM has opened exciting possibilities for reconstructing the quantum state of the electron wavefunction[90], wavefunction shaping[200], and attosecond electron pulse generation[91].

An underexplored platform for PINEM is the ultrafast scanning electron microscope (USEM), that gives access to slower electrons with energies of 500 eV to 30

keV. Compared to UTEM, such systems are relatively more affordable and commercially available. Importantly, reducing the electron velocity in equation 5.1 can lead to a large increase of the electron-light coupling strength[21, 201]. Additionally, the larger vacuum chamber size of the SEM offers more flexibility for integration of complex experimental geometries, such as implementing two or more subsequent PINEM interactions for wavefunction engineering. Finally, because electron microscopes are already established tools for cathodoluminescence (CL) microscopy, it gives the opportunity to perform correlative PINEM-CL experiments[202].

In this work, we demonstrate how PINEM can be integrated into our existing USEM-based PP-CL system using a retarding field analyzer as an electron energy spectrometer. We discuss the technical details of the set-up as well as the alignment procedures, and then demonstrate PINEM on a Si metasurface that was used as a dielectric laser accelerator (DLA) structure in earlier work in by Shiloh et al [203, 204]. Despite the limited energy resolution of the system, we are able to observe electron gain-sidebands and fit a coupling strength parameter of $g = 0.43 \pm 0.05$ eV. We use PINEM to map the near field of the DLA as a function of electron energy gain, to calculate the local coupling strength. Finally, we use the RFA and PINEM to study the electron energy resolution and electron pulse lengths as a function of different microscope parameters.

5.2. EXPERIMENTAL IMPLEMENTATION OF PINEM

5.2.1. RETARDING FIELD ANALYZER

The major challenge in the implementation of PINEM in an USEM is the lack of commercially available adapted electron energy spectrometers, and particularly ones with sufficient sensitivity and energy resolution. Such technology is widely available in (S)TEMs that operate with high energy electrons, and are routinely used for PINEM measurements and electron energy loss spectroscopy (EELS). These EELS spectrometers typically are high-resolution magnetic deflection analyzers, where depending on the energy of the electrons beam the Lorentz force applied by the magnetic field deflects the electron at a different angle. This dispersion is exploited to measure the electron beam energy with meV resolution[30]. The lack of development of EELS spectrometers in SEMs is precipitated by the fact that the slow electrons can only be transmitted through ultra-thin specimens, restricting the range of applications. Despite this, recent progress has been demonstrated using custom built SEM-EELS spectrometers with different approaches. One example is a home-built magnetic deflection spectrometer, based on half an Omega filter, used to study PINEM in the SEM at 10.4 keV[93]. Another employs cylindrical electrostatic deflection analyzer used to study EELS from 2D materials in the strong coupling regime[205]. Similar to magnetic analyzers, electrostatic deflectors rely on an angular dispersion of electron trajectories, due to an energy/velocity-dependent centripetal force, and are routinely used in low-energy electron microscopes (LEEM)[206]. It is noteworthy to mention that at low energy regimes $\ll 500$ eV, it becomes plausible to measure electron energy using changes of flight time, although

typically this method is used for ion energy measurements[206]. Finally, it is also worth noting that PINEM mapping of optical near-fields is possible without the use of an electron spectrometer, by measuring the electron deflection as a result of the Lorentz force of the near-field acting on slow electrons, and has been demonstrated in both SEM and LEEM [207, 208].

Our solution to measure the electron energy in the SEM uses a retarding field analyzer, based on the design described in ref. [209]. The operating principle behind such an energy analyzer is the use of a retarding electrode as a high pass filter of the electron energy. Scanning this electrode over a voltage range generates an energy-dependent transmission function of the electron beam. Our RFA device, shown in cross-section in Figure 5.1 a, consists of four electrodes at different potentials. Grounded electrodes are positioned at the entrance and exit, for electron beam deceleration upon entering the RFA, and re-acceleration upon exit. At the centre sits the 400 μm diameter scanning (retarding) electrode, U_{scanning}, which acts as the electron energy filter. It is biased at a threshold voltage, U_{th}, slightly below the primary energy of the electron beam. On top of this threshold voltage, an additional step-wise voltage is applied, ΔU, that increases the Couloumb barrier and incrementally repels lower-energy electrons. Above the retarding electrode is the focusing electrode, U_{focusing}, held at 98% of the threshold voltage. This electrode further decelerates the electron beam and focuses it into the retarding electrode. As there is a dispersion of the retarding potential across the scanning electrode (characterized in detail in ref. [210]), focusing the electrons beam into the centre of the electrode guarantees the optimum energy resolution.

It is important that, in contrast to the design in ref. [209], no additional focusing electrode was included beneath the scanning electrode. This choice was made because the MiniPix electron detector that is integrated with the RFA can suffer from pile-up effects in the regime of more than one electrons per pulse. As each pixel of the detector can register a single electron, and the dead time of the sensor exceeds electron pulse duration, the detection efficiency decreases at high currents[210]. To mitigate this, the electron beam is deliberately defocused onto the MiniPix sensor, diminishing pile-up.

In Figure 5.1 b, we show an example energy scan of the continuous electron beam (5 keV, spot 1.5, and 20 μm objective aperture) acquired with the RFA. The transmitted electrons are detected using a Timepix3 single-electron detector (Advacam MiniPix), and the count rate is recorded as a function of potential energy of the retarding electrode. For this measurement, the threshold voltage is set to $U_{\text{th}} \sim$ 4.997 kV and the scanning range is $\Delta U = 5.2$ V. The resulting transmission curve can be fit with the cumulative distribution function (CDF) of a pseudo-Voigt function, defined as

$$\begin{aligned} I(U;U_0,w) &= k\,L_{\text{CDF}}(U;U_0,w) + (1-k)\,G_{\text{CDF}}(U;U_0,w), \\ &= k\left[-\frac{I(0)}{\pi}\arctan\left(\frac{U-U_0}{w}\right)+\frac{I(0)}{2}\right] + (1-k)\frac{I(0)}{2}\left[1-\text{erf}\left(\sqrt{\ln(2)}\frac{U-U_0}{w}\right)\right], \end{aligned} \tag{5.4}$$

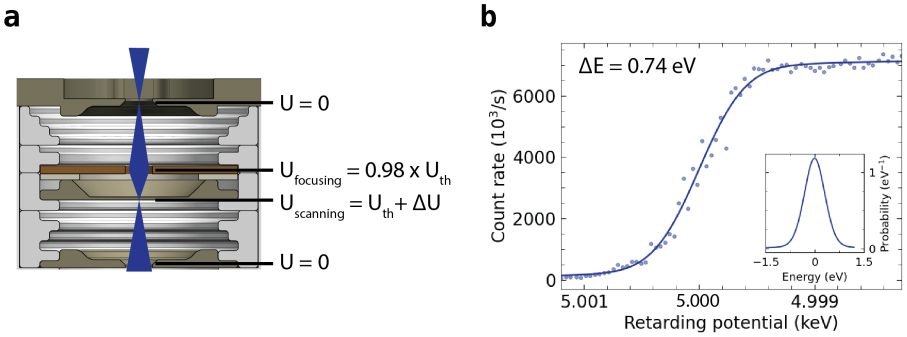

Figure 5.1: Electron energy measurements in the SEM with a RFA. (a) Schematic of the RFA cross-section with the focusing, scanning, entrance, and exit electrodes depicted. (b) Energy spread measurement of the 5 keV continuous electron beam. The retarding potential in the RFA is scanned around a voltage of 5 keV and the transmitted electron current is measured. The data is fitted with a CDF (Eq. 5.4). The inset figure plots the corresponding PDF (Eq. 5.6) of the fit.

5

where $L_{\mathrm{CDF}}(U;U_0,w)$ and $G_{\mathrm{CDF}}(U;U_0,w)$ are the Lorentzian and Gaussian CDFs respectively, U is the applied potential, U_0 the central electron energy, w the half-width half maximum (HWHM), and k controls the weight of the Gaussian and Lorentzian contributions. Since the CDF in Eq. 5.4 is the integral of the underlying probability density function (PDF), the corresponding PDF of the pseudo-Voigt distribution is

$$\begin{aligned} f(U;U_0,w) &= k\,L_{\mathrm{PDF}}(U;U_0,w) + (1-k)\,G_{\mathrm{PDF}}(U;U_0,w) \\ &= k\left[\frac{I(0)}{2\pi w}\frac{1}{1+\left(\frac{(U-U_0)}{w}\right)^2}\right] + (1-k)\frac{I(0)}{2w}\sqrt{\frac{\ln(2)}{\pi}}\exp\left[-\ln(2)\left(\frac{U-U_0}{w}\right)^2\right], \end{aligned} \tag{5.5}$$

where $L_{\mathrm{PDF}}(U;U_0,w)$ and $G_{\mathrm{PDF}}(U;U_0,w)$ are the Lorentzian and Gaussian PDFs respectively. This PDF represents the energy distribution of the electron beam, from which we can extract U_0, the primary electron energy, and the FWHM energy spread of the electron beam, $\Delta U = 2w$. This is analogous to the zero loss peak (ZLP) in EELS. The fit of the dataset in Figure 5.1b yields an energy spread of $\Delta U = 0.74 \pm 0.05$ eV, which is consistent with the typical energy spread anticipated from a Schottky field emission gun (FEG) source at 1800 K[54].

5.2.2. INTEGRATION INTO THE SEM

Although it is possible to mount the RFA onto a standard SEM stage [64, 210, 211], PINEM requires that a sample is properly aligned above the RFA, and furthermore requires optics in order to optically pump the sample. To accommodate for these

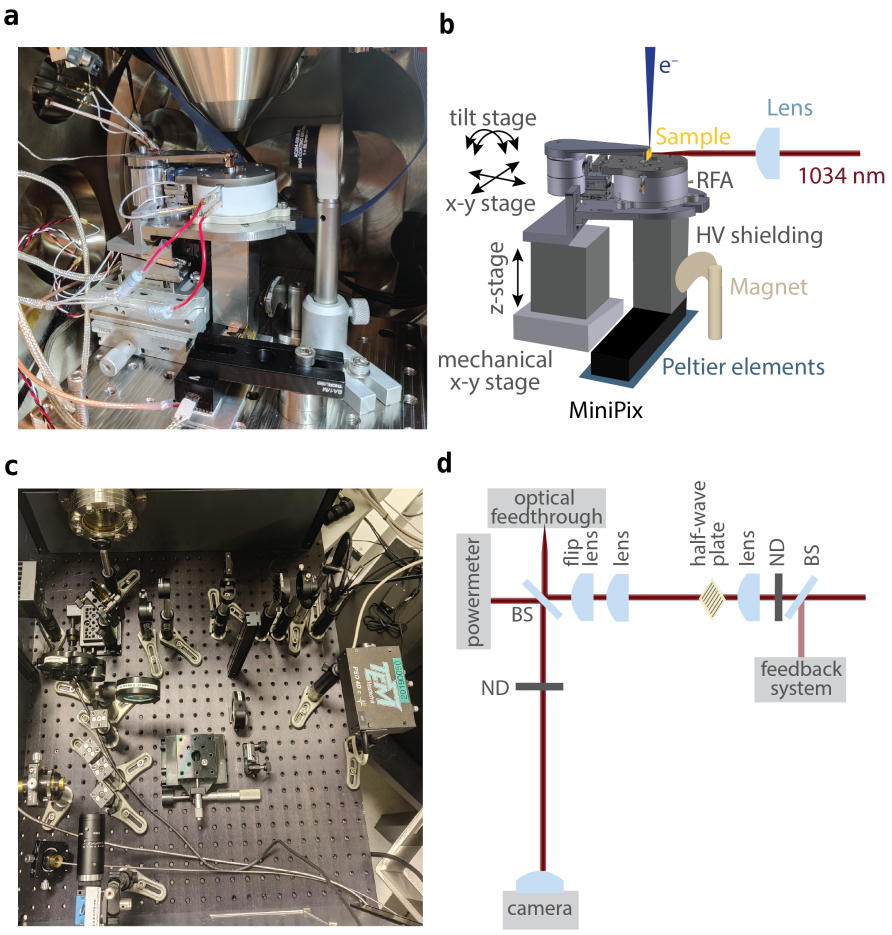

Figure 5.2: Depictions of the experimental PINEM set-up both inside and outside the SEM chamber. (a) Photographic and (b) schematic representation of the modified SEM chamber. The SEM stage is replaced with an optical breadboard and a custom door is installed. The RFA is mounted onto the breadboard with a home-built hexapod and automated stages for sample alignment into the laser focal point and positioning above the retarding electrode of the RFA. The MiniPix electron detector is cooled by Peltier elements coupled to the SEM stage and shielded with a hollow cage. A magnet is used to deflect the electron beam, preventing it from overlapping with pixels where scattered laser light also co-propagates. (c) Photographic and (d) schematic view of the optical set-up outside the SEM chamber. A telescope of two lenses matches the acceptance angle of the final focusing lens inside the SEM chamber. A flip-mounted lens allows switching between tight focusing for PINEM and defocused illumination, enabling both laser focus alignment and wide-area sample imaging with a camera.

requirements, and allow for maximum flexibility of the set-up for future experiments, the experimental pump-probe set up based on the USEM (ThermoFischer Quanta 250) described in Chapter 2, was redesigned. The original SEM door unit as well as the sample stage unit were removed and replaced with a custom door without a stage. An optical breadboard was mounted inside the SEM chamber, onto which the experimental set-up was installed. Building on the pump-probe set up (chapter 2, the same optical delay stage, harmonic generation and electron cathode excitation schemes were retained, while the laser was replaced with a system producing 300 fs pulses of $\lambda = 1034$ nm (Coherent Monaco 1035).

Figure 5.2 (a-b) demonstrates a schematic of the set-up within the SEM chamber. The RFA is mounted onto the breadboard atop of a mechanical x-y stage (Thorlabs DTS25V/M) and an automated z-stage (Thorlabs PDXZ1/M, with the PDXC2 piezo controller). The z-stage positions the RFA and sample relative to the focal point of the optical lens (focal length 50 mm) that focuses the pump laser onto the sample. To maintain alignment even at low current, pulsed conditions, the RFA is positioned beneath the pole piece using the mechanical x-y stage, such that the retarding electrode under high tension corresponds to a zero-deflection position of the electron beam at the pole piece exit. The sample is mounted onto a flange that is attached to a home-built hexapod stage, allowing independent movement relative to the RFA. This enables precise alignment of the sample with respect to the electron propagation axis, and positioning of the sample above the retarding electrode. The hexapod is composed of stages that move in x- and y- (Mechonics x-y mounted MS15) as well as along two tilt axes (Mechonics MT25), driven independently by piezo controllers (Mechonics, CF30). Beneath the RFA sits the MiniPix electron counter, cooled by three Peltier elements connected in series. The SEM stage serves as a heat sink of the Peltier cooling system, allowing stable operation of the MiniPix at 20°C for many hours. Surrounding the MiniPix sensor is a hollow shielding cage, that suppresses noise from stray, scattered high-voltage (HV) electrons.

Depending on the sample, scattered laser light can co-propagate with the electron beam and impact the same MiniPix pixels. Although the sensor threshold voltage is set above the photon energy, the high peak powers required for PINEM can still overshadow counts from the electron beam on the sensor. To avoid this, a disassembled hard-disk drive magnet is placed adjacent to the HV shielding to deflect the electron beam path. The magnet was oven-baked at ~ 500 K to deliberately reduce it's magnetic field strength. To enable the operation of all the electronics in the SEM, we integrated several electrical feedthroughs: a USB connection for the MiniPix, feedthroughs for three RS232 ports for control of the positioning stages, and a HV feedthrough for the RFA. For operation up to 5 kV, the electrodes are powered by a high resolution power supply (FuG Elektronik GmbH, HCN-35-6500), and for higher voltages up to 13 kV, a different power supply is used (FuG Elektronik GmbH, HCL-35-12500).

To focus the pump laser onto the sample with lenses rather than the parabolic mirror, the optical set-up outside of the SEM was updated with respect to the pump-

probe configuration, as depicted in Figure 5.2 (c-d). To match the acceptance angle of the 50 mm lens within the SEM chamber, a telescope was built using a pair of 75 mm and 125 mm focal point lenses to adjust the beam diameter before it is coupled into the chamber using a beam splitter. The laser focus on the sample can be imaged through an imaging lens with a CMOS camera (the Imaging Source, DMK 33UX183). Additionally, a 400 mm lens mounted on a flip mount provides the option of insertion into the beam path to create a defocused spot. In this configuration, the defocused beam enables the illumination of a larger area of the sample and optical imaging of the sample with the camera. Finally, a half-wave plate is also installed into the beam path to adjust the laser polarization for more efficient coupling to the nanostructured samples described in the next section.

5.2.3. DIELECTRIC LASER ACCELERATOR STRUCTURE

To simplify the alignment of the electron-laser spatial and temporal overlap, it is important to boost the coupling strength between the electrons and the optical near-field, using many subsequent interactions over an extended interaction length. This can be achieved using a phase-matched metasurface, such as an optical grating. Phase matching ensures that the electron velocity is synchronized with the phase velocity of the optical mode co-propagating with the electron along the metasurface, enabling energy transfer over multiple optical cycles. One way to achieve this is with a dielectric laser accelerator (DLA), originally designed for compact electron acceleration[212]. The DLA operates using periodic dielectrics features (i.e. gratings or metasurfaces) that support optical near fields. When illuminated with a laser, the periodic structure generates evanescent fields with a phase velocity that can be engineered to match the electron velocity by adjusting the periodicity of the grating. Under these conditions, the swift electron grazing the structure is accelerated by each successive optical cycle, leading to efficient energy exchange. This is effectively the same principle behind conventional linear radio-frequency particle accelerators, however dielectric materials exhibit a much higher breakdown threshold than metals. As a result, DLAs can achieve extremely high acceleration gradients on the order of GeV/m [213]. This can also be viewed as the inverse Smith-Purcell effect, but with the energy transfer direction reversed. Employing a DLA structure as the PINEM sample thus ensures strong coupling to the electron beam and increases the probability of observing an electron energy modulation and finding a precise laser-electron overlap.

Our DLA structures were designed and fabricated in the Hommelhoff group based at the Friedrich Alexander University of Erlangen-Nürnberg, as described in ref. [203, 204], and are depicted in the SEM image in Figure 5.3b. The samples are composed of two symmetric columns of Si nanocylinders separated by a 225 nm channel, with target diameters of 400 nm, a periodicity of 600 nm over 40 periods, and nanocylinder heights of 2.7 μm. The dual-nanocylinder channel is surrounded by ten distributed Bragg reflectors on either side of the structure. The purpose of the Bragg mirrors is to increase the efficiency of out-of-plane illumination of the structures (as in our geometry), which has been shown in ref. [203]. However, as

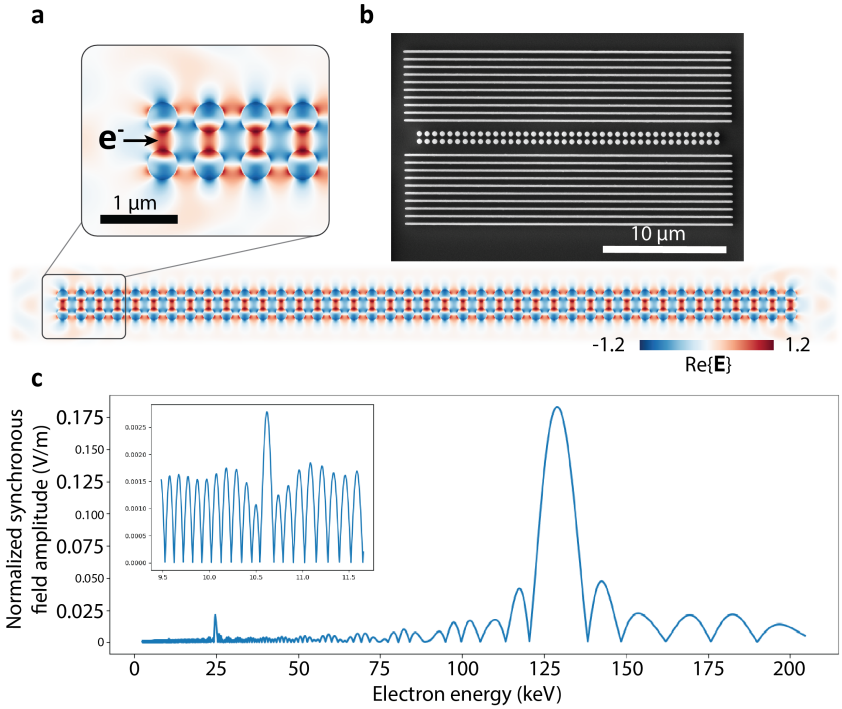

Figure 5.3: Lumerical FDTD simulation of DLA structure. (a) Real component of simulated electric field, normalized to the amplitude of the plane wave excitation, with an additional zoomed in panel showing the nanocylinder geometry and the electron injection axis. (b) SEM image of the fabricated DLA, consisting of two parallel rows of Si nanocylinders separated by a 225 nm channel and surrounded by Bragg reflectors. (c) Calculated normalized synchronous field amplitude at the centre of the nanocylinder channel as a function of electron beam energy. Inset: zoomed in view of the coupling to the third spatial mode at 10.6 keV, corresponding to the operating energy used in this work.

these reflectors were designed for 1.93 μm wavelength illumination, within our set up the Bragg reflectors play no role. The samples were fabricated using electron beam lithography from 1 - 5 Ω·cm doped, <100> silicon substrates. The patterns were printed onto a 400-nm-thick negative resist (ma-N 2405) using a 100 keV electron beam writer (Raith EBPG 5200). Following resist development, the sample was etched using cryogenic reactive ion etching (Oxford Instruments Plasmalab100) to the target height of the sample, followed by resist removal using acid piranha solution.

A Lumerical 2D FDTD simulation of the DLA structure in frequency domain is depicted in Figure 5.3. Due to the 2D nature of the simulation, the simulation was driven by two counter propagating plane waves from opposite sides of the structure, incident from above and below the nanocylinders, each at a frequency of ω = 290.5 THz (corresponding to λ = 1034 nm). For simplicity, the Bragg mirrors were omitted, however, it has been shown that out-of-plane illumination will result in about a 35% reduction of the resulting acceleration gradient created by the structure[203]. The phase of the simulation output was rotated such that the electric field at the centre of the structure was completely real, to maximize the electric field and ensuring that no electric field amplitude was *hidden* in the complex component. The input plane waves were then subtracted from the results, possible because they are not phase-matched with the electrons and do not meaningfully interact, and the resulting real component of the electric near field is plotted in Figure 5.3a. To quantify the coupling between the electrons and the simulated near field, a crosscut of the complex electric field along the centre of the nanocylinder channel was extracted and evaluated for electrons of different energies. The energy-dependent electron velocity determines the parallel wave vector $k_{||} = \frac{2\pi}{\beta\lambda}$ where β is the electron velocity relative to the speed of light, $\beta = v/c$, $0 < \beta < 1$. For each electron velocity, the E_x field was multiplied by the phase factor $\exp^{-ik_{||}x}$, representing the phase accumulated by an electron traveling along the x direction through the channel. The integral of this product along the electron trajectory, equivalent to taking the Fourier component of the field with the parallel wave vector, yields the amplitude of the mode that phase matched with the electron. The resulting amplitude as a function of electron energy is plotted in Figure 5.3c.

As the sample was designed for illumination with a 1.93 μm laser, adjusted for the fundamental output of our laser at 1034 nm, the amplitude peaks at ~ 129, 24.7, and 10.6 keV, corresponding to the first, second, and third order spatial modes respectively. Because the current design of our RFA is limited to 13 kV, the work in the following sections all operated at an electron beam energy of 10.6 keV, coupling to the third spatial harmonic of the DLA. This result illustrates that designing a structure specifically for our experimental electron energies and laser wavelengths would enhance the coupling by several orders of magnitude.

An important experimental consideration is the grazing length of the electron beam. Because of the high convergence angle of the electron beam in the SEM, combined with the transverse broadening of the electron beam that occurs after the PINEM interaction[214], a grating that is too long or positioned too close to the

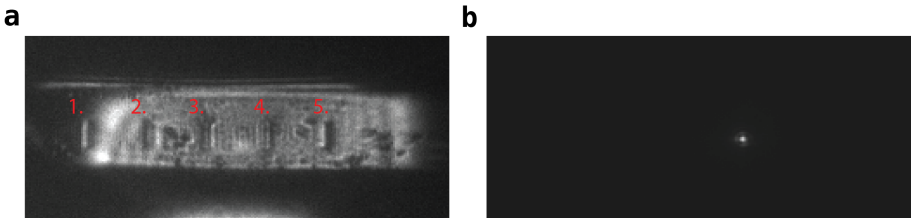

Figure 5.4: (a) Camera image of the sample with the defocusing lens inserted, showing a wide field of view and five labeled 80 μm long DLA structures illuminated. (b) Camera image of the tightly focused laser spot with defocusing lens removed.

substrate surface, will cause many of the interacted electron to be deflected into the substrate instead of transmitted. To avoid this, it is essential to fabricate either deep grating elements, or fabricating gratings on raised mesa structures. In our case, the DLA length was limited to 24 μm and the nanocylinders had heights of 2.7 μm.

5.2.4. SPATIOTEMPORAL ALIGNMENT

To align the laser spot on the sample, we iteratively flip the defocusing lens in and out of the optical path. When inserted (Figure 5.4 a), the beam is expanded to illuminate a large field of view, which allows for clear imaging of the sample surface and identification of multiple DLA structures. Removing the defocusing lens (Figure 5.4 b), focuses the laser tightly on the sample. This procedure enables accurate alignment of the focused spot directly over a target DLA structure. The laser spot size was estimated by first calibrating the pixel-to-micrometer conversion from Figure 5.4a, using the known dimensions of the DLA structure. The intensity profile across the laser spot in Figure 5.4 b was then fitted with a Gaussian to approximate the FWHM intensity distribution. The resulting value, converted using the pixel calibration, corresponds to a spot diameter of approximately 15 μm.

The electron-laser temporal overlap was coarsely aligned within a ~100 ps window, using an uncapped fast photodiode with a 35 ps rise time (Thorlabs FDS015) that was mounted onto the sample flange at an angle, and electrically connected to an oscilloscope via a BNC feedthrough. The oscilloscope was triggered by the RF output of the laser, and signals generated separately by incident laser pulses and by incident 10.6 keV electron pulses were recorded. The electron pulses were generated by triggering the cathode with the third harmonic (TH) of the laser. As described in Chapter 1, by adjusting the first condensor lens (C1) the beam current was boosted such that illumination with ~2 nJ of the TH at a high extractor voltage (4155 V) produced on the order of 1 electron per pulse compared to the sub 0.1 electron/pulse regime used for high-resolution imaging. Although this reduced the spatial resolution of the beam, the signal-to-noise ratio was greatly improved, which facilitated the identification of the electron pulse on the photodiode. By comparing the relative arrival times of the electron and laser signals on the oscilloscope, the optical delay stage could be adjusted to achieve a coarse temporal overlap. It is important to note that changing the C1 voltage changes the arrival

time of the electron beam on the sample.

It is advantageous to perform this overlap search at the highest available electron energy. Although in some cases slower electrons in the SEM exhibit higher coupling strength, they couple more efficiently to higher spatial-frequency components of the evanescent near-fields, which decay with distance proportionally to $e^{-ik_x x}$. Considering an electron beam traveling along z and an infinite grating along y, the decay constant of such a field can be written as $\Gamma = ik_x$. Using the wave equation, and noting that in this scenario k_y is zero, and k_z corresponds to the momentum of the co-propagating mode ($k_z = \frac{\omega}{v}$), the decay constant can be expressed in terms of electron velocity. By rewriting the velocity as a fraction of the speed of light, β, and including relativistic corrections via the Lorentz factor, $\gamma = \frac{1}{\sqrt{1-\beta^2}}$, the relation becomes[215]

$$\Gamma = \frac{\omega}{\beta\gamma c}. \tag{5.6}$$

This expression shows that as the electron velocity decreases, the interaction is dominated by increasingly strongly confined near-field components with shorter decay lengths. In the case of a structure confined in both transverse directions, $k_y \neq 0$, and the decay length further shortens. Consequently, PINEM measurements at low electron energies become highly sensitive to the electron beam position and to drift. Using higher-energy electron for alignment minimizes the spatial uncertainty to optimize in time.

After establishing the spatial alignment of the laser on the DLA sample, the temporal overlap was achieved. For this measurement, the electron beam was positioned within the nanocylinder channel, as shown in the SEM image of a side view of the channel in Figure 5.5 a (note that this image was recorded with a continuous electron beam). At the higher current but poor spatial resolution settings described above, the beam position within the channel was less sensitive to spatial drift, which made the overlap search more robust. The position of the optical delay stage was then scanned over 100 ps window around the coarse alignment position determined with the photodiode/oscilloscope method. During the delay scan, the threshold voltage of the RFA was set several volts above the ZLP of the electron beam, ensuring that mostly energy-gain electrons were transmitted. The electron count rate on the MiniPix was recorded as a function of delay. The onset of a pronounced increase in counts revealed the formation of PINEM gain sidebands, and that the electron and laser pulses were overlapped spatiotemporally.

5.2.5. PINEM MEASUREMENTS

After confirming the temporal overlap through PINEM, the electron beam settings were returned to the standard C1 voltage and operated in the low-current regime to maximize the spatial resolution. Spatially resolved PINEM measurements were then performed to map the near-field distribution on the nanocylinders. The electron beam was raster scanned across the same sample depicted in Figure 5.5 a, while keeping the RFA fixed at a threshold voltage corresponding to energy-gain

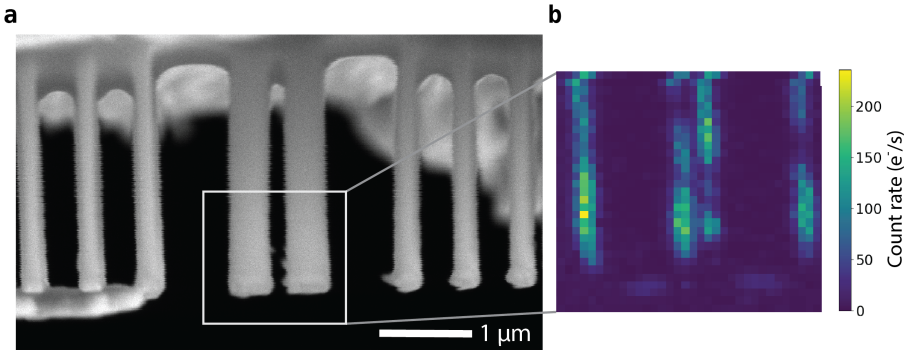

Figure 5.5: (a) SEM image of the side profile of a 25 μm long DLA structure. The two central features correspond to the side profile of the nanocylinders, surrounded by the Bragg reflectors on either side. (b) Spatially resolved PINEM map showing the count rate of gain electrons recorded while raster scanning the electron beam along the DLA. The resulting map reflects the local optical near field distribution.

electrons. At each beam position, the transmitted count rate was recorded, yielding a two-dimensional map of the gain electron signal, as plotted in Figure 5.5 b. Since the gain probability is directly related to the strength of the optical near field, such maps provide the basis for reconstructing the electric fields. The resulting map reveals that the near-field is excited along the length of the nanocylinder as well as across it's front facet.

Unlike PINEM mapping performed with an EELS spectrometer in UTEMs, where both the spatial map and the corresponding energy spectrum can be acquired simultaneously, using the RFA the threshold voltage must be scanned for each pixel position in the map in order to reconstruct the energy spectrum. Figure 5.6 shows the energy spectrum obtained by parking the electron beam at the centre of the DLA channel and recording the electron count rate on the MiniPix detector as a function of retarding potential of the RFA. This was performed when laser excitation of the sample was temporally unsynchronized (blue curve) with the electron pulse, meaning that they did not overlap at the sample, corresponding to the ZLP of the electron beam, and laser synchronization (red curve), producing the PINEM spectrum characterized by sidebands from having gained and lost quanta of energy.

The ZLP (blue curve) of the electron beam can be fitted with eq. 5.4, resulting in an energy spread of 1.1 ± 0.08 eV. The influence of the electron beam settings on the energy spread will be discussed in section 5.3, but we note here that the energy resolution of our PINEM measurements are limited by the high-voltage power supply required for 10.6 keV operation, that has a voltage ripple of ~0.58 eV. Together, the energy resolution is not sufficient to resolve individual PINEM sidebands, however, the PINEM spectrum (red curve) does show a clear modulation of the electron transmission spectrum, evidence of strong electron-photon coupling.

To analyze this spectrum, the transmission curve was fitted with a modified CDF composed of a sum of 2N+1 pseudo-Voigt functions, each separated by the

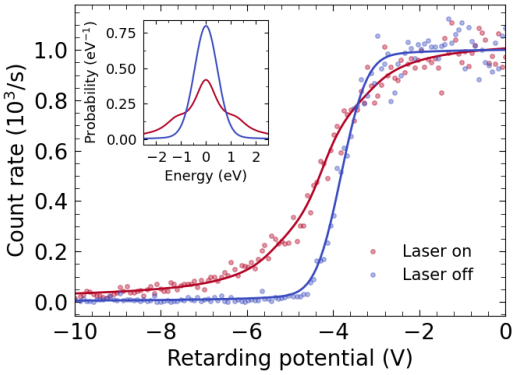

Figure 5.6: Transmission spectrum of the 10.6 keV electron beam positioned at the center of the nanocylinder channel, recorded with (blue curve) and with (red curve) synchronized 1.1991 eV laser excitation of the sample (pulse energy ≈ 70 nJ). The RFA transmission curves are fitted with CDF distribution functions, from which the corresponding PDFs representing the energy spectra are extracted and plotted in the inset.

photon energy of the laser (1.1991 eV) and constrained to share the same energy spread as the ZLP. The relative intensities of the sidebands were determined according to eq. 5.3, which gives the probability of populating the N^{th} sideband as a function of the coupling factor, g, through Bessel functions. The corresponding PDF of the fit reconstructs the PINEM sidebands, that are barely resolved given our energy resolution, and fits the coupling strength, $g = 0.43 \pm 0.05$ eV. It should be noted, however, that the extracted g does not correspond to a single, well-defined value for all electrons in the measurements. The measured energy spread indicates that the initial electron distribution is impacted by incoherent fluctuations, and in addition the PINEM spectrum represents an average over both space and time. As a result, g would be more accurately represented by a distribution with uncertainty Δg rather that a single parameter[21, 216], as from the total number of electrons grazing the sample, some will not interact at all, while others will gain many quanta of energy.

This becomes apparent when examining PINEM maps recorded as a function of RFA voltage, as depicted in Figure 5.7. For these experiments, a different DLA structure was employed, as shown in the secondary electron (SE) image of Figure 5.7 a. The corresponding electron energy spectrum, recorded with the electron beam parked in the center of the nanocylinder channel and synchronized with the laser is plotted in Figure 5.7 b. Here the ZLP exhibited an energy spread of 3.7 ± 0.11 eV and the fitted coupling strength is $g = 0.68 \pm 0.43$ eV. Such a coupling value would only be expected to significantly populate the first energy sidebands. However, as the RFA voltage, ΔU, is progressively increased from 1 V to 34 V above the threshold voltage, U_{th}, a small but distinct fraction of electrons focused through the DLA channel experience gain. Since a retarding potential of ~5 V corresponds to the ZLP of the electron beam, electrons detected at $\Delta U = 34$ V must have gained ~29

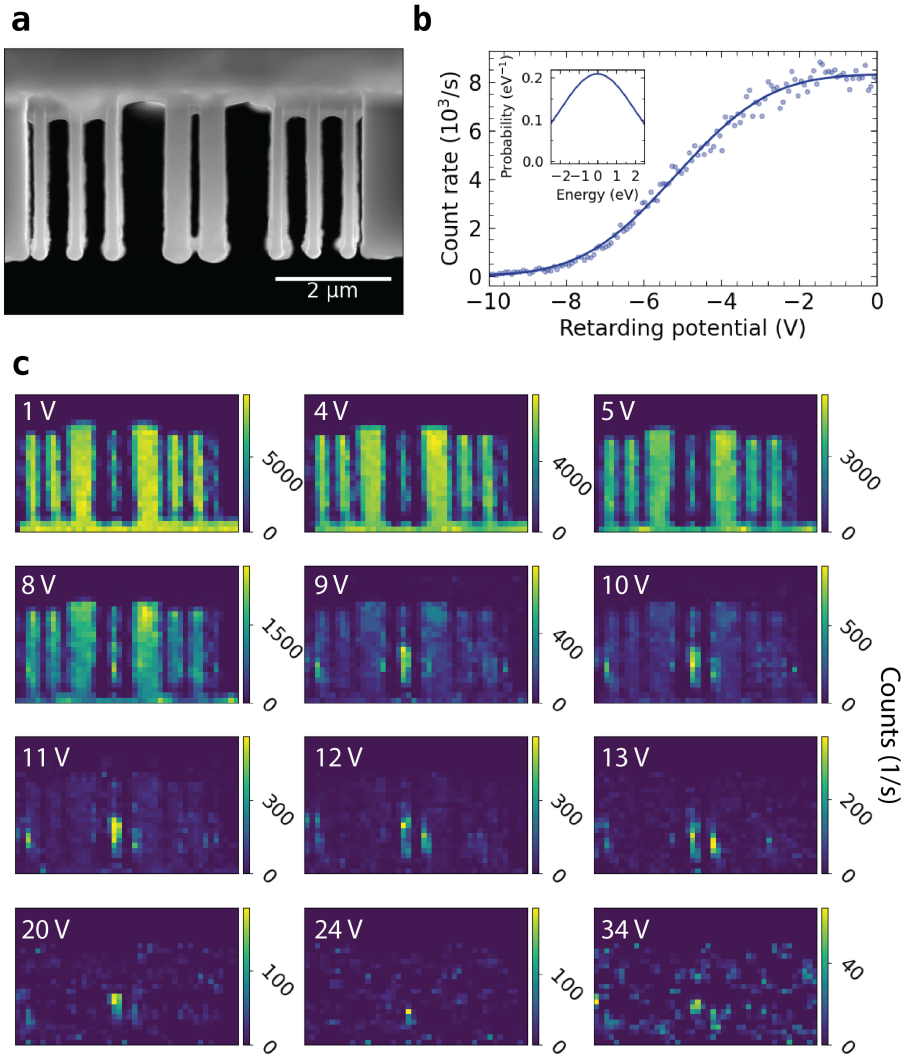

Figure 5.7: (a) SE image of the DLA structure. The electron beam was positioned in the center of the nanocylinder channel to measure the corresponding (b) electron energy spectrum under laser synchronization. The ZLP has an energy spread of 3.7 ± 0.11 eV, and the curve is fit with the modified CDF including Pseudo-Voigt sidebands, resulting in a fitted coupling strength of $g = 0.68 \pm 0.43$. The corresponding PDF representing the energy spectrum in plotted in the inset. (c) PINEM maps acquired as a function of additional voltage applied to the RFA, $\Delta U = 1 - 34$ V.

eV, approximately corresponding to the 24^{th} sideband for a photon energy of 1.1991 eV. Although the relative population of this sideband is only about 1% of the total electrons, its presence indicates that a subset of electron have experienced a local coupling strength of the order of g ~ 11.4, at the minimum. This highlights that the interaction involves a wide range of coupling strengths, that cannot be captured by a single effective g, primarily because of the mismatch in electron and laser pulse lengths.

5.3. ELECTRON PULSE CHARACTERIZATION

Having established the advantages of performing PINEM experiments in the SEM, it's implementation, and demonstrated it's capability of mapping optical near fields, we now turn to using the RFA in combination with PINEM to characterize the energy spread and temporal profiles of electron pulses generated by photoemission in the USEM. Accessing a narrow energy spread is essential to achieving the high energy resolution required for PINEM and EELS measurements. Equally important, controlling the initial electron pulse length is a requirement for wavepacket shaping and attosecond pulse generation. Pulse lengths on the order of tens of picoseconds can be characterized using time-resolved cathodoluminescence measurements (TR-CL) using time-correlated single-photon counting [53], or streak cameras[217]. In contrast, shorter pulses achievable via photoemission are more challenging to characterize directly and PINEM offers one of the few methods to measure them. While the characterization of energy, pulse length, and spatial coherence of photoemitted electron pulses in UTEMs has been reported in several studies[218–222], such measurements in USEM are limited[64], with earlier work focused on spatial resolution[53], and only more recent studies addressing pulse durations[60]. Importantly, the focus of these publications is not on the intrinsic photoemission mechanisms dictated by the cathode source, which in our case is a Schottky field-emission-gun (FEG) with a ZrO/W tip. While factors such as the emitting facet, tip size, and material are all critical and differ slightly between thermionic, Schottky, and cold FEG regimes, our focus is on the usable, apertured electron beam at the sample plane, and it's dependence on SEM gun parameters.

5.3.1. ENERGY SPREAD MEASUREMENTS

Firstly, Figure 5.8 compares the transmission spectra of continuous, thermally emitted electrons (blue curve), and electrons generated via photoemission (red curve). For this measurement, the filament current was decreased from 2.41 A to 1.2 A and its was left to cool for around 50 min, effectively decreasing the current. The extractor voltage was kept at its standard high value of 4155 V. The tip was then laser triggered using the fourth harmonic (FH, λ = 257 nm) at a low pulse energy of 100 nJ. These conditions enabled the simultaneous observation of the two emission channels, resulting in two separate peaks in the photoemission spectrum (red curve). Fitting the transmission spectra with a standard CDF for the thermal spectrum, and the CDF of a sum of two Pseudo-Voigt functions for the photoemission spectrum,

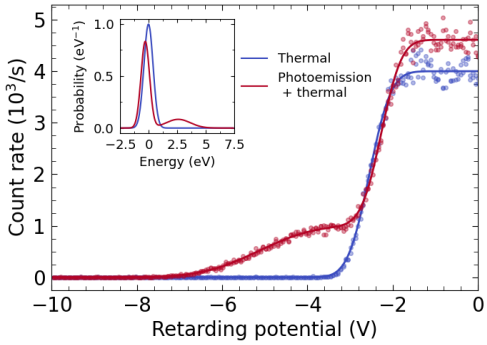

Figure 5.8: Transmission spectra of the thermally emitted electrons (blue curve) and the combined thermal and photoemitted electrons at 10.6 keV accelerating voltage from the Schottky ZrO/W FEG. The spectra were fitted with a CDF corresponding to a single or sum of two Pseudo-Voigt function for the thermal electrons and combination of thermal and photoemission electrons respectively, and with the corresponding PDFs of the fits plotted in the inset.

allowed for the extraction of the corresponding PDFs (plotted in the inset). The energy difference between the two peaks was determined as $\Delta E = 2.88 \pm 0.07$ eV. This difference corresponds to the excess energy of the photoemitted electrons relative to the thermally emitted population. By subtracting this value from the photon energy of the laser trigger (4.82 eV), the effective work function of the tip can be estimated as $\Phi_{\text{eff}} = 1.94$ eV. A ZrO/W cathode typically has a work function in the range of $\Phi \sim 2.8-2.9$ eV [223] with some temperature dependence, which suggests that an external electric field generated by the extractor voltage must lower the barrier by approximately 0.645 V/nm to reduce to effective work function from 2.9 eV to 1.94 eV. We note that additional factors may also contribute to the reduction of the work function, for instance, energy losses due to surface adsorbates on the tip[224, 225].

Next, the effect of laser triggering on the energy spread of the electron pulses was measured, together with the influence of varying the extractor voltage. Figure 5.9 a, shows the energy spread of the photoemitted electron pulses as a function of laser pulse energy on the electron cathode. For these measurements, the FH was used, with the laser polarization aligned with the axis of the cathode using a half-wave plate to maximize the emission efficiency. The SEM was operated with a cold tip, achieved by reducing the filament current from 2.41 A to 1.2 A, and a 50 μm aperture. Four extractor voltage settings were investigated, matching the conditions previously used for electron current measurements as a function of laser pulse energy (Chapter 1, Figure 1.3 b). At the standard, high extractor voltage of 4155 V, two condenser lens (C1) voltages were compared. First, the standard C1, 1305 V, configuration yielding a modest current and a high spatial resolution, and secondly an optimized C1 voltage, 1100 V, maximizing the current. The later results in an increased energy width as fewer electrons are cropped by the aperture. This comparison is important, as for all other extractor voltages, the C1 setting was always optimized for current. Measurements were also performed at an intermediate

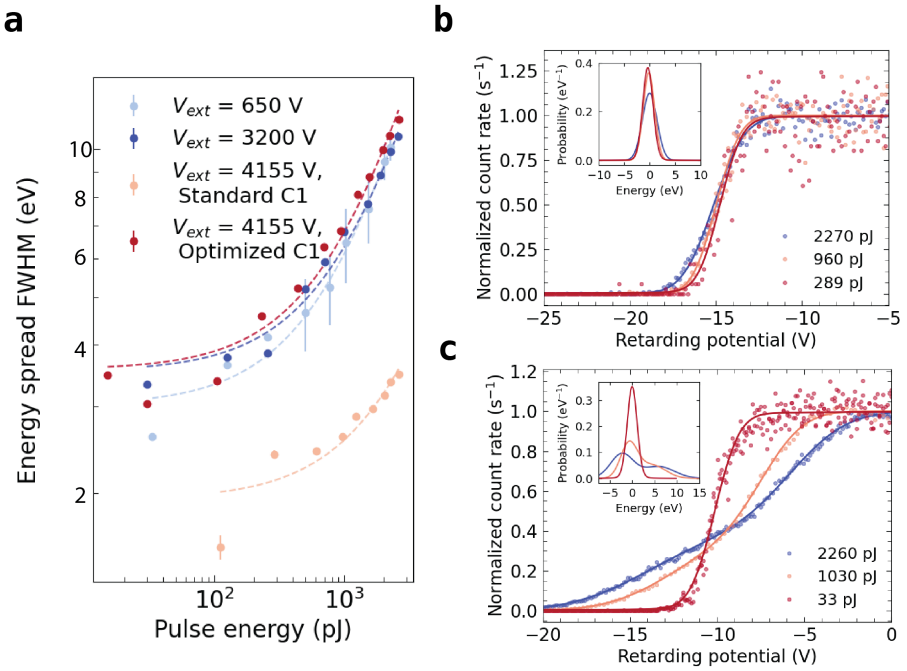

Figure 5.9: (a) Energy spread of photoemitted electron pulses at 10.6 keV as a function of laser pulse energy, extracted from transmission spectra of the electron beam through the RFA. The SEM was operated with a 50 μm aperture and four extractor voltage settings, 4155 V standard C1 (orange curve), 4155 V optimized C1 (red curve), 3200 V (pale blue curve) and 650 V (dark blue curve). (b, c) Transmission spectra recorded with the RFA at 4155 V standard C1, and 650 V respectively for low, intermediate and high laser pulse energy. Insets shows the corresponding energy spectra (PDFs) derived from CDF fits.

extractor voltage of 3200 V, corresponding to the setting at which the thermal emission of electrons is completely quenched, and at a low extractor voltage of 650 V, where strong focusing effects increase collection of electrons through the extractor aperture leading to very high currents at the sample plane[65]. Despite this increase in current, the energy spread as a function of laser pulse energy remains comparable to that obtained at 3200 V and 4155 V (optimized C1). In all four cases, the energy spread increases linearly with pulse energy. This behavior, observed previously in TEM studies[219, 221, 222], is attributed to the Boersch effect as a result of Coulomb interactions between the electrons in the pulse, that becomes more significant as the number of electron per pulse increases.

Figure 5.9 b & c, show example transmission spectra from the data set measured with the RFA at extractor voltages of 4155 V (standard C1) and 650 V, respectively. For each setting, the spectra are displayed at three laser pulse energies (in the range of 30 pJ/pulse to 2 nJ/pulse). The data are fitted with CDF functions, while the derivative of these fits, representing the PDF, are plotted in the insets. In both cases, a clear broadening of the energy distribution is observed with increasing laser pulse energy. However, at 650 V the energy distribution not only broadens, but also splits into two distinct peaks. This splitting is a result of pronounced space-charge effects, where the high electron density leads to the separation of the pulse into two bunches of accelerated and decelerated electrons[106, 222, 226]. For most measurements, the energy width is reported as the full width at half maximum (FWHM) of the PDF. However, at high laser pulse energies where the splitting becomes evident, the CDF is best described by a sum of two Pseudo-Voigt functions. In such cases the effective energy width is calculated using the weighted FWHM of the two peaks,

$$\Delta E = 2.355\,\sigma_{tot} = 2.355\,\sqrt{w_1\sigma_1^2 + w_2\sigma_2^2 + w_1 w_2 (E_1 - E_2)^2}, \tag{5.7}$$

where E_1, E_2 are the central energies of the two peaks, σ_1, σ_2 are their standard deviations, and w_1, w_2 the relative weighted amplitudes.

The measurements at 10.6 keV electron energy provide important insight into the range of experimental settings usable for PINEM experiments with the available DLA sample. However, the limited energy resolution of the high-voltage power supply constrains the precision with which the lower limit of the intrinsic electron pulse width can be determined. Energy spread measurements at a lower electron acceleration voltage of 5 keV that use a higher resolution power supply for the RFA, can overcome this limitation. In this configuration, a Faraday cup beneath the RFA was used to count the electrons instead of the MiniPix, and a 1 mm aperture was used to maximize electron collection.

In these measurements, plotted in Figure 5.10, both fourth harmonic (FH, λ = 257 nm) and third harmonic (TH, λ = 345 nm) excitation was used, to compare the effect of photon energy on the energy spread. No waveplate was employed to adjust the polarization of the excitation laser. Two extractor voltage settings were investigated, a low extractor voltage of 650 V, and a standard setting 4550 V with optimized C1. The high value of the standard extractor voltage, compared to 4155 V used in the

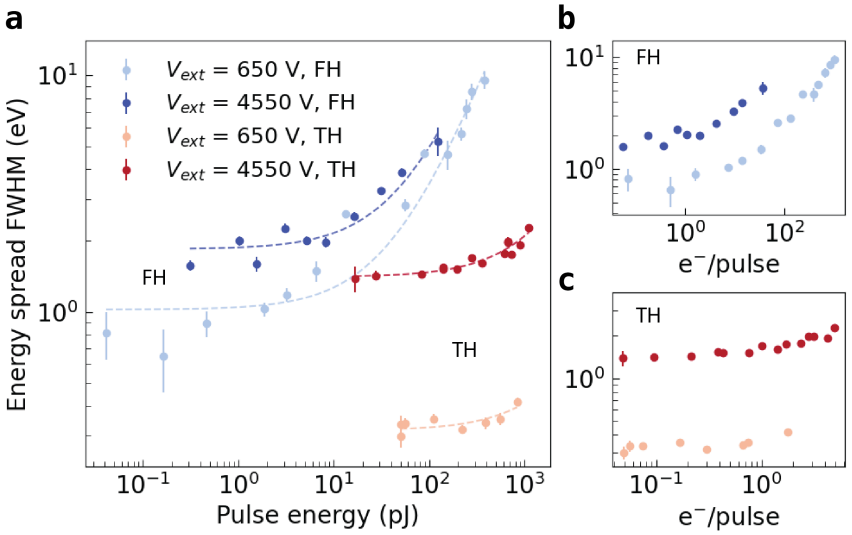

Figure 5.10: (a) Energy spread of photoemitted electron pulses at 5 keV as a function of laser pulse energy, extracted from transmission spectra of the electron beam through the RFA using a Faraday cup detector and a 1 mm aperture. Both FH and TH excitation were used and measurements were performed at two extractor voltage settings, 4155 V optimized C1, and 650 V. (b,c) The same data plotted as a function of number of electrons per pulse for FH and TH excitation respectively.

10.6 measurements, is due to the fact that these experiments were performed on a different electron cathode. Figure 5.10 a plots the measured FWHM of the energy spread as a function of laser pulse energy focused to the tip. Figure 5.10 b & c show the same data, but plotted as a function of the number of electrons per pulse for FH and TH excitation respectively. In all cases, the energy spread increases linearly with pulse energy, consistent with the Boersch effect. With the increased energy resolution of this set up, it is evident that TH excitation systematically produces a narrower energy spread than FH excitation. This is a consequence of lower excitation efficiency of the TH photons, as their energy lies closer to the work function of the cathode, lowering the excess energy of the electrons that are excited over the barrier[227].

Notably, these measurements reveal the narrowest energy width of the electron beam obtained in this study, $\Delta E = 0.3 \pm 0.03$ eV, under TH excitation and an extractor voltage of 650 V. A systematic decrease in energy spread is observed when reducing the extractor voltage from 4550 V to 650 V. For TH excitation the minimum energy width decreases from 1.38 ± 0.17 eV at 4550 V to 0.3 ± 0.03 eV at 650 V. A similar trend is observed for FH excitation, where the minimum width is reduced from 1.57 ± 0.08 eV to 0.65 ± 0.19 eV. This reduction is attributed to the increase in the effective work function of the tip at lower extractor fields. An increased energy barrier reduces the excess energy of the electrons resulting in a narrower energy spread.

These results demonstrate that by controlling both the trigger laser wavelength

and the extractor voltage, the lower limit of the electron energy resolution can be improved to $\Delta E = 0.3$ eV. This resolution is sufficient to resolve discrete energy sidebands in future PINEM experiments. Nevertheless, it must be noted that while the measurements of the minimum energy width provide meaningful insight into the intrinsic resolution of the source, the broadening observed at high laser pulse energies, when many electrons per pulse are not only generated at the tip but also arriving at the RFA, may not fully reflect the initial energy distribution of the electron pulse. Instead, additional broadening may occur from Coulomb repulsion inside the RFA, as electrons are decelerated and focused into the scanning electrode. The magnitude of this effect is not yet known and will require simulations to disentangle contributions of space-charge interactions within the RFA from intrinsic energy distributions.

The next step is to examine the temporal profile of the electron pulses using PINEM. The energy spread and pulse duration of electron beams are intrinsically linked with a negative chirp[228], as electrons with different energies propagate at different velocities, leading to a temporal broadening of the pulse. Measuring the pulses in time can therefore not only characterize the intrinsic pulse length but also help assess whether Coulomb repulsion inside the RFA contributes significantly to the measured energy width.

5.3.2. PULSE LENGTH MEASUREMENTS

To measure the temporal spread of the electron pulses, PINEM was employed to measure the cross-correlation between the electron beam and the laser pumped optical near field. In this approach, the relative delay between the electron pulse and the femtosecond laser pulse is scanned in time, and the strength of the PINEM interaction, quantified by the number of gain electrons, is recorded as a function of delay, Δt. The electron pulse duration can be deconvoluted from the measured envelop under the assumption of a Gaussian laser pulse, as the efficiency of the electron-photon coupling depends on their temporal overlap.

Pulse length measurements using PINEM (Figure 5.11, left column) were performed under the same operating conditions as the 10.6 keV current measurements (Figure 1.3) and energy spread measurements (Figure 5.9). Additionally, experiments performed with TH excitation are plotted in Figure 5.11 (right column). For the TH measurements, only 4155 V (optimized C1) and 3200 V configurations were explored. To distinguish the gain electrons generated by PINEM, the RFA voltage was set several volts above the ZLP of the electron beam, and the electron count rate was recorded. The delay, Δt, between the laser and electron pulses was scanned, where negative delays ($\Delta t < 0$) correspond to the laser arriving before the electron beam and probing the head of the electron pulse, while positive delays ($\Delta t > 0$) correspond to the laser arriving after the electron and probing the tail. These measurements were repeated as a function of laser pulse energy to the tip, ranging from regimes were space-charge effects are negligible to high excitation energies where they become significant.

The time traces in Figure 5.11 a & c demonstrate that under FH excitation and

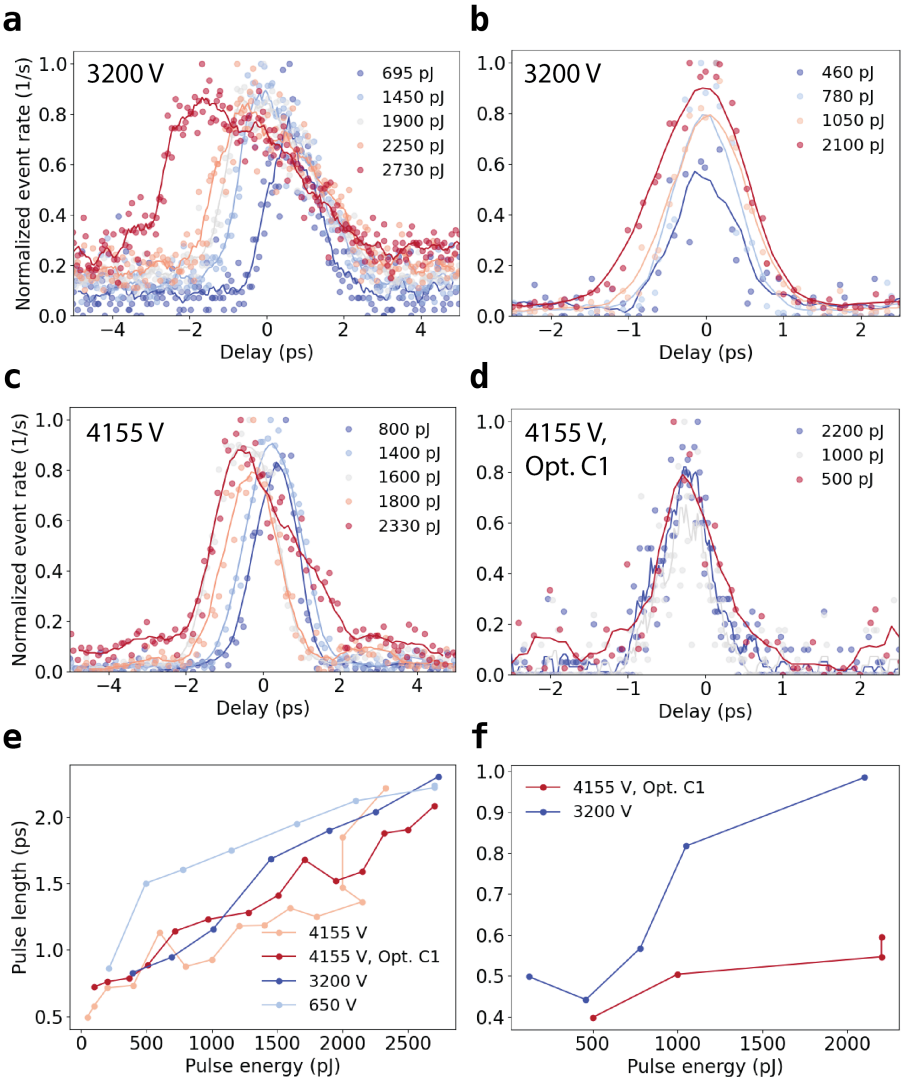

Figure 5.11: Electron-photon cross correlation measurements using PINEM to study the electron pulse length. (a-d) Normalized gain electron count rate as a function of relative delay between the electron and laser pulses for different laser pulse energies. (a-c) correspond to FH excitation at extractor voltages of 3200 V and 4155 V standard C1, respectively, while (b-d) correspond to TH excitation at 3200 V and 4155 V optimized C1. (e,f) Extracted pulse lengths (2×RMS) after deconvolution of the 300 fs laser pulse for the FH and TH.

extractor voltages of 3200 V and 4155 V respectively, the electron pulses broaden with increasing laser pulse energy. A similar trend is observed for TH excitation in Figures 5.11 b & d. For each decay trace, the root-mean-square (RMS) deviation was extracted and deconvoluted from the laser pulse duration (300 fs). The resulting pulse lengths, defined as 2 × RMS, are plotted in Figures 5.11 e & f. The RMS approach was used because at high laser pulse energies the temporal profiles are no longer well described by a single Gaussian, as the strong space charge effects cause the electron pulses to split into two bunches, as observed previously[60, 221]. Interestingly, the measured pulse width does not show a strong dependence on the extractor voltage, even when changing the C1 settings. This indicates that the temporal broadening occurs predominantly at the cathode tip and is not significantly influenced by clipping at the aperture, consistent with earlier findings in ref [60]. Additionally, excitation with the TH consistently produces shorter electron pulsed compared to FH, reflecting both the limited number of electrons per pulse in the TH, suppressing space-charge effects and resulting in a narrower energy and temporal profile.

It must be noted that, due to the nature of the RFA measurement, the lower-energy electrons must be filtered by the scanning electrode in order to resolve the gain electrons resulting from the PINEM interaction. Depending on the RFA threshold voltage, the filtering of the low-energy tail electrons may lead to an artificial reduction in the measured pulse duration, which can be a significant fraction of the total pulse, as demonstrated in Supplementary 5.5.1. A rigorous calculation of the electron pulse lengths would require to perform the measurement at a range of different RFA voltages, in order to reconstruct the full temporal profile.

Despite this limitation, it is a useful exercise to analytically calculate the estimated pulse lengths from the previously measured energy spreads, to compare them with the measurements.

5.3.3. ANALYTICAL CALCULATION

To analytically estimate the pulse lengths of the electron beam, we follow the approach outlined in ref [229], which solves the equations of motion to calculate the temporal broadening of the electron pulse, $\Delta t_{\text{arrival}}$, based on an initial uncertainty in kinetic energy, ΔE_i. In this model, electron propagation through the microscope is divided into three regions: (A) the first acceleration region from the cathode at 0 V to the extractor voltage, V_{ext}, with a distance d_{ext}, (B) the second acceleration region of length d_{acc} between the extractor and the anode, where the electrons are accelerated to their final energy V_{acc}, and (C) the drift region, where electrons propagate with their final energy over a distance l to the sample without further acceleration.

For the electron propagating in either the extractor and acceleration regions, the time of flight can be expressed as

$$t_{\text{ext/acc}} = \frac{d_{\text{ext/acc}}}{qV_{\text{ext/acc}}}\left[\frac{\sqrt{E_f^{\text{ext/acc}}\left(E_f^{\text{ext/acc}}+2mc^2\right)}}{c} - \frac{\sqrt{E_i^{\text{ext/acc}}\left(E_i^{\text{ext/acc}}+2mc^2\right)}}{c}\right] \tag{5.8}$$

where $E_i^{\text{ext/acc}}$ and $E_f^{\text{ext/acc}} = E_i^{\text{ext/acc}} + qV_{\text{ext/acc}}$ are the initial and final kinetic energies of the electron. The time spent in the drift region is given by

$$t_{\text{drift}} = \frac{l}{c}\left[\sqrt{\frac{E_f(E_f+2mc^2)+m^2c^4}{E_f(E_f+2mc^2)}}\right]. \tag{5.9}$$

The arrival time of the electron beam at the sample, t_{arrival} is thus the sum over these three regions, convolved with the temporal distribution of the laser exciting the cathode. By taking the derivative of this expression, the probability density function of the electron arrival time given a probability density function of energy can be calculated through

$$P(t) = P(E)\frac{dE}{dt}. \tag{5.10}$$

This model operates under several assumptions. Firstly, the electrons energies are considered relativistic, such that electrons of any kinetic energy can be directly substituted into the calculation. Secondly, the initial energy distribution is applied at a distance d_{start} from the tip, rather than a gradually accumulated along it's trajectory from Coulomb interactions. Thirdly, the effects of propagation angle and focusing lenses in the microscope are neglected. In our calculations, we use the energy spread data from the 3200 V measurements in Figure 5.9 a as the initial energy distribution. Accordingly, we set $V_{\text{ext}} = 3200$ V, $V_{\text{acc}} = 10600$ V, and $\sigma_{\text{laser}} = 127$ fs. Since the detailed geometry of the electron gun column is unavailable, we evaluate an envelop of pulse lengths by varying the distances of each region over realistic ranges, with $d_{\text{start}} = 5 - 500\,\mu$m, $d_{\text{ext}} = 400 - 600\,\mu$m, $d_{\text{acc}} = 10 - 40$ mm, and $l = 0.3 - 0.5$ m. Each distance parameter was varied independently over its range, while other distances were fixed at their average values. The results of these calculations are plotted in Figure 5.12.

Remarkably, these results show that the position of d_{start}, where the electrons acquire their initial energy spread, can have a substantial effect on the temporal distribution, as the electrons still have very low velocities in the extractor region. Onto the same graph we project the measured electron pulse lengths from Figure 5.11 e, with a one sided error bar of 50% that we consider a reasonable correction factor to account for the energy filtering introduced with the RFA (Supplementary 5.5.1). From this comparison, we conclude that the measurements and the analytical calculation are in good agreement, yielding pulse lengths of the same order of magnitude. Furthermore, as the measured and calculated temporal spreads share

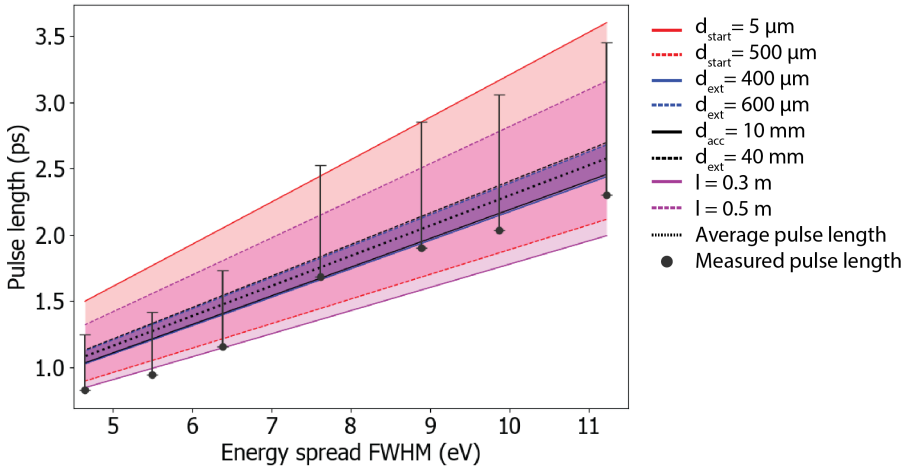

Figure 5.12: Calculated temporal distribution of electron pulses based on the measured energy spread data. The calculation divides the electron propagation into three regions, the extractor region, acceleration region, and drift region, with distances d_{ext}, d_{acc}, and l respectively. The envelop of the pulse length is obtained by sweeping the distances of each region over a range of reasonable values. The measured pulse lengths at the same experimental settings are projected onto the graph, with one-sided error bars of 50%, which we estimate as a correction factor to account for the effect of energy filtering with the RFA.

a similar slope, this suggests that the energy spread measured with the RFA are not dominated by Coulomb repulsion effects within the analyzer.

5.4. CONCLUSIONS

In this chapter, we have demonstrated for the first time that PINEM measurements can be successfully implemented in an USEM using an RFA. This achievement extends the capabilities of PINEM to a more affordable and accessible microscope, with unique advantages such as lower electron velocities that can enhance coupling efficiency, and the flexibility of a larger vacuum chamber enabling more complex light incoupling geometries and correlation with CL experiments. The implementation and alignment procedure required to perform PINEM in the SEM were outlined, and its capabilities were demonstrated through the near-field mapping of a DLA structure.

Furthermore, we showed that the RFA in combination with PINEM can be used to characterize the energy spread and temporal profile of the electron pulses, giving insights into how different gun parameters affect the pulse properties and may be optimized for high-resolution PINEM and EELS. At the same time, we identified that there are still significant uncertainties arising from Coulomb repulsion within the RFA, that can artificially broaden the measured energy distribution, and energy filtering by the RFA, that can artificially shorten the measured pulse length. These effects can be quantified and corrected in future work, through simulations

of the electron interactions inside the RFA and through voltage-dependent delay measurements.

Overall, the results presented in this chapter broaden the scope of studies of electron-light interaction in the SEM, providing a route to quantitative near-field mapping of photonic nanostructures, as well as electron wavepacket shaping.

5.5. SUPPLEMENTARY

5.5.1. EFFECT OF RFA FILTERING ON PULSE LENGTH MEASUREMENT

To investigate the artifacts introduced by the retarding field analyzer (RFA) when extracting electron pulse lengths using PINEM cross-correlation measurements, we performed a simple numerical calculation.

The electron beam was initialized using experimentally measured energy distributions from the V_{ext} = 650 V data set in Figure 5.9. The first case (Figure 5.1 a) was representative of a low-current electron pulse, with a single Gaussian peak of 2.7 eV FWHM. The second case (Figure 5.1 d) was representative of a high-current electron pulse with strong space-charge effects forming two energy bunches with FWHM 5.4 and 8.6 respectively. The initial temporal spread of the electron beams was assumed Gaussian and matched the FWHM of the laser excitation pulse. For the case of the double peaked spectrum, a 100 fs temporal offset was introduced between the two bunches. The electrons were then propagated along a 40 cm length, generating an arrival time distribution at the sample plane through velocity dispersion (Figure 5.1 b & e). A PINEM interaction was simulated by modifying the energy distributions into photon sidebands according to equation 5.3, using coupling strengths of g = 0.7 and 5 respectively to illustrate weak and strong coupling. Cross-correlation with laser induced near-field was simulated by scaling the coupling strength as a function of electron-laser overlap and calculating the energy modulation as a function of relative delay. To model the RFA, a threshold voltage V_{th} with a Gaussian uncertainty of 0.6 eV was applied after the PINEM interaction, to filter electrons with an energy of $E < V_{th}$. The effective pulse lengths were then extracted by calculating the RMS width from the energy modulation as a function of delay curves, for both the energy filtered and unfiltered cases (Figure 5.1 c & f). The contribution of the laser pulse was removed via deconvolution.

These calculations show that filtering above the ZLP systematically shortens the measured pulse duration, with progressive shorting of the measured pulse length with increasing threshold voltage. This effect becomes especially pronounced in the case of high-current electron beams due to strong chirping. Based on these calculations, filtering several volts above the ZLP requires a correction factor when interpreting experimentally measured values of at least 50% when interpreting experimentally measured pulse durations.

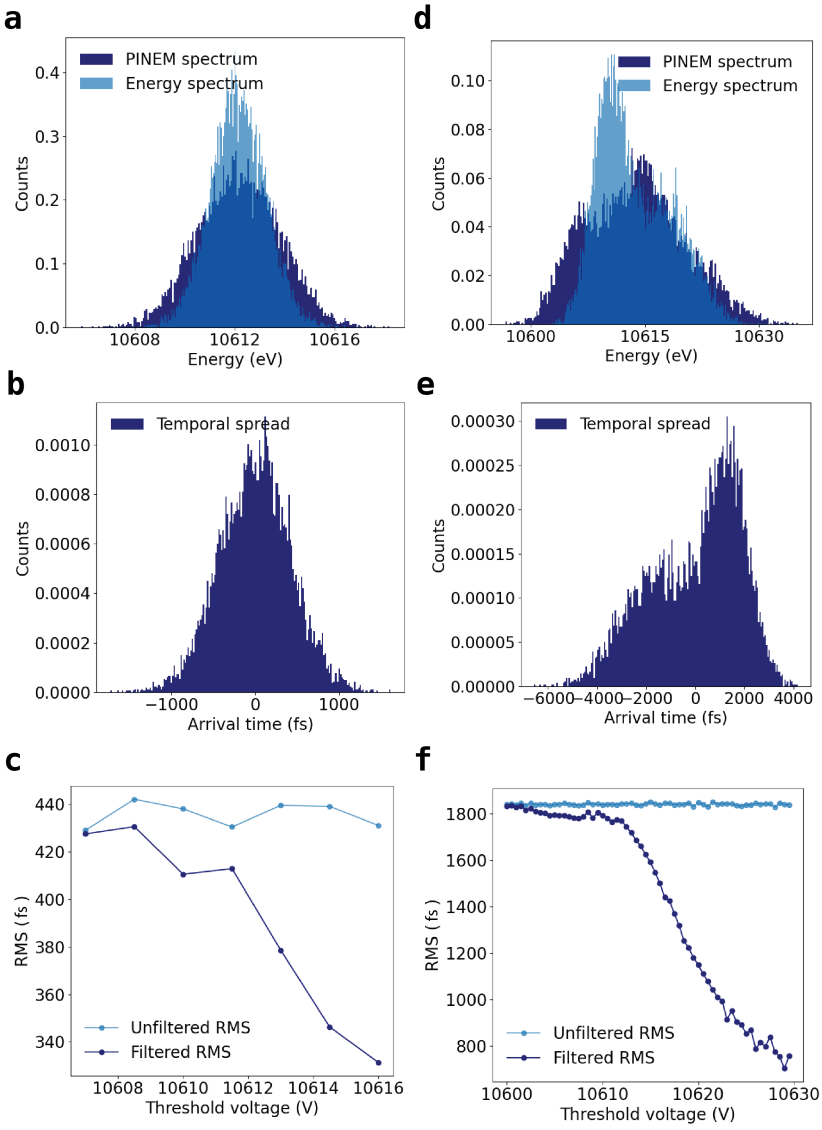

Supplementary Figure 5.1: Numerical calculation of PINEM cross-correlation traces with and without RFA filtering. (a & d) Electron energy distributions of low-current and high-current electron beams, before and after a PINEM interaction with coupling strengths of $g = 0.7$ and $g = 5$, respectively. (b & e) Simulated arrival-time distributions at the sample plane after 40 cm propagation for the low-current and high-current cases. (c & f) Extracted RMS widths from simulated cross-correlation traces with and without RFA filtering, as a function of threshold voltage, for the low-current and high-current electron beam respectively.

REFERENCES

[1] J. Strutt, *XV. On the light from the sky, its polarization and colour* , The London, Edinburgh, and Dublin Philosophical Magazine and Journal of Science **41**, 107 (1871).

[2] G. Mie, *Beiträge zur Optik trüber Medien, speziell kolloidaler Metallösungen,* Annalen der Physik **330**, 377 (1908).

[3] A. F. Koenderink, A. Alù, and A. Polman, *Nanophotonics: Shrinking light-based technology,* Science **348**, 516 (2015).

[4] M. Kneissl, A. Knorr, S. Reitzenstein, and A. Hoffmann, *Semiconductor Nanophotonics: Materials, Models, and Devices*, Vol. 194 (Springer Series in Solid-State Sciences, 2020).

[5] E. Abbe, *Beiträge zur Theorie des Mikroskops und der mikroskopischen Wahrnehmung,* Archiv f. mikrosk. Anatomie **9**, 413 (1873).

[6] S. W. Hell and J. Wichmann, *Breaking the diffraction resolution limit by stimulated emission: stimulated-emission-depletion fluorescence microscopy,* Optics Letters **19**, 780 (1994).

[7] A. F. Raigoza, J. W. Dugger, and L. J. Webb, *Review: Recent advances and current challenges in scanning probe microscopy of biomolecular surfaces and interfaces,* ACS Applied Materials and Interfaces **5**, 9249 (2013).

[8] R. F. Egerton and M. Watanabe, *Spatial resolution in transmission electron microscopy,* Micron **160**, 103304 (2022).

[9] J. J. Thomson, *Cathode rays,* Philosophical Magazine and Journal of Science **44**, 293 (1897).

[10] R. Sippel and E. Glover, *Structures in carbonate rocks made visible by luminescence petrography,* Science **150**, 1283 (1965).

[11] A. S. Marfunin, *Spectroscopy, Luminescence and Radiation Centers in Minerals* (Springer-Verlag, 1979).

[12] B. G. Yacobi and D. B. Holt, *Cathodoluminescence scanning electron microscopy of semiconductors,* Journal of Applied Physics **59**, R1 (1986).

[13] B. G. Yacobi and D. B. Holt, *Cathodoluminescence Microscopy of Inorganic Solids* (Springer, 1990).

[14] S. Fiedler, S. Morozov, D. Komisar, E. A. Ekimov, L. F. Kulikova, V. A. Davydov, V. N. Agafonov, S. Kumar, C. Wolff, S. I. Bozhevolnyi, and N. A. Mortensen, *Sub-to-super-poissonian photon statistics in cathodoluminescence of color center ensembles in isolated diamond crystals,* Nanophotonics **12**, 2231 (2023).

[15] S. Meuret, L. H. Tizei, F. Houdellier, S. Weber, Y. Auad, M. Tencé, H. C. Chang, M. Kociak, and A. Arbouet, *Time-resolved cathodoluminescence in an ultrafast transmission electron microscope,* Applied Physics Letters **119**, 062106 (2021).

[16] K. W. Mauser, M. Solà-Garcia, M. Liebtrau, B. Damilano, P. M. Coulon, S. Vézian, P. A. Shields, S. Meuret, and A. Polman, *Employing cathodoluminescence for nanothermometry and thermal transport measurements in semiconductor nanowires,* ACS Nano **15**, 11385 (2021).

[17] N. J. Schilder, H. Agrawal, E. C. Garnett, and A. Polman, *Phase-resolved surface plasmon scattering probed by cathodoluminescence holography,* ACS Photonics **7**, 1476 (2020).

[18] T. Coenen and A. Polman, *Polarization-sensitive cathodoluminescence fourier microscopy,* Optics Express **20**, 18679 (2012).

[19] T. Coenen and A. Polman, *Energy-momentum cathodoluminescence imaging of anisotropic directionality in elliptical aluminum plasmonic bullseye antennas,* ACS Photonics **6**, 573 (2019).

[20] F. J. García De Abajo, *Optical excitations in electron microscopy,* Reviews of Modern Physics **82**, 209 (2010).

[21] M. Liebtrau, M. Sivis, A. Feist, H. Lourenço-Martins, N. Pazos-Pérez, R. A. Alvarez-Puebla, F. J. García de Abajo, A. Polman, and C. Ropers, *Spontaneous and stimulated electron–photon interactions in nanoscale plasmonic near fields,* Light: Science and Applications **10**, 82 (2021).

[22] M. Kociak and O. Stéphan, *Mapping plasmons at the nanometer scale in an electron microscope,* Chemical Society Reviews **43**, 3865 (2014).

[23] V. L. Ginzberg, *Radiation by uniformly moving sources (vavilov-cherenkov effect, transition radiation, and other phenomena),* Physics - Uspekhi **39**, 973 (1996).

[24] B. J. Brenny, A. Polman, and F. J. García De Abajo, *Femtosecond plasmon and photon wave packets excited by a high-energy electron on a metal or dielectric surface,* Physical Review B **94**, 155412 (2016).

[25] J. van de Groep, T. Coenen, S. A. Mann, and A. Polman, *Direct imaging of hybridized eigenmodes in coupled silicon nanoparticles,* Optica **3**, 93 (2016).

[26] E. Akerboom, V. D. Giulio, N. J. Schilder, F. J. García de Abajo, and A. Polman, *Free electron-plasmon coupling strength and near-field retrieval through electron energy-dependent cathodoluminescence spectroscopy,* ACS Nano **18**, 13560 (2024).

[27] S. J. Smith and E. M. Purcell, *Visible light from localized surface charges moving across a grating,* Phys. Rev. **92**, 1069 (1953).

[28] A. Karnieli, D. Roitman, M. Liebtrau, S. Tsesses, N. V. Nielen, I. Kaminer, A. Arie, and A. Polman, *Cylindrical metalens for generation and focusing of free-electron radiation,* Nano Letters **22**, 5641 (2022).

[29] E. Akerboom, H. Sugimoto, M. Fujii, F. J. García de Abajo, and A. Polman, *Angle-resolved cathodoluminescence interferometry of plasmonic and dielectric scatterers,* Nano Letters **25**, 14264 (2025).

[30] R. F. Egerton, *Electron energy-loss spectroscopy in the TEM,* Reports on Progress in Physics **72**, 016502 (2009).

[31] A. Rothwarf, *Plasmon theory of electron-hole pair production: Efficiency of cathode ray phosphors,* Journal of Applied Physics **44**, 752 (1973).

[32] H. Raether, *Excitation of plasmons and interband transitions by electrons,* (Springer, 1980).

[33] C. A. Klein, *Radiation lonization energies in semiconductors: Speculations about the role of plasmons,* Proceeding of the International Conference on the Physics of Semiconductors. Journal of the Physical Society of Japan **21**, 307 (1966).

[34] M. Kociak and L. F. Zagonel, *Cathodoluminescence in the scanning transmission electron microscope,* Ultramicroscopy **176**, 112 (2017).

[35] J. M. Auerhammer and P. Rez, *Dipole-forbidden excitations in electron-energy-loss spectroscopy,* Physical Review B **40**, 2024 (1989).

[36] T. F. Kuech, *III-V compound semiconductors: Growth and structures,* Progress in Crystal Growth and Characterization of Materials **62**, 352 (2016).

[37] D. J. Frank, *Power-constrained CMOS scaling limits,* IBM Journal of Research and Development **46**, 235 (2002).

[38] J. A. D. Alamo, *Nanometre-scale electronics with III-V compound semiconductors,* Nature **479**, 317 (2011).

[39] S. K. Lim, M. Brewster, F. Qian, Y. Li, C. M. Lieber, and S. Gradečak, *Direct correlation between structural and optical properties of III - V nitride nanowire heterostructures with nanoscale resolution,* Nano Letters **9**, 3940 (2009).

[40] X. Zhou, M. Y. Lu, Y. J. Lu, E. J. Jones, S. Gwo, and S. Gradečak, *Nanoscale optical properties of indium gallium nitride/gallium nitride nanodisk-in-rod heterostructures,* ACS Nano **9**, 2868 (2015).

[41] S. Meuret, *Applications of photon bunching in cathodoluminescence,* in *Advances in Imaging and Electron Physics*, Vol. 215 (Elsevier, 2020) pp. 47–87.

[42] M. Solà-Garcia, K. W. Mauser, M. Liebtrau, T. Coenen, S. Christiansen, S. Meuret, and A. Polman, *Photon statistics of incoherent cathodoluminescence with continuous and pulsed electron beams,* ACS Photonics **8**, 916 (2021).

[43] M. Merano, S. Sonderegger, A. Crottini, S. Collin, P. Renucci, E. Pelucchi, A. Malko, M. H. Baier, E. Kapon, B. Deveaud, and J. D. Ganière, *Probing carrier dynamics in nanostructures by picosecond cathodoluminescence,* Nature **438**, 479 (2005).

[44] M. Taddei, S. Jariwala, R. J. Westbrook, S. Gallagher, A. C. Weaver, J. Pothoof, M. E. Ziffer, H. J. Snaith, and D. S. Ginger, *Interpreting halide perovskite semiconductor photoluminescence kinetics,* ACS Energy Letters **9**, 2508 (2024).

[45] X. Fu, G. Jacopin, M. Shahmohammadi, R. Liu, M. Benameur, J. D. Ganière, J. Feng, W. Guo, Z. M. Liao, B. Deveaud, and D. Yu, *Exciton drift in semiconductors under uniform strain gradients: Application to bent ZnO microwires,* ACS Nano **8**, 3412 (2014).

[46] A. David, N. G. Young, C. Lund, and M. D. Craven, *Review—The Physics of Recombinations in III-Nitride Emitters,* ECS Journal of Solid State Science and Technology **9**, 016021 (2020).

[47] M. Maiberg and R. Scheer, *Theoretical study of time-resolved luminescence in semiconductors. i. decay from the steady state,* Journal of Applied Physics **116**, 123710 (2014).

[48] M. Maiberg and R. Scheer, *Theoretical study of time-resolved luminescence in semiconductors. ii. pulsed excitation,* Journal of Applied Physics **116**, 123711 (2014).

[49] M. Maiberg, T. Hölscher, S. Zahedi-Azad, and R. Scheer, *Theoretical study of time-resolved luminescence in semiconductors. iii. trap states in the band gap,* Journal of Applied Physics **118**, 105701 (2015).

[50] W. Liu, C. Mounir, G. Rossbach, T. Schimpke, A. Avramescu, H. J. Lugauer, M. Strassburg, U. Schwarz, B. Deveaud, and G. Jacopin, *Spatially dependent carrier dynamics in single InGaN/GaN core-shell microrod by time-resolved cathodoluminescence,* Applied Physics Letters **112**, 052106 (2018).

[51] A. Bell, J. Christen, F. Bertram, F. A. Ponce, H. Marui, and S. Tanaka, *Localization versus field effects in single ingan quantum wells,* Applied Physics Letters **84**, 58 (2004).

[52] S. Sonderegger, E. Feltin, M. Merano, A. Crottini, J. F. Carlin, R. Sachot, B. Deveaud, N. Grandjean, and J. D. Ganière, *High spatial resolution picosecond cathodoluminescence of ingan quantum wells,* Applied Physics Letters **89**, 232109 (2006).

[53] S. Meuret, M. Solà-Garcia, T. Coenen, E. Kieft, H. Zeijlemaker, M. Lätzel, S. Christiansen, S. Y. Woo, Y. H. Ra, Z. Mi, and A. Polman, *Complementary cathodoluminescence lifetime imaging configurations in a scanning electron microscope,* Ultramicroscopy **197**, 28 (2019).

[54] M. J. Fransen, J. S. Faber, T. L. van Rooy, P. C. Tiemeijer, and P. Kruit, *Experimental evaluation of the extended Schottky model for ZrO/W electron emission,* Journal of Vacuum Science & Technology B: Microelectronics and Nanometer Structures Processing, Measurement, and Phenomena **16**, 2063 (1998).

[55] L. Zhang, J. P. Hoogenboom, B. Cook, and P. Kruit, *Photoemission sources and beam blankers for ultrafast electron microscopy,* Structural Dynamics **6**, 051501 (2019).

[56] I. G. Weppelman, R. J. Moerland, J. P. Hoogenboom, and P. Kruit, *Concept and design of a beam blanker with integrated photoconductive switch for ultrafast electron microscopy,* Ultramicroscopy **184**, 8 (2018).

[57] A. Feist, N. Bach, N. R. da Silva, T. Danz, M. Möller, K. E. Priebe, T. Domröse, J. G. Gatzmann, S. Rost, J. Schauss, S. Strauch, R. Bormann, M. Sivis, S. Schäfer, and C. Ropers, *Ultrafast transmission electron microscopy using a laser-driven field emitter: Femtosecond resolution with a high coherence electron beam,* Ultramicroscopy **176**, 63 (2017).

[58] B. Barwick, H. S. Park, O.-H. Kwon, J. S. Baskin, and A. H. Zewail, *4D imaging of transient structures and morphologies in ultrafast electron microscopy,* Science **322**, 1224 (2008).

[59] H. S. Park, J. S. Baskin, O. H. Kwon, and A. H. Zewail, *Atomic-scale imaging in real and energy space developed in ultrafast electron microscopy,* Nano Letters **7**, 2545 (2007).

[60] K. Moriová, P. Koutenský, M. C. Chirita-Mihaila, and M. Kozák, *Temporal characterization of femtosecond electron pulses inside ultrafast scanning electron microscope,* Review of Scientific Instruments **96**, 063706 (2025).

[61] D. S. Yang, O. F. Mohammed, and A. H. Zewail, *Scanning ultrafast electron microscopy,* PNAS **107**, 14993 (2010).

[62] R. Haindl, A. Feist, T. Domröse, M. Möller, J. H. Gaida, S. V. Yalunin, and C. Ropers, *Coulomb-correlated electron number states in a transmission electron microscope beam,* Nature Physics **19**, 1410 (2023).

[63] M. Bronsgeest, *Physics of Schottky electron sources: Theory and Optimum Operation* (Pan Stanford Publishing, 2014).

[64] M. M. Sola Garcia, *Electron-matter interaction probed with time-resolved cathodoluminescence*, Ph.D. thesis, Universiteit van Amsterdam (2021).

[65] M. Bronsgeest, *Physics of Schottky electron sources*, Ph.D. thesis, Technische Universiteit Delft (2009).

[66] H. J. Joyce, J. L. Boland, C. L. Davies, S. A. Baig, and M. B. Johnston, *A review of the electrical properties of semiconductor nanowires: Insights gained from terahertz conductivity spectroscopy,* Semiconductor Science and Technology **31**, 103003 (2016).

[67] L. Q. Phuong, M. Okano, Y. Yamada, A. Nagaoka, K. Yoshino, and Y. Kanemitsu, *Photocarrier localization and recombination dynamics in Cu_2ZnSnS_4 single crystals,* Applied Physics Letters **103**, 191902 (2013).

[68] A. Cavalleri, C. Tóth, C. W. Siders, J. A. Squier, F. Ráksi, P. Forget, and J. C. Kieffer, *Femtosecond structural dynamics in VO_2 during an ultrafast solid-solid phase transition,* Physical Review Letters **87**, 237401 (2001).

[69] A. H. Zewail, *Femtochemistry: Atomic-scale dynamics of the chemical bond using ultrafast lasers (nobel lecture),* Angewandte Chemie - International Edition **39**, 2586 (2000).

[70] M. C. Fischer, J. W. Wilson, F. E. Robles, and W. S. Warren, *Invited review article: Pump-probe microscopy,* Review of Scientific Instruments **87**, 031101 (2016).

[71] M. Kretschmar, E. Svirplys, M. Volkov, T. Witting, T. Nagy, M. J. J. Vrakking, and B. Schütte, *Compact realization of all-attosecond pump-probe spectroscopy,* Sci. Adv. **10**, eadk9605 (2024).

[72] V. A. Lobastov, R. Srinivasan, and A. H. Zewail, *Four-dimensional ultrafast electron microscopy,* PNAS **102**, 7069 (2005).

[73] K. B. Schliep, P. Quarterman, J. P. Wang, and D. J. Flannigan, *Picosecond fresnel transmission electron microscopy,* Applied Physics Letters **110**, 222404 (2017).

[74] D. R. Cremons, D. A. Plemmons, and D. J. Flannigan, *Femtosecond electron imaging of defect-modulated phonon dynamics,* Nature Communications **7**, 11230 (2016).

[75] D. T. Valley, V. E. Ferry, and D. J. Flannigan, *Imaging intra- and interparticle acousto-plasmonic vibrational dynamics with ultrafast electron microscopy,* Nano Letters **16**, 7302 (2016).

[76] G. Cao, S. Sun, Z. Li, H. Tian, H. Yang, and J. Li, *Clocking the anisotropic lattice dynamics of multi-walled carbon nanotubes by four-dimensional ultrafast transmission electron microscopy,* Scientific Reports **5**, 08404 (2015).

[77] S. Sun, L. Wei, Z. Li, G. Cao, Y. Liu, W. J. Lu, Y. P. Sun, H. Tian, H. Yang, and J. Li, *Direct observation of an optically induced charge density wave transition in 1T-$TaSe_2$,* Physical Review B - Condensed Matter and Materials Physics **92**, 224303 (2015).

[78] O. F. Mohammed, D. S. Yang, S. K. Pal, and A. H. Zewail, *4D scanning ultrafast electron microscopy: Visualization of materials surface dynamics,* Journal of the American Chemical Society **133**, 7708 (2011).

[79] B. Liao and E. Najafi, *Scanning ultrafast electron microscopy: A novel technique to probe photocarrier dynamics with high spatial and temporal resolutions,* Materials Today Physics **2**, 46 (2017).

[80] M. W. Garming, M. Bolhuis, S. Conesa-Boj, P. Kruit, and J. P. Hoogenboom, *Lock-in ultrafast electron microscopy simultaneously visualizes carrier recombination and interface-mediated trapping,* Journal of Physical Chemistry Letters **11**, 8880 (2020).

[81] M. W. Garming, I. G. C. Weppelman, M. Lee, T. Stavenga, and J. P. Hoogenboom, *Ultrafast scanning electron microscopy with sub-micrometer optical pump resolution,* Applied Physics Reviews **9**, 021418 (2022).

[82] M. Zani, V. Sala, G. Irde, S. M. Pietralunga, C. Manzoni, G. Cerullo, G. Lanzani, and A. Tagliaferri, *Charge dynamics in aluminum oxide thin film studied by ultrafast scanning electron microscopy,* Ultramicroscopy **187**, 93 (2018).

[83] M. Sola-Garcia, S. Meuret, T. Coenen, and A. Polman, *Electron-Induced State Conversion in Diamond NV Centers Measured with Pump-Probe Cathodoluminescence Spectroscopy,* ACS Photonics **7**, 232 (2020).

[84] B. Barwick, D. J. Flannigan, and A. H. Zewail, *Photon-induced near-field electron microscopy,* Nature **462**, 902 (2009).

[85] A. Feist, K. E. Echternkamp, J. Schauss, S. V. Yalunin, S. Schäfer, and C. Ropers, *Quantum coherent optical phase modulation in an ultrafast transmission electron microscope,* Nature **521**, 200 (2015).

[86] K. Wang, R. Dahan, M. Shentcis, Y. Kauffmann, A. B. Hayun, O. Reinhardt, S. Tsesses, and I. Kaminer, *Coherent interaction between free electrons and a photonic cavity,* Nature **582**, 50 (2020).

[87] E. Pomarico, I. Madan, G. Berruto, G. M. Vanacore, K. Wang, I. Kaminer, F. J. García De Abajo, and F. Carbone, *meV Resolution in Laser-Assisted Energy-Filtered Transmission Electron Microscopy,* ACS Photonics **5**, 759 (2018).

[88] O. Kfir, H. Lourenço-Martins, G. Storeck, M. Sivis, T. R. Harvey, T. J. Kippenberg, A. Feist, and C. Ropers, *Controlling free electrons with optical whispering-gallery modes,* Nature **582**, 46 (2020).

[89] O. Kfir, *Entanglements of electrons and cavity photons in the strong-coupling regime,* Physical Review Letters **123**, 103602 (2019).

[90] K. E. Priebe, C. Rathje, S. V. Yalunin, T. Hohage, A. Feist, S. Schäfer, and C. Ropers, *Attosecond electron pulse trains and quantum state reconstruction in ultrafast transmission electron microscopy,* Nature Photonics **11**, 793 (2017).

[91] G. M. Vanacore, I. Madan, G. Berruto, K. Wang, E. Pomarico, R. J. Lamb, D. McGrouther, I. Kaminer, B. Barwick, F. J. García De Abajo, and F. Carbone, *Attosecond coherent control of free-electron wave functions using semi-infinite light fields,* Nature Communications **9**, 2694 (2018).

[92] Y. Morimoto and P. Baum, *Diffraction and microscopy with attosecond electron pulse trains,* Nature Physics **14**, 252 (2018).

[93] R. Shiloh, T. Chlouba, and P. Hommelhoff, *Quantum-coherent light-electron interaction in a scanning electron microscope,* Physical Review Letters **128**, 23501 (2022).

[94] A. S. Nazligul, M. Wang, and K. L. Choy, *Recent development in earth-abundant kesterite materials and their applications,* Sustainability **12**, 5138 (2020).

[95] S. Kim, J. A. Márquez, T. Unold, and A. Walsh, *Upper limit to the photovoltaic efficiency of imperfect crystals from first principles,* Energy and Environmental Science **13**, 1481 (2020).

[96] F. Liu, Q. Zeng, J. Li, X. Hao, A. Ho-Baillie, J. Tang, and M. A. Green, *Emerging inorganic compound thin film photovoltaic materials: Progress, challenges and strategies,* Materials Today **41**, 120 (2020).

[97] S. Chen, J. H. Yang, X. G. Gong, A. Walsh, and S. H. Wei, *Intrinsic point defects and complexes in the quaternary kesterite semiconductor Cu_2ZnSnS_4,* Physical Review B **81**, 245204 (2010).

[98] M. A. Green, E. D. Dunlop, M. Yoshita, N. Kopidakis, K. Bothe, G. Siefer, X. Hao, and J. Y. Jiang, *Solar cell efficiency tables (version 65),* Progress in Photovoltaics: Research and Applications **33**, 3 (2025).

[99] M. Solà-Garcia, K. W. Mauser, N. van Nielen, T. Coenen, S. Meuret, and A. Polman, *Pump-probe cathodoluminescence microscopy,* (2021), arXiv:2112.03034.

[100] C. Yan, J. Huang, K. Sun, S. Johnston, Y. Zhang, H. Sun, A. Pu, M. He, F. Liu, K. Eder, L. Yang, J. M. Cairney, N. J. Ekins-Daukes, Z. Hameiri, J. A. Stride, S. Chen, M. A. Green, and X. Hao, *Cu_2ZnSnS_4 solar cells with over 10% power conversion efficiency enabled by heterojunction heat treatment,* Nature Energy **3**, 764 (2018).

[101] D. Abou-Ras, U. Bloeck, S. Caicedo-Dávila, A. Eljarrat, H. Funk, A. Hammud, S. Thomas, D. R. Wargulski, T. Lunkenbein, and C. T. Koch, *Correlative microscopy and monitoring of segregation processes in optoelectronic semiconductor materials and devices,* Journal of Applied Physics **133**, 121101 (2023).

[102] R. Schot, I. Schuringa, S. Fiedler, T. Veeken, B. Ehrler, and A. Polman, *Morphological effect on cathodoluminescence outcoupling in perovskite thin films,* Conference abstract, presented at the 3rd Workshop on Semiconductor Cathodoluminescence and Electron Beam Induced Current (2025).

[103] D. Drouin, A. R. Couture, D. Joly, X. Tastet, V. Aimez, and R. Gauvin, *Casino v2.42 - a fast and easy-to-use modeling tool for scanning electron microscopy and microanalysis users,* Scanning **29**, 92 (2007).

[104] M. Grossberg, P. Salu, J. Raudoja, and J. Krustok, *Microphotoluminescence study of Cu_2ZnSnS_4 polycrystals,* Journal of Photonics for Energy **3**, 030599 (2013).

[105] I. Pelant and J. Valenta, *Luminescence Spectroscopy of Semiconductors* (Oxford University Press, Oxford, 2012) pp. 1–560.

[106] M. Kuwahara, Y. Nambo, K. Aoki, K. Sameshima, X. Jin, T. Ujihara, H. Asano, K. Saitoh, Y. Takeda, and N. Tanaka, *The Boersch effect in a picosecond pulsed electron beam emitted from a semiconductor photocathode,* Applied Physics Letters **109**, 013108 (2016).

[107] K. Thonke, I. Tischer, M. Hocker, M. Schirra, K. Fujan, M. Wiedenmann, R. Schneider, M. Frey, and M. Feneberg, *Nanoscale characterisation of semiconductors by cathodoluminescence,* IOP Conference Series: Materials Science and Engineering **55**, 0122018 (2014).

[108] P. R. Edwards and R. W. Martin, *Cathodoluminescence nano-characterization of semiconductors,* Semiconductor Science and Technology **26**, 064005 (2011).

[109] K. Loeto, *Uncovering the carrier dynamics of AlInGaN semiconductors using time-resolved cathodoluminescence,* Materials Science and Technology **38**, 780 (2022).

[110] T. J. O'Hanlon, F. C. Massabuau, A. Bao, M. J. Kappers, and R. A. Oliver, *Directly correlated microscopy of trench defects in InGaN quantum wells,* Ultramicroscopy **231**, 113255 (2021).

[111] I. Dimkou, E. Di Russo, P. Dalapati, J. Houard, N. Rochat, D. Cooper, E. Bellet-Amarlic, A. Grenier, E. Monroy, and L. Rigutti, *InGaN quantum dots studied by correlative microscopy techniques for enhanced light-emitting diodes,* ACS Applied Nano Materials **3**, 10133 (2020).

[112] R. M. Kemper, P. Veit, C. Mietze, A. Dempewolf, T. Wecker, F. Bertram, J. Christen, J. K. Lindner, and D. J. As, *STEM-CL investigations on the influence of stacking faults on the optical emission of cubic GaN epilayers and cubic GaN/AlN multi-quantum wells,* Physica Status Solidi C **12**, 469 (2015).

[113] F. Bertram, G. Schmidt, J. Kernchen, P. Veit, H. Schürmann, A. Ćutuk, M. Jetter, P. Michler, and J. Christen, *Direct Imaging of the Carrier Capture into Individual InP Quantum Dots of a Semiconductor Disk Laser Membrane,* ACS Nano **16**, 4619 (2022).

[114] B. Ding, M. Frentrup, S. M. Fairclough, G. Kusch, M. J. Kappers, D. J. Wallis, and R. A. Oliver, *Multimicroscopy of cross-section zincblende GaN LED heterostructure,* Journal of Applied Physics **130**, 115705 (2021).

[115] R. Changizi, S. Zaefferer, L. Abdellaoui, and C. Scheu, *Effects of Defect Density on Optical Properties Using Correlative Cathodoluminescence and Transmission Electron Microscopy Measurements on Identical $PrNbO_4$ Particles,* ACS Applied Electronic Materials **4**, 2095 (2022).

[116] K. Keevend, T. Coenen, and I. K. Herrmann, *Correlative cathodoluminescence electron microscopy bioimaging: Towards single protein labelling with ultrastructural context,* Nanoscale **12**, 15588 (2020).

[117] M. I. Mitrofanov, G. V. Voznyuk, S. N. Rodin, W. V. Lundin, V. P. Evtikhiev, A. F. Tsatsulnikov, and M. A. Kaliteevski, *Calculation of the Ga+ FIB Ion Dose Distribution by SEM Image,* Semiconductors **54**, 1682 (2020).

[118] T. Sato, K. Nakano, H. Matsumoto, S. Torikawa, I. Nakatani, M. Kiyohara, and T. Isshiki, *High quality lamella preparation of gallium nitride compound semiconductor using Triple Beam™ system,* Journal of Physics: Conference Series **902**, 0192019 (2017).

[119] M. Schaffer, B. Schaffer, and Q. Ramasse, *Sample preparation for atomic-resolution STEM at low voltages by FIB,* Ultramicroscopy **114**, 62 (2012).

[120] S. Bals, W. Tirry, R. Geurts, Y. Zhiqing, and D. Schryvers, *High-quality sample preparation by low kV FIB thinning for analytical TEM measurements,* Microscopy and Microanalysis **13**, 80 (2007).

[121] A. Wolff, *Focused ion beams: An overview of the technology and its capabilities,* Wiley Analytical Science (2020).

[122] A. V. Sakharov, S. O. Usov, S. N. Rodin, W. V. Lundin, A. F. Tsatsulnikov, M. I. Mitrofanov, I. V. Levitskii, G. V. Voznyuk, M. A. Kaliteevskii, and V. P. Evtikhiev, *Effect of Annealing on Luminescence of InGaN/GaN Structures Etched by a Focused Ion Beam,* Semiconductors **53**, 2121 (2019).

[123] K. Loeto, S. M. Fairclough, I. Griffiths, G. Kusch, S. Ghosh, M. J. Kappers, N. Young, and R. A. Oliver, *Influence of Xe+ and Ga+ milling species on the cathodoluminescence of wurtzite and zincblende GaN,* Journal of Applied Physics **136**, 045702 (2024).

[124] F. U. Kosasih, G. Divitini, J. F. Orri, E. M. Tennyson, G. Kusch, R. A. Oliver, S. D. Stranks, and C. Ducati, *Optical emission from focused ion beam milled halide perovskite device cross-sections,* Microscopy Research and Technique **85**, 2351 (2022).

[125] A. F. F. Tsatsulnikov, W. V. V. Lundin, A. V. V. Sakharov, A. E. E. Nikolaev, E. E. E. Zavarin, S. O. O. Usov, M. A. A. Yagovkina, M. Hÿtch, M. Korytov, N. Cherkashin, A. F. Tsatsulnikov, W. V. Lundin, A. V. Sakharov, A. E. Nikolaev, E. E. Zavarin, S. O. Usov, M. A. Yagovkina, M. J. Hÿtch, M. Korytov, and N. Cherkashin, *Formation of three-dimensional islands in the active region of InGaN based light emitting diodes using a growth interruption approach,* Science of advanced materials **7**, 1629 (2015).

[126] N. Cherkashin, A. Louiset, A. Chmielewski, D. J. Kim, C. Dubourdieu, and S. Schamm-Chardon, *Quantitative mapping of strain and displacement fields over HR-TEM and HR-STEM images of crystals with reference to a virtual lattice,* Ultramicroscopy **253**, 113778 (2023).

[127] I. Olaniyan, I. Tikhonov, V. V. Hevelke, S. Wiesner, L. Zhang, A. Razumnaya, N. Cherkashin, S. Schamm-Chardon, I. Lukyanchuk, D. J. Kim, and C. Dubourdieu, *Switchable topological polar states in epitaxial $BaTiO_3$ nanoislands on silicon,* Nature Communications **15**, 10047 (2024).

[128] N. A. Bert, V. V. Chaldyshev, N. A. Cherkashin, V. N. Nevedomskiy, V. V. Preobrazhenskii, M. A. Putyato, B. R. Semyagin, V. I. Ushanov, and M. A. Yagovkina, *Metallic AsSb nanoinclusions strongly enriched by Sb in AlGaAsSb metamaterial,* Journal of Applied Physics **125**, 145106 (2019).

[129] S. N. Mohammad and H. Morkoc, *Progress and progress of group-III nitride semiconductors,* Progress in Quantum Electronics **20**, 361 (1996).

[130] G. Callsen, R. Butté, and N. Grandjean, *Probing Alloy Formation Using Different Excitonic Species: The Particular Case of InGaN,* Physical Review X **9**, 031030 (2019).

[131] C. Adelmann, J. Simon, G. Feuillet, N. T. Pelekanos, B. Daudin, and G. Fishman, *Self-assembled InGaN quantum dots grown by molecular-beam epitaxy,* Applied Physics Letters **76**, 1570 (2000).

[132] L. K. Lee, L. Zhang, H. Deng, and P. C. Ku, *Room-temperature quantum-dot-like luminescence from site-controlled InGaN quantum disks,* Applied Physics Letters **99**, 263105 (2011).

[133] D. Barettin, A. V. Sakharov, A. F. Tsatsulnikov, A. E. Nikolaev, A. Pecchia, M. Auf Der Maur, S. Y. Karpov, A. Pec-Chia, J. B. Wagner, and N. Cherkashin, *Impact of Local Composition on the Emission Spectra of InGaN Quantum-Dot LEDs,* Nanomaterials **13**, 1367 (2023).

[134] H.-M. Kim and T.-W. Kang, *Cathodoluminescence characteristics of InGaN/GaN quantum wells grown by MOCVD,* Materials Letters **48**, 263 (2001).

[135] D. Drouin, A. R. Couture, D. Joly, X. Tastet, V. Aimez, and R. Gauvin, *CASINO V2.42 - A fast and easy-to-use modeling tool for scanning electron microscopy and microanalysis users,* Scanning **29**, 92 (2007).

[136] L. F. Zagonel, L. H. Tizei, G. Z. Vitiello, G. Jacopin, L. Rigutti, M. Tchernycheva, F. H. Julien, R. Songmuang, T. Ostasevicius, F. De La Peña, C. Ducati, P. A. Midgley, and M. Kociak, *Nanometer-scale monitoring of quantum-confined Stark effect and emission efficiency droop in multiple GaN/AlN quantum disks in nanowires,* Physical Review B **93**, 205410 (2016).

[137] J. R. Lakowicz, *Principles of Fluorescence Spectroscopy,* 3rd ed. (Springer, Boston, MA, 2019).

[138] S. Meuret, T. Coenen, S. Y. Woo, Y. H. Ra, Z. Mi, and A. Polman, *Nanoscale Relative Emission Efficiency Mapping Using Cathodoluminescence g(2) Imaging,* Nano Letters **18**, 2288 (2018).

[139] M. A. Reshchikov, *On the Origin of the Yellow Luminescence Band in GaN,* Physica Status Solidi B **260**, 2200488 (2023).

[140] K. Loeto, G. Kusch, O. Brandt, P. M. Coulon, S. Hammersley, J. Lähnemann, I. Girgel, S. M. Fairclough, M. Sarkar, P. A. Shields, and R. A. Oliver, *Investigating the exciton dynamics in InGaN/GaN core-shell nanorods using time-resolved cathodoluminescence,* Nanotechnology **36**, 025703 (2024).

[141] G. E. Weng, W. R. Zhao, S. Q. Chen, H. Akiyama, Z. C. Li, J. P. Liu, and B. P. Zhang, *Strong localization effect and carrier relaxation dynamics in self-assembled InGaN quantum dots emitting in the green,* Nanoscale Research Letters **10**, 31 (2015).

[142] P. Dawson, S. Schulz, R. A. Oliver, M. J. Kappers, and C. J. Humphreys, *The nature of carrier localisation in polar and nonpolar InGaN/GaN quantum wells,* Journal of Applied Physics **119**, 181505 (2016).

[143] Y. Robin, E. A. Evropeitsev, T. V. Shubina, D. A. Kirilenko, V. Y. Davydov, A. N. Smirnov, A. A. Toropov, I. A. Eliseyev, S. Y. Bae, M. Kushimoto, S. Nitta, S. V.

Ivanov, and H. Amano, *Localization and transient emission properties in InGaN/GaN quantum wells of different polarities within core-shell nanorods,* Nanoscale **11**, 193 (2019).

[144] S. W. Feng, Y. C. Cheng, Y. Y. Chung, C. C. Yang, Y. S. Lin, C. Hsu, K. J. Ma, and J. I. Chyi, *Impact of localized states on the recombination dynamics in InGaN/GaN quantum well structures,* Journal of Applied Physics **92**, 4441 (2002).

[145] Y. R. Wu, Y. Y. Lin, H. H. Huang, and J. Singh, *Electronic and optical properties of InGaN quantum dot based light emitters for solid state lighting,* Journal of Applied Physics **105**, 013117 (2009).

[146] C. Haller, J.-f. Carlin, G. Jacopin, W. Liu, D. Martin, R. Butté, N. Grandjean, and a. GaN, *GaN surface as the source of non-radiative defects in InGaN/GaN quantum wells,* Applied Physics Letters **113**, 111106 (2018).

[147] I. H. Lee, A. Y. Polyakov, N. B. Smirnov, I. V. Shchemerov, P. B. Lagov, R. A. Zinov'Ev, E. B. Yakimov, K. D. Shcherbachev, and S. J. Pearton, *Point defects controlling non-radiative recombination in GaN blue light emitting diodes: Insights from radiation damage experiments,* Journal of Applied Physics **122**, 115704 (2017).

[148] H. Tsurusawa, N. Nakanishi, K. Kawano, Y. Chen, M. Dutka, B. Van Leer, and T. Mizoguchi, *Robotic fabrication of high-quality lamellae for aberration-corrected transmission electron microscopy,* Scientific Reports **11**, 21599 (2021).

[149] S. M. Olaizola, W. H. Fan, S. A. Hashemizadeh, J. P. Wells, D. J. Mowbray, M. S. Skolnick, A. M. Fox, and P. J. Parbrook, *Time-resolved photoluminescence studies of carrier diffusion in GaN,* Applied Physics Letters **89**, 072107 (2006).

[150] B. J. M. Brenny, *Probing light emission at the nanoscale with cathodoluminescence*, Ph.D. thesis, University of Amsterdam, Amsterdam (2016).

[151] F. Houdellier, G. M. Caruso, S. Weber, M. J. Hÿtch, C. Gatel, and A. Arbouet, *Optimization of off-axis electron holography performed with femtosecond electron pulses,* Ultramicroscopy **202**, 26 (2019).

[152] M. H. Huang, S. Mao, H. Feick, H. Yan, Y. Wu, H. Kind, E. Weber, R. Russo, and P. Yang, *Room-temperature ultraviolet nanowire nanolasers,* Science **292**, 1897 (2001).

[153] J. C. Johnson, H. J. Choi, K. P. Knutsen, R. D. Schaller, P. Yang, and R. J. Saykally, *Single gallium nitride nanowire lasers,* Nature Materials **1**, 106 (2002).

[154] C. Couteau, A. Larrue, C. Wilhelm, and C. Soci, *Nanowire lasers,* Nanophotonics **4**, 90 (2015).

[155] Q. Li, J. B. Wright, W. W. Chow, T. S. Luk, I. Brener, L. F. Lester, and G. T. Wang, *Single-mode GaN nanowire lasers,* Optics Express **20**, 17873 (2013).

[156] H. Xu, J. B. Wright, A. Hurtado, Q. Li, T. S. Luk, J. J. Figiel, K. Cross, G. Balakrishnan, L. F. Lester, I. Brener, and G. T. Wang, *Gold substrate-induced single-mode lasing of GaN nanowires,* Applied Physics Letters **101**, 221114 (2012).

[157] H. Xu, J. B. Wright, T. S. Luk, J. J. Figiel, K. Cross, L. F. Lester, G. Balakrishnan, G. T. Wang, I. Brener, and Q. Li, *Single-mode lasing of GaN nanowire-pairs,* Applied Physics Letters **101**, 113106 (2012).

[158] A. B. Greytak, C. J. Barrelet, Y. Li, and C. M. Lieber, *Semiconductor nanowire laser and nanowire waveguide electro-optic modulators,* Applied Physics Letters **87**, 1 (2005).

[159] P. Bhattacharya, A. Hazari, S. Jahangir, W. Guo, and T. Frost, *III-Nitride Electrically Pumped Visible and Near-Infrared Nanowire Lasers on (001) Silicon*, Vol. 96 (Academic Press Inc., 2017) pp. 385–409.

[160] J. A. Alanis, D. Saxena, S. Mokkapati, N. Jiang, K. Peng, X. Tang, L. Fu, H. H. Tan, C. Jagadish, and P. Parkinson, *Large-scale statistics for threshold optimization of optically pumped nanowire lasers,* Nano Letters **17**, 4860 (2017).

[161] S. A. Church, N. Patel, R. Al-Abri, N. Al-Amairi, Y. Zhang, H. Liu, and P. Parkinson, *Holistic nanowire laser characterization as a route to optimal design,* Advanced Optical Materials **11**, 2202476 (2023).

[162] S. A. Church, F. Vitale, A. Gopakumar, N. Gagrani, Y. Zhang, N. Jiang, H. H. Tan, C. Jagadish, H. Liu, H. Joyce, C. Ronning, and P. Parkinson, *Data-driven discovery for robust optimization of semiconductor nanowire lasers,* Laser and Photonics Reviews **19**, 2401194 (2025).

[163] B. Damilano, P. M. Coulon, S. Vézian, V. Brändli, J. Y. Duboz, J. Massies, and P. A. Shields, *Top-down fabrication of GaN nano-laser arrays by displacement Talbot lithography and selective area sublimation,* Applied Physics Express **12**, 045007 (2019).

[164] P. M. Coulon, B. Damilano, B. Alloing, P. Chausse, S. Walde, J. Enslin, R. Armstrong, S. Vézian, S. Hagedorn, T. Wernicke, J. Massies, J. Zúñiga-Pérez, M. Weyers, M. Kneissl, and P. A. Shields, *Displacement Talbot lithography for nano-engineering of III-nitride materials,* Microsystems and Nanoengineering **5**, 1 (2019).

[165] D. E. McCumber, *Einstein relations connecting broadband emission and absorption spectra,* Physical Review **136**, A954 (1964).

[166] H. Haug and S. W. Koch, *Quantum Theory of the Optical and Electronic Properties of Semiconductors*, 5th ed. (World Scientific, Singapore, 2009).

[167] M. A. Reshchikov, *Temperature dependence of defect-related photoluminescence in iii-v and ii-vi semiconductors,* Journal of Applied Physics **115**, 012010 (2014).

[168] J. Lähnemann, T. Flissikowski, M. Wölz, L. Geelhaar, H. T. Grahn, O. Brandt, and U. Jahn, *Quenching of the luminescence intensity of GaN nanowires under electron beam exposure: Impact of C adsorption on the exciton lifetime,* Physics Review Letters **27**, 455706 (2016).

[169] E. F. Schubert, I. D. Goepfert, W. Grieshaber, and J. M. Redwing, *Optical properties of Si-doped GaN,* Applied Physics Letters **71**, 921 (1997).

[170] Y. P. Varshni, *Temperature dependence of the energy gap in semiconductors,* Physica **34**, 149 (1967).

[171] B. J. Brenny, T. Coenen, and A. Polman, *Quantifying coherent and incoherent cathodoluminescence in semiconductors and metals,* Journal of Applied Physics **115**, 244307 (2014).

[172] W. Shan, T. J. Schmidt, X. H. Yang, S. J. Hwang, J. J. Song, and B. Goldenberg, *Temperature dependence of interband transitions in GaN grown by metalorganic chemical vapor deposition,* Applied Physics Letters , 985 (1995).

[173] D. G. Chtchekine, G. D. Gilliland, Z. C. Feng, S. J. Chua, D. J. Wolford, S. E. Ralph, M. J. Schurman, and I. Ferguson, *Temperature dependence of bound exciton emissions in GaN,* MRSJournal of Nitride Semiconductor Research **4**, 733 (1999).

[174] K. Paku, M. Wojdak, M. Palczewska, B. Suchanek, and J. M. Baranowski, *Luminescence and ESR Spectra of GaN:Si below and above Mott Transition,* MRS Internet Journal Nitride Semiconductor Research **3**, 1 (1998).

[175] M. A. Reshchikov, *Measurement and analysis of photoluminescence in gan,* Journal of Applied Physics **129**, 121101 (2021).

[176] L. H. Robins, K. A. Bertness, J. M. Barker, N. A. Sanford, and J. B. Schlager, *Optical and structural study of GaN nanowires grown by catalyst-free molecular beam epitaxy. II. Sub-band-gap luminescence and electron irradiation effects,* Journal of Applied Physics **101**, 113506 (2007).

[177] M. Almokhtar, N. A. All, J. Q. Almarashi, and H. Asahi, *Photoluminescence enhancement associated with the small size of GaN nanorods,* Journal of Alloys and Compounds **894**, 162408 (2022).

[178] M. Wahl, *Time-Correlated Single Photon Counting*, Tech. Rep. (PicoQuant GmbH, 2014).

[179] S. Thomson, *IRF Width & Minimum Measurable Lifetime in the FLS1000*, Tech. Rep. (Edinburgh Instruments Limited, 2023).

[180] B. Monemar, P. P. Paskov, J. P. Bergman, A. A. Toropov, T. V. Shubina, T. Malinauskas, and A. Usui, *Recombination of free and bound excitons in GaN,* Physica Status Solidi (B) Basic Research **245**, 1723 (2008).

[181] R. Calarco, T. Stoica, O. Brandt, and L. Geelhaar, *Surface-induced effects in GaN nanowires,* Journal of Materials Research **26**, 2157 (2011).

[182] S. W. Eaton, A. Fu, A. B. Wong, C. Z. Ning, and P. Yang, *Semiconductor nanowire lasers,* Nature Reviews Materials **1**, 1 (2016).

[183] C. Z. Ning, *Semiconductor nanolasers,* Physica Status Solidi (B) Basic Research **247**, 774 (2010).

[184] A. V. Maslov and C. Z. Ning, *Reflection of guided modes in a semiconductor nanowire laser,* Applied Physics Letters **83**, 1237 (2003).

[185] J. Mooney and P. Kambhampati, *Get the basics right: Jacobian conversion of wavelength and energy scales for quantitative analysis of emission spectra,* Journal of Physical Chemistry Letters **4**, 3316 (2013).

[186] H. Zhang, X. Deng, J. Zhang, D. Xue, Y. Huang, F. Bai, B. J. Inkson, and Y. Peng, *Phase transformation of Sn-based nanowires under electron beam irradiation,* Journal of Materials Chemistry C **3**, 5389 (2015).

[187] L. H. Tizei, V. Mkhitaryan, H. Lourenço-Martins, L. Scarabelli, K. Watanabe, T. Taniguchi, M. Tencé, J. D. Blazit, X. Li, A. Gloter, A. Zobelli, F. P. Schmidt, L. M. Liz-Marzán, F. J. García De Abajo, O. Stéphan, and M. Kociak, *Tailored nanoscale plasmon-enhanced vibrational electron spectroscopy,* Nano Letters **20**, 2973 (2020).

[188] A. Gale, C. Li, Y. Chen, K. Watanabe, T. Taniguchi, I. Aharonovich, and M. Toth, *Site-specific fabrication of blue quantum emitters in hexagonal boron nitride,* ACS Photonics **9**, 2170 (2022).

[189] F. J. García de Abajo, A. Polman, C. I. Velasco, M. Kociak, L. H. G. Tizei, O. Stéphan, S. Meuret, T. Sannomiya, K. Akiba, Y. Auad, A. Feist, C. Ropers, P. Baum, J. H. Gaida, M. Sivis, H. Lourenço-Martins, L. Serafini, J. Verbeeck, A. Konečná, N. Talebi, B. M. Ferrari, C. J. R. Duncan, M. G. Bravi, I. Ostroman, G. M. Vanacore, E. Nussinson, R. Ruimy, Y. Adiv, A. Niedermayr, I. Kaminer, V. D. Giulio, O. Kfir, Z. Zhao, R. Shiloh, Y. Morimoto, M. Kozák, P. Hommelhoff, F. Barantani, F. Carbone, F. Chahshouri, W. Albrecht, S. Rey, T. Coenen, E. Kieft, H. L. L. Robert, F. de Jong, and M. Solà-Garcia, *Roadmap for quantum nanophotonics with free electrons,* ACS Photonics **12**, 4760 (2025).

[190] H. Souissi, M. Gromovyi, T. Gueye, C. Brimont, L. Doyennette, D. Solnyshkov, G. Malpuech, E. Cambril, S. Bouchoule, B. Alloing, S. Rennesson, F. Semond, J. Zúñiga Pérez, and T. Guillet, *Ridge polariton laser: Different from a semiconductor edge-emitting laser,* Phys. Rev. Appl. **18**, 044029 (2022).

[191] H. Souissi, M. Gromovyi, I. Septembre, V. Develay, C. Brimont, L. Doyennette, E. Cambril, S. Bouchoule, B. Alloing, E. Frayssinet, J. Zúñiga-Pérez, T. Ackemann, G. Malpuech, D. D. Solnyshkov, and T. Guillet, *Mode-locked waveguide polariton laser,* Optica **11**, 962 (2024).

[192] F. J. García de Abajo and M. Kociak, *Electron energy-gain spectroscopy,* New Journal of Physics **10**, 073035 (2008).

[193] A. Peruzzo, M. Lobino, J. C. F. Matthews, N. Matsuda, A. Politi, K. Poulios, X.-Q. Zhou, Y. Lahini, N. Ismail, K. Wörhoff, Y. Bromberg, Y. Silberberg, M. G. Thompson, and J. L. Obrien, *Quantum walks of correlated photons,* Science **329**, 1500 (2010).

[194] S. T. Park, M. Lin, and A. H. Zewail, *Photon-induced near-field electron microscopy (PINEM): Theoretical and experimental,* New Journal of Physics **12**, 123028 (2010).

[195] F. J. Garcia De Abajo, A. Asenjo-Garcia, and M. Kociak, *Multiphoton absorption and emission by interaction of swift electrons with evanescent light fields,* Nano Letters **10**, 1859 (2010).

[196] S. Meuret, H. Lourenço-Martins, S. Weber, F. Houdellier, and A. Arbouet, *Photon-induced near-field electron microscopy of nanostructured metallic films and membranes,* ACS Photonics **11**, 977 (2024).

[197] T. T. Lummen, R. J. Lamb, G. Berruto, T. Lagrange, L. D. Negro, F. J. García De Abajo, D. McGrouther, B. Barwick, and F. Carbone, *Imaging and controlling plasmonic interference fields at buried interfaces,* Nature Communications **7**, 13156 (2016).

[198] D. Nabben, J. Kuttruff, L. Stolz, A. Ryabov, and P. Baum, *Attosecond electron microscopy of sub-cycle optical dynamics,* Nature **619**, 63 (2023).

[199] J. H. Gaida, H. Lourenço-Martins, M. Sivis, T. Rittmann, A. Feist, F. J. García de Abajo, and C. Ropers, *Attosecond electron microscopy by free-electron homodyne detection,* Nature Photonics **18**, 509 (2024).

[200] M. V. Tsarev, A. Ryabov, and P. Baum, *Free-electron qubits and maximum-contrast attosecond pulses via temporal Talbot revivals,* Physical Review Research **3**, 043033 (2021).

[201] N. Talebi, *Strong interaction of slow electrons with near-field light visited from first principles,* Physical Review Letters **125**, 080401 (2020).

[202] J. W. Henke, H. Jeng, and C. Ropers, *Probing electron-photon entanglement using a quantum eraser,* Physical Review A **111**, 012610 (2025).

[203] R. Shiloh, T. Chlouba, P. Yousefi, and P. Hommelhoff, *Particle acceleration using top-illuminated nanophotonic dielectric structures,* Optics Express **29**, 14403 (2021).

[204] R. Shiloh, J. Illmer, T. Chlouba, P. Yousefi, N. Schönenberger, U. Niedermayer, A. Mittelbach, and P. Hommelhoff, *Electron phase-space control in photonic chip-based particle acceleration,* Nature **597**, 498 (2021).

[205] J. W. Simonaitis, J. A. Alongi, B. Slayton, W. P. Putnam, K. K. Berggren, and P. D. Keathley, *Electron energy loss spectroscopy of 2D materials in a scanning electron microscope,* (2024), arXiv:2410.09291 .

[206] J. L. Erskine, *Electron energy analyzers,* Methods in Experimental Physics **29**, 209 (1995).

[207] P. Koutenský, N. L. Streshkova, K. Moriová, M. C. C. Mihaila, A. Knápek, D. Burda, and M. Kozák, *Ultrafast 4D scanning transmission electron microscopy for imaging of localized optical fields,* ACS Photonics **12**, 4452 (2025).

[208] A. Wöste, G. Hergert, T. Quenzel, M. Silies, D. Wang, P. Groß, and C. Lienau, *Ultrafast coupling of optical near fields to low-energy electrons probed in a point-projection microscope,* Nano Letters **23**, 5528 (2023).

[209] M. v.d. Heijden, *Energy spread measurement of the Nano Aperture Ion Source*, Master's thesis, Delft University of Technology (2011).

[210] M. Liebtrau, *Shaping the interplay of free electrons and light with optical metasurfaces*, Ph.D. thesis, Universiteit van Amsterdam (2023).

[211] H. Niese, M. Liebtrau, and A. Polman, *Photon-induced near-field electron microscopy in a Scanning Electron Microscope*, Master's thesis, AMOLF (2022).

[212] R. J. England, R. J. Noble, K. Bane, D. H. Dowell, C. K. Ng, J. E. Spencer, S. Tantawi, Z. Wu, R. L. Byer, E. Peralta, K. Soong, C. M. Chang, B. Montazeri, S. J. Wolf, B. Cowan, J. Dawson, W. Gai, P. Hommelhoff, Y. C. Huang, C. Jing, C. McGuinness, R. B. Palmer, B. Naranjo, J. Rosenzweig, G. Travish, A. Mizrahi, L. Schachter, C. Sears, G. R. Werner, and R. B. Yoder, *Dielectric laser accelerators,* Reviews of Modern Physics **86**, 1337 (2014).

[213] D. Cesar, S. Custodio, J. Maxson, P. Musumeci, X. Shen, E. Threlkeld, R. J. England, A. Hanuka, I. V. Makasyuk, E. A. Peralta, K. P. Wootton, and Z. Wu, *High-field nonlinear optical response and phase control in a dielectric laser accelerator,* Communications Physics **1**, 46 (2018).

[214] N. Talebi, *Schrödinger electrons interacting with optical gratings: Quantum mechanical study of the inverse Smith-Purcell effect,* New Journal of Physics **18**, 123006 (2016).

[215] J. Breuer and P. Hommelhoff, *Laser-based acceleration of nonrelativistic electrons at a dielectric structure,* Physical Review Letters **111**, 134803 (2013).

[216] T. R. Harvey, J. W. Henke, O. Kfir, H. Lourenço-Martins, A. Feist, F. J. García De Abajo, and C. Ropers, *Probing chirality with inelastic electron-light scattering,* Nano Letters **20**, 4377 (2020).

[217] M. Merano, S. Collin, P. Renucci, M. Gatri, S. Sonderegger, A. Crottini, J. D. Ganière, and B. Deveaud, *High brightness picosecond electron gun,* Review of Scientific Instruments **76**, 085108 (2005).

[218] S. Collin, M. Merano, M. Gatri, S. Sonderegger, P. Renucci, J. D. Ganière, and B. Deveaud, *Transverse and longitudinal space-charge-induced broadenings of ultrafast electron packets,* Journal of Applied Physics **98**, 094910 (2005).

[219] S. T. Park, O. H. Kwon, and A. H. Zewail, *Chirped imaging pulses in four-dimensional electron microscopy: Femtosecond pulsed hole burning,* New Journal of Physics **14**, 053046 (2012).

[220] D. A. Plemmons and D. J. Flannigan, *Ultrafast electron microscopy: Instrument response from the single-electron to high bunch-charge regimes,* Chemical Physics Letters **683**, 186 (2017).

[221] N. Bach, T. Domröse, A. Feist, T. Rittmann, S. Strauch, C. Ropers, and S. Schäfer, *Coulomb interactions in high-coherence femtosecond electron pulses from tip emitters,* Structural Dynamics **6**, 014301 (2019).

[222] P. K. Olshin, M. Drabbels, and U. J. Lorenz, *Characterization of a time-resolved electron microscope with a Schottky field emission gun,* Structural Dynamics **7**, 054304 (2020).

[223] M. S. Bronsgeest and P. Kruit, *Temperature dependence of the work function of the Zr/O/W(100) Schottky electron source in typical operating conditions and its effect on beam brightness,* Journal of Vacuum Science & Technology B: Microelectronics and Nanometer Structures Processing, Measurement, and Phenomena **24**, 887 (2006).

[224] K. S. Yeong and J. T. Thong, *Life cycle of a tungsten cold field emitter,* Journal of Applied Physics **99**, 104903 (2006).

[225] A. Michaelides, P. Hu, M. H. Lee, A. Alavi, and D. A. King, *Resolution of an ancient surface science anomaly: Work function change induced by N adsorption on W{100},* Physical Review Letters **90**, 246103 (2003).

[226] S. Ji, L. Piazza, G. Cao, S. T. Park, B. W. Reed, D. J. Masiel, and J. Weissenrieder, *Influence of cathode geometry on electron dynamics in an ultrafast electron microscope,* Structural Dynamics **4**, 054303 (2017).

[227] M. Aidelsburger, F. O. Kirchner, F. Krausz, and P. Baum, *Single-electron pulses for ultrafast diffraction,* Proceedings of the National Academy of Sciences of the United States of America **107**, 19714 (2010).

[228] P. Baum and A. Zewail, *Femtosecond diffraction with chirped electron pulses,* Chemical Physics Letters **462**, 14 (2008).

[229] A. Gahlmann, S. T. Park, and A. H. Zewail, *Ultrashort electron pulses for diffraction, crystallography and microscopy: Theoretical and experimental resolutions,* Physical Chemistry Chemical Physics **10**, 2894 (2008).

SUMMARY

Cathodoluminescence (CL) microscopy is a powerful technique for probing optical properties of materials with the nanoscale spatial resolution of an electron beam. The development of ultrafast scanning electron microscopes (USEMs), capable of generating picosecond pulsed electron beams, has further extended this approach into the time domain, making it possible to study dynamic processes. These advances have made CL a quintessential tool for investigating, among others, III-V semiconductor materials that form the basis of many modern technologies such as optoelectronics and renewable energy. With the addition of laser incoupling and electron energy spectroscopy, the ultrafast SEM can be further expanded into pump-probe schemes, providing a versatile platform to explore fundamental interactions between electrons, light, and matter.

In Chapter 2 we introduce our USEM based pump-probe cathodoluminescence (PP-CL) instrument, that combines femtosecond laser pulses and picosecond electron pulses generated by photoemission to measure dynamic material properties. We apply this technique to study the carrier recombination dynamics in Cu_2ZnSnS_4. With increasing laser excitation, we observe a blue-shift of the photoluminescence (PL) peak energy as well as a saturation of its intensity. This behavior is attributed to the filling of shallow radiative defect states near the valence band, as is commonly observed in doped semiconductors. However, this behavior is not observed under electron beam excitation with increasing electron current. We compare carrier generation mechanisms under electron-beam and laser-beam excitation. Because electron excitation occurs indirectly, the resulting carrier generation gradient is much smaller under our experimental conditions, highlighting the suitability of the electron beam as a probe in PP-CL. By performing PP-CL experiments, we observe that the CL signal is enhanced relative to its reference value, which we attribute to laser passivation of non-radiative defects in the sample. By fitting the PP-CL data, we directly extract the recombination rate, which cannot be directly measured with time-resolved CL (TR-CL), and measure a characteristic lifetime of 1.68 ± 0.78 ns. Under increased laser excitation, the CL intensity is suppressed, which we again attribute to the saturation of the shallow radiative defects. Because of the high repetition rate used for experiments, we could fit only a lower bound of 43 ns for the lifetime of these radiative defect states.

In Chapter 3, we use hyperspectral and TR-CL to study an InGaN/GaN quantum well (QW) sample before and after preparation as a lamella using focused ion beam milling (FIB). The accelerated ions in the FIB are known to introduce defects into the sample. To mitigate damage, strategies such as using low energy ions, tilted milling angles, and protective layer deposition are commonly employed. This has enabled FIB milling as a widely used method to prepare electron transparent sam-

ples for measurements in the transmission electron microscope (TEM), including CL studies. Nevertheless, the effect of the FIB on the luminescence properties of materials has seldom been systematically studied. Our sample underwent a growth interruption step during fabrication that etched the InGaN layer into regions containing 2D-confined quantum wells, and 3D-confined quantum discs (QD), resulting in a rich hyperspectral landscape with CL emission peaks ranging between 450 and 550 nm, due to varying degrees of quantum confinement. Lifetimes were measured for both the QD emission and QW emission by filtering with 450 and 550 nm bandpass filters. The QD emission followed a single exponential decay with a lifetime of 433 ± 1 ps, whereas the QW emission was best described by a biexponential decay with components of 1.864 ± 0.031 ns and 7.495 ± 0.136 ns, corresponding to recombination of weakly and strongly localized excitons respectively. The hyperspectral- and TR-CL measurements were repeated following the preparation of the sample as a FIB lamella. Due to the rich luminescence features of the sample, the same sample region could be identified, enabling direct correlation of the bulk and lamella measurements. Hyperspectral CL revealed strong quenching of the luminescence, primarily affecting the QW emission, that could not be explained by the increased transparency of the sample to the electron beam. TR-CL showed that the lifetime of the QD emission was decreased to 320 ± 20 ps, while the fast and slow recombination components of the QW emission were shortened to 111 ± 7 ps, and 550 ± 113 ps respectively. These decreases are characteristic of the introduction of non-radiative defects in the material by the FIB. The more pronounced suppression of QW emission is attributed to lateral carrier diffusion in QWs, enabling carriers to recombine non-radiatively at defects. In contrast, carrier confinement in QDs shields carriers from migrating to and recombining at defect sites.

In Chapter 4, we use the light-incoupling capabilities of the PP-CL microscope to study the lasing properties of GaN nanowire (NW) lasers. Combined with temperature -resolved hyperspectral CL, TR-CL and secondary electron imaging, we correlate the optical and structural properties of individual NWs. CL measurements are used to characterize the gain medium itself, revealing temperature-independent but diameter-dependent lifetimes, demonstrating that recombination is limited by non- radiative surface defects. Furthermore, non-monotonic spectral peak shifting with decreasing temperature points to exciton localization at shallow radiative defects that influence the emission. We then investigate the lasing properties of single NWs transferred onto a planar Si substrate, and determine the lasing threshold as a function of NW geometry. The lasing thresholds systematically decrease with increasing NW aspect ratio (diameter/length). In contrast, NWs dispersed onto a carbon TEM grid showed no systematic dependence of the lasing threshold on aspect ratio, highlighting the strong influence of the local dielectric environment on lasing. Finally, we show how electron beam irradiation of the NWs can be used to influence lasing. While the lasing threshold remained unchanged, the modal distribution is modified, opening possibilities for using electron beams for mode selection.

Finally, in Chapter 5, we reconfigure the PP-CL set-up from Chapter 2 to integrate an electron energy spectrometer, enabling photon-induced near-field mi-

croscopy (PINEM) experiments and measure optical near-fields at the nanometer scale. Implementing PINEM in an SEM offers the advantages of using slower electron velocities that can boost electron-light coupling, as well as the flexibility of combining PINEM and CL and advanced light incoupling configurations enabled by the larger vacuum chamber of the SEM. To overcome the lack of commercially available electron energy spectrometers, we use a retarding field analyzer (RFA) equipped with an Advacam MiniPix electron detector. We describe the technical integration and the alignment procedures for PINEM. As a sample, we use a dielectric laser accelerator (DLA) structure consisting of a dual silicon nanocylinder metasurface channel. This geometry enhances the electron-light coupling strength, quantified by the factor g, as the electron interacts with a phase-matched optical mode co-propagating along the metasurface over multiple optical cycles, thereby simplifying the temporal overlap procedure. Under 1034 nm illumination, a 10.6 keV electron beam couples to the third spatial harmonic of the structure. As a result of the PINEM interaction, the electron energy spectrum gains additional sidebands of energy, and the energy modulation is exploited to map the near-field. From spectral fitting, we extract an average coupling strength of $g = 0.68 \pm 0.43$, although we note that there is a large distribution of Δg due to averaging over both space and time. In some cases, electrons gain up to 24 energy sidebands. Using the RFA and PINEM cross-correlation measurements, we then characterize the energy spread and pulse length of the photoemitted electron pulses as a function of different gun parameters. By decreasing the extractor voltage, lowering the laser trigger photon energy, and operating in a regime with strictly < 1 electron per pulse (avoiding Coulomb repulsion), the energy resolution of the electron beam is decreased from the standard $\Delta E = 0.74 \pm 0.05$ eV (typical for a continuous 1800 K Schottky field emission gun) to $\Delta E = 0.3 \pm 0.03$ eV. Using PINEM cross-correlation, we measure the electron pulse lengths of a 10.6 keV electron beam as a function of laser trigger pulse energy, finding durations of 0.5 ps to 2.3 ps, broadened by the velocity dispersion of electrons as a result of Coulomb interactions. We discuss the uncertainties introduced due to electron interaction within the RFA and due to energy filtering, noting that these can be improved through modeling of the set-up.

This thesis demonstrates how USEMs with light incoupling capabilities form a powerful and versatile platform for investigating the optical, electronic, and dynamic properties of a range of material systems. Using PP-CL we directly probed non-radiative recombination dynamics, employed correlative CL measurements to reveal how the standard practice of FIB lamella preparation alters the luminescence properties of materials, and correlated nanowire lasing properties to material and geometric characteristics. We further expanded the PP-CL USEM with the integration of an electron energy spectrometer, enabling PINEM experiments within the USEM. This advancement allows the study of optical near-fields and probing electron-light interactions with enhanced coupling strength and flexibility for integration with CL experiments. Together, these results extend the reach of ultrafast scanning electron microscopy into new regimes for material science and nanophotonics.

SAMENVATTING

Cathodoluminescentie (CL) microscopie is een krachtige techniek om optische eigenschappen van materialen te onderzoeken met de nanometerschaal ruimtelijke resolutie van een elektronenbundel. De ontwikkeling van ultrasnelle scanning elektronen microscopen (USEMs), die picoseconde gepulste elektronenbundels kunnen genereren, heeft deze methode verder uitgebreid naar het tijdsdomein, waardoor het mogelijk is dynamische processen te bestuderen. Deze vooruitgangen hebben CL tot een essentieel instrument gemaakt voor het onderzoeken van onder andere III-V halfgeleidermaterialen, die de basis vormen van veel moderne technologieën zoals opto-elektronica en hernieuwbare energie. Met de toevoeging van laserinvoer en elektronen-energie spectroscopie kan de ultrasnelle SEM verder worden uitgebreid naar pump-probe schema's, wat een veelzijdig platform biedt om fundamentele interacties tussen elektronen, licht en materie te verkennen.

In Hoofdstuk 2 introduceren we ons USEM-gebaseerde pump-probe cathodoluminescentie (PP-CL) instrument, dat femtoseconde laserpulsen en picoseconde elektronenpulsen, gegenereerd door foto-emissie, combineert om dynamische materiaaleigenschappen te meten. We passen deze techniek toe om de ladingdrager-recombinatie dynamica in Cu_2ZnSnS_4 te bestuderen. Bij toenemende laser-excitatie observeren we een blauwverschuiving van de fotoluminescentie piekenergie en een verzadiging van de intensiteit. Dit gedrag wordt toegeschreven aan de vulling van ondiepe radiatieve defecten nabij de valentieband, zoals vaak wordt waargenomen in gedoopte halfgeleiders. Onder elektronenbundel-excitatie met toenemende stroom wordt dit gedrag niet gezien. We vergelijken de ladingsgeneratiemechanismen onder elektronen- en laser-excitatie. Omdat elektronen-excitatie indirect plaatsvindt, is de resulterende ladingsgeneratiegradiënt veel kleiner onder onze experimentele omstandigheden, wat de geschiktheid van de elektronenbundel als probe in PP-CL benadrukt. Door PP-CL experimenten uit te voeren, observeren we dat het CL-signaal wordt versterkt ten opzichte van de referentiewaarde, wat we toeschrijven aan laser-passivatie van niet radiatieve defecten in het monster. Door de PP-CL data te fitten, extraheren we rechtstreeks de recombinatiesnelheid, die niet direct kan worden gemeten met tijdsopgeloste CL (TR-CL), en meten we een karakteristieke levensduur van 1.68 ± 0.78 ns. Bij verhoogde laser-excitatie wordt de CL-intensiteit onderdrukt, wat opnieuw wordt toegeschreven aan de verzadiging van de ondiepe radiatieve defecten. Vanwege de hoge herhalingsfrequentie van de laser konden we slechts een ondergrens fitten van 43 ns voor de levensduur van deze radiatieve defecten.

In Hoofdstuk 3 gebruiken we hyperspectrale en TR-CL metingen om een InGaN/GaN kwantumput (KP) monster te onderzoeken, voor en na preparatie als lamel met behulp van een gefocuste ionenbundel (FIB) frezen. De versnelde ionen

in de FIB staan erom bekend defecten in het monster te introduceren. Om schade te beperken worden strategieën toegepast zoals lage energie ionen, gefreesde hoeken en beschermende lagen. Dit heeft FIB-frezen mogelijk gemaakt als een veelgebruikte methode om elektronen-transparante monsters te fabriceren voor transmissie-elektronenmicroscopie (TEM), inclusief CL-studies. Toch is het effect van FIB op de luminescentie-eigenschappen zelden systematisch bestudeerd. Ons monster onderging een groeionderbreking tijdens de fabricatie, waarbij de InGaN-laag werd geëtst in regio's met 2D-opgesloten kwantumputten (KP, "quantum wells") en 3D-opgesloten kwantumdeeltjes (KD, "quantum dics"), wat resulteerde in een rijke hyperspectrale structuur met CL-emissiepieken tussen 450 en 550 nm, als gevolg van verschillende gradaties van kwantumconfinment. De levensduren werden gemeten voor zowel de KD-emissie als de KP-emissie met banddoorlaatfilters van 450 en 550 nm. De KD-emissie volgde een enkelvoudig exponentieel verval met een levensduur van 433 ± 1 ps, terwijl de KP-emissie het best werd beschreven door een dubbel exponentieel verval met componenten van 1.864 ± 0.031 ns en 7.495 ± 0.136 ns, overeenkomend met recombinatie van respectievelijk zwak en sterk gelokaliseerde excitonen. Hyperspectrale- en TR-CL-metingen werden herhaald na FIB-preparatie. Vanwege de rijke luminescentiekenmerken kon dezelfde regio worden geïdentificeerd, waardoor directe correlatie mogelijk was. Hyperspectrale CL onthulde sterke quenching van de luminescentie, vooral in de KP-emissie, die niet kon worden verklaard door de verhoogde transparantie van het monster voor de elektronenbundel. TR-CL toonde dat de levensduur van de KD-emissie werd verkort tot 320 ± 20 ps, terwijl de snelle en langzame recombinatiecomponenten van de KP-emissie werden verkort tot respectievelijk 111 ± 7 ps en 550 ± 113 ps. Deze afnames zijn kenmerkend voor de introductie van niet radiatieve defecten door FIB. De meer uitgesproken onderdrukking van KP-emissie wordt toegeschreven aan laterale ladingsdiffusie in KP's, waardoor ladingsdragers niet radiatief recombineren bij defecten. Daarentegen beschermt confinering in KD's ladingsdragers tegen migratie en recombinatie bij defectplaatsen.

In Hoofdstuk 4 gebruiken we de lichtinvoer mogelijkheden van de PP-CL microscoop om de lasingeigenschappen van GaN nanodraad (NR) lasers te bestuderen. In combinatie met temperatuurafhankelijke hyperspectrale CL, TR-CL en secundaire elektronenbeeldvorming correleren we de optische en structurele eigenschappen van individuele NR's. CL-metingen worden gebruikt om het versterkingsmedium zelf te karakteriseren, waarbij temperatuuronafhankelijke maar diameterafhankelijke levensduren worden onthuld. Dit toont aan dat recombinatie wordt beperkt door niet radiatieve oppervlakte-defecten. Verder wijst een niet-monotone spectrale piekverschuiving bij dalende temperatuur op excitonlokalisatie aan ondiepe radiatieve defecten die de emissie beïnvloeden. We onderzoeken vervolgens de lasingeigenschappen van afzonderlijke NR's die op een Si-substraat zijn geplaatst, en bepalen de drempelwaarde als functie van de NR-geometrie. De lasing drempels nemen systematisch af bij toenemende NR-aspectratio (diameter/lengte). Daarentegen vertoonden NR's op een koolstof TEM-raster geen systematisch verband tussen drempel en aspectratio, wat het sterke effect van de lokale diëlektrische omgeving benadrukt. Tot slot tonen we aan dat elektronenbundelbestral-

ing kan worden gebruikt om het lasinggedrag te beïnvloeden. Hoewel de drempel onveranderd bleef, werd de modale verdeling gewijzigd, wat mogelijkheden opent voor elektronenbundel-gebaseerde modusselectie.

In Hoofdstuk 5 herconfigureren we de PP-CL opstelling uit Hoofdstuk 2 om een elektronen-energiespectrometer te integreren, waarmee foton-geïnduceerde nabijveld elektronenmicroscopie (FINEM) experimenten mogelijk worden en optische nabijvelden op nanometerschaal gemeten kunnen worden. Het implementeren van FINEM in een SEM biedt voordelen zoals tragere elektronen, die de koppeling met licht versterken, en de flexibiliteit om FINEM en CL te combineren dankzij de grotere vacuümkamer van de SEM. Om het gebrek aan commerciële elektronen-energiespectrometers te omzeilen, gebruiken we een retarding field analyzer (RFA) met een Advacam MiniPix detector. We beschrijven de technische integratie en uitlijnprocedures. Als monster gebruiken we een diëlektrische laseraccelerator (DLA) structuur bestaande uit een dubbele silicium-nanocilinder metasurface-kanaal. Deze geometrie versterkt de elektronen-licht koppeling, gekwantificeerd door de factor g, doordat de elektron interacteert met een fase- gematchte optische mode die langs de metasurface co-propageert over meerdere optische cycli. Onder 1034 nm belichting koppelt een 10.6 keV elektronenbundel aan de derde ruimtelijke harmonische van de structuur. Als resultaat van de FINEM-interactie ontstaan er extra zijbanden in het elektronen-energiespectrum, en de energiemodulatie wordt benut om het nabijveld in kaart te brengen. Uit spectrale fits extraheren we een gemiddelde koppelingsterkte van $g = 0.68 \pm 0.43$, hoewel we noteren dat er een grote spreiding in Δg is. In sommige gevallen verkrijgen elektronen tot wel 24 energie-zijbanden. Met behulp van de RFA en FINEM-crosscorrelatie meten we de energieverdeling en pulsduur van de foto geëmitteerde elektronenpulsen als functie van verschillende parameters. Door de extractor-spanning te verlagen, de fotonenergie van de trigger-laser te reduceren en te werken in een regime met strikt < 1 elektron per puls (zonder Coulomb-repulsie), kon de energie-resolutie worden verbeterd van $\Delta E = 0.74 \pm 0.05$ eV (standaard bij een continue 1800 K Schottky bron) naar $\Delta E = 0.3 \pm 0.03$ eV. Met FINEM-crosscorrelatie maten we pulsduurtes van 0.5 ps tot 2.3 ps, verbreed door snelheidsdispersie als gevolg van Coulomb-interacties.

Dit proefschrift demonstreert hoe USEM's met lichtinvoer een krachtig en veelzijdig platform vormen voor het onderzoeken van optische, elektronische en dynamische eigenschappen van diverse materiaalsystemen. Met PP-CL hebben we niet radiatieve recombinatiedynamica direct onderzocht, correlatieve CL-metingen uitgevoerd die aantoonden hoe standaard FIB-lamel-preparatie de luminescentie-eigenschappen verandert, en nanodraad-lasingeigenschappen gekoppeld aan materiaal en geometriekenmerken. We hebben de PP-CL USEM verder uitgebreid met een elektronen-energiespectrometer, waarmee FINEM-experimenten binnen de USEM mogelijk zijn. Deze uitbreiding maakt het mogelijk optische nabijvelden te bestuderen en elektron-licht interacties te onderzoeken met verbeterde koppeling en integratie met CL-experimenten. Samen breiden deze resultaten het bereik van ultrasnelle scanning-elektronenmicroscopie uit naar nieuwe domeinen in de materiaalwetenschappen en nanofotonica.

AUTHOR CONTRIBUTIONS AND PUBLICATIONS

Chapter 2

Author contributions:
Nika van Nielen performed the experiments, analysis, interpretation, and wrote the manuscript. *Magda Solà-Garcia* co-performed the pump-probe experiments and supervised *Marnix Vreugdenhil* who performed time-resolved luminescence characterization of the same sample. *Xiaojing Hao* provided the CZTS sample. *Sophie Meuret* helped with interpretation and editing of the manuscript. *Albert Polman* edited the manuscript and supervised the project.

Associated publication:
N. van Nielen, M. Solà-Garcia, M. Vreugdenhil, X. Hao, S. Meuret, A. Polman, *Time resolved pump-probe cathodoluminescence microscopy on* Cu_2ZnSnS_4, in preparation.

Chapter 3

Author contributions:
Nika van Nielen performed the SEM-CL experiments, analysis, interpretation, and wrote the manuscript. *Luiz H. G. Tizei* performed TEM-CL measurements. *Delphine Lagard* performed time-resolved photoluminescence measurements. *Cleo Santini* and *Florian Castioni* had supporting roles in TEM-CL experiments. *Robin Cours* performed the lamella preparation. *Andrea Balocchi* supervised the TR-PL measurements. *Teresa Hungria* performed TEM measurements. *Andrew F. Tsatsulnikov, Alexei V. Sakharov,* and *Andrew. E. Nikolaev* fabricated the InGaN qauntum well sample. *Nikolay Cherkashin* performed the strain-state analysis. *Albert Polman* co-supervised the project together with *Sophie Meuret* who supervised and conceptualized the project as well as did the TEM-CL analysis. All authors participated in revision of the manuscript.

Associated publication:
N. van Nielen, L. H. G. Tizei, D. Lagarde, C. Santini, F. Castioni, R. Cours, A. Balocchi, T. Hungria, A. F. Tsatsulnikov, A. V. Sakharov, A. E. Nikolaiev, N. Cherkashin, A. Polman, S. Meuret, *Effects of lamella preparation on InGaN quantum well luminescence*, Appl. Phys. Lett. **127**, 222101 (2025).

Chapter 4

Author contributions:
Nika van Nielen performed the SEM-CL and lasing experiments, analysis, interpretation, and writing. *Benjamin Damilano* fabricated the samples. *Cleo Santini* performed μ-PL experiments in the lab of *Thierry Guillet*. *Sophie Meuret* and *Albert Polman* edited the text and supervised the work.

Chapter 5

Author contributions:
Nika van Nielen performed the experiments, analysis, and wrote the manuscript. She built the set up together with *Thomas Chlouba* and AMOLF technical support departments†. *Thomas Chlouba* performed the FDTD simulations of the DLA sample. *Magda Solà-Garcia* performed the 5 keV energy spread measurements and analytically calculated the electron pulse length. *Matthias Liebtrau* built the RFA based on the design of *Pieter Kruit* who also consulted on the energy spread data. *Leon Brueckner, Julian Litzel,* and *Roy Shiloh* designed and fabricated the DLA structure under the supervision of *Peter Hommelhoff*. *Sophie Meuret* commented on the manuscript, together with *Albert Polman* who supervised the project.

Associated publications:
T. Chlouba*, N. van Nielen*, M. Liebtrau, L. Brueckner, J. Litzel, R. Shiloh, P. Hommelhoff, S. Meuret, A. Polman, *Electron-light coupling in an ultrafast scanning electron microscope*, in preparation.

M. Solà-Garcia*, N. van Nielen*, T. Chlouba*, M. Liebtrau, E. Kieft, L. Brueckner, J. Litzel, R. Shiloh, P. Hommelhoff, P. Kruit, S. Meuret, A. Polman, *Electron energy spread in an ultrafast scanning electron microscope*, in preparation.

†Special thanks to Max Postma, Bob Krijger, and Ulas Demirtas
*These authors contributed equally to the work

Other

N. van Nielen, N. Schilder, M. Hentschel, H. Giessen, A. Polman, N. Talebi, *Electrons generate self-complementary broadband vortex light beams using chiral photon sieves*, Nano Lett. **20**, 5975 (2020)

M. Solà-Garcia, K. Mauser, N. van Nielen, T. Coenen, S. Meuret, A. Polman, *Pump-probe cathodoluminescence spectroscopy*, ArXiv 2112.03034 (2021)

A. Karnieli, D. Roitman, M. Liebtrau, S. Tsesses, N. van Nielen, I. Kaminer, A. Arie, A.

Polman, *Cylindrical metalens for generation and focusing of free-electron radiation,* Nano Lett. **22**, 5641 (2022)

ACKNOWLEDGMENTS

It feels impossible to condense years of work at AMOLF into just a few pages of acknowledgements. Looking back, I first think of the drama and intensity of lab work, sitting in a dark laser room late into the night, constantly fixing equipment, and fighting to get experiments to work. At some point, the motivation to get through it wasn't earning the doctorate anymore, but the people. This scientific journey mixed into true friendships that I wouldn't trade for an easier job or a smoother journey. You made it worth it and I will miss it terribly, thank you, everybody. There are a couple of people who deserve a special shout-out.

Firstly, **Albert**, thank you for being my supervisor and mentor all these years. You have created such an open and caring working environment, with an emphasis on people and their well-being, but nevertheless leading us to explore new and amazing science through your contagious passion. You have been patient, warm, wise, hardworking, and always happy to provide advice. Your optimism about tough situations often turned out to be right, or perhaps those tough situations worked out because of your undaunted optimism. Thank you deeply for sharing it with me, and for all your support!

Sophie, my co-supervisor, I cannot thank you enough for how much you influenced the success of this thesis. You are so open, helpful, encouraging, passionate, resourceful, and you made me fall in love with science again! You also reminded me that failure is an important part of it, something proven by the three times we wanted to do experiments together but had to cancel because equipment broke ;). I am so happy to have gotten to collaborate with you on so many other projects, and spend time in the lab with you. It was not only great fun, but I learned so much. Thank you.

I want to thank my thesis committee, **Peter Schall**, **Sander Mann**, **Katrien Keune**, **Jacob Hoogenboom**, and **Jonas Lähnemann**, for kindly taking time from their research to evaluate this thesis. I also want to thank Jonas for being one of the spearheads of the CLEBIC community, that organized my favorite conferences I attended during my thesis! I was also lucky to work on a project with a strong user committee. After each of our annual meetings I felt grounded, reinvigorated, and received great advice, so thank you very much to **Toon Coenen**, **Erik Kieft**, **Benjamin Brenny**, and **Marie Anne van de Haar**.

I am extremely proud to say that I got to work with many incredible women in the Polman group (i.e. the "CLadies"), which is a rare thing in physics and gave me such an amazing feeling at work! **Evelijn**, my dear paranymph, and travel buddy. I love you so much! You were always in the office an hour before work started, saying hi, and made it a warm and cozy place. I'm so grateful to have shared so much of my PhD with you, and so many conferences that we milked for the opportunity to go

on a hike. I think you are just an amazing scientist, the best person to rant to and a true friend. The pink office is not complete without **Hollie**, my second paranymph! I almost forget that I was your supervisor as a master student, because to me you are first and foremost a really dear friend. You are so caring, thoughtful, fun, full of energy and happiness, you make the best cakes, share the best fidget toys, and I love how often our thoughts are aligned, and laugh about the same things. Our identical Instagram algorithms are proof of how alike we are. **Saskia**, you are so adventurous, and lovely, and I will never forget how hyped we were about having such a CL expert join the team. Although we both battled through the pain of pump-probe, thankfully we could laugh it off over beautiful trips together and hopefully many more games of Terraforming Mars.

Matthias, you are one of the most special people on this journey. I will never forget all the time we spent together in the lab trying to get PINEM to work, and despite how hard it was it was by far my favourite. You are so funny, and hardworking, and I am so proud of us! I just want to point out that we did still try to have a social life and I enjoyed spending every king's day with you and our NS walks. I miss you in Dortmund, but thankfully **Tomas** came to the group just in time to join in the lab as well, and I am so thankful! Tomas, you really are THE lab cowboy. You taught me how not to be afraid of the machine and are just a ridiculously good experimentalist. You make a mean tiramisu, and know the best places for Indian takeout so I am always up for trying a new recommendation together. **Magda**, I am in awe of you. You built the USEM and, at the end of your PhD, had to teach me all you knew about it (even worse this was during lockdown). And yet you were and still are always so patient and thoughtful and kind. I remember that time so fondly. Even after that, you kept on guiding me in many different ways - thank you so much!

Robin, I already miss seeing you every day! From making me feel like a princess on your boat, to always coming in to the office to cheer us up (i.e. gently distract us), you make people feel like a million bucks around you! Furthermore, you are a really hard worker and a great physicist - I hope you remember that! **Tom**, you are just a famous and irreplaceable LMPVer now, and everyone knows they can always rely on you for help. That's such a beautiful trait, you are a gorgeous human being, and I am so grateful for all the ways I got support from you. I hope some of your peacefulness has rubbed off on me after all these years. **Marco**, although I usually just stare at you across the road in the SolarNL office, I enjoyed every one of our coffees together. You are a very warm and genuine person and I only wish that our offices were closer together. The twins, i.e. **Sam** and **Stan**, I am very thankful to have overlapped with you both in my last stressful months of the PhD, you really helped me with your positive energy. You are both so easygoing, fun, and also so kind! I am sure you will do brilliantly in your PhDs, and are stellar people to kick off the new generation of the Polman group. **Alvaro**, what a treat to have you join the Polman group after many encounters with the rest of the lovely Ebeam community. I love how you are always down to have a great time, and am so happy you too have a passion for the techno biking. Although they have already left the group, I want to thank **Andrea** for all the laughs, drinks, and good times together, **Kelly** for her dry humour and all the

improvements she made on the USEM, **Nick** for his mentorship, and enthusiasm, **Stefan** for being THE example of someone managing to stay chill til the end of the PhD, **Hannah** for being such a prolific master student and always down to hang out outside the lab, **Ana** for all the heartfelt, open talks and encouragement, **Heleen** for being my first ever master student and her patience as we learned on the fly together about many TR-CL experiments, and **Verena** for being a stellar example of a woman in science, with a passion for environment and people.

Beyond the Polman group, we had an entire institute of truly great people, that add up to the "magic" of AMOLF. Firstly I would like to thank the technical support in the Nanolab, **Bob D.**, **Igor**, **Rilda**, in electrical engineering, **Bob K.**, software engineering (and the fun outing planning department), **Ulas**, laser physics, **Jan V.**, and mechanical engineering, **Max P.**, without whom this work would not be possible. Furthermore I want to deeply thank our group technician, **Dion**, who was so smiley, happy to help, and furthermore found ways to help without me having to ask, thank you so much for all your hard work over the years!

I cannot overstate how much fun I had connecting with everyone at AMOLF over our ritualistic morning coffees, regular PV events, weekly colloquia and poster sessions amongst the LMPV and nanophotonics groups, Christmasses, summer schools, and so much more. It is no wonder people outside AMOLF view us as a cult, I will miss it so much! Thank you for all the amazing times to **Ethan K.**, **Loriane M.** (two wonderful office mates), **Esther A. L.**, **Wiebke A.**, **Erik G.**, **Bruno E.**, **Said R.**, **Femius K.**, **Ewold V.**, **Francesca S.**, **Mees D.**, **Sergio R. P.**, **Patrick S.**, **Sarah G.**, **Imme S.**, **Daphne D.**, **Larissa v.d.V**, **Alex L.**, **Daphne A.**, **Antony L.**, **Margarita G.**, **Yorick B.**, **Elaina G.**, **Daan M.**, **Jerome G.**, **Hongyu S.**, **Linde v.d.V**, **Nikolai O.**, **Omalara A.**, **Rohit R.**, **Robin B.**, **Deba P.**, **Masha O.**, **Vashist G.R.**, **Nick F.**, and **Falco B.**. There are many amazing people that I wish I'd had even more time to get to know better.

I want to thank my home away from home. I am so lucky to have lived with amazing housemates on the Molukkenstraat that have given me so much happiness and peace and fun over the years, thank you **Jans**, **Ferran**, and furry little **Alpha**! For all the chill nights, board game nights, movies, swimming, food, friendship, I love you and miss you in the house! Thank you for moving in with me **Esther**, and for being an endless source of positivity and energy! It is wonderful living with you!

Now, this part is impossible to write without crying, I want to thank my family. My caring and strong **Papa**, you taught me how to stand up for myself, gave us a beautiful childhood full of adventure, and inspired me on this career path partly because you told me that physicists will never hurt your feelings. I'm lucky to have a sister in the brave and beautiful **Vani**, who is so patient with me, puts up with me always wanting to hold her hand, and so loyal. Thankfully we will have each others backs until the very end. **Mama**, у меня почти нет слов. Спасибо тебе за всё. Ты самая заботливая и любящая мама, такая сильная, бесконечно терпелива, и такой хороший пример для меня. При этом ты весёлая, болтливая, и я обожаю наши пивные дегустации вместе. Я так сильно тебя люблю и

чувствую, что могу летать от того количества любви, которое ты мне даришь. Finally, I want to thank my partner in everything, **Emil**, the most grounded, sweet, funny, kind person, with whom life is easier, and funner, and better. After ten years together, I know I couldn't have done any of this without your support. I love you!

About the author

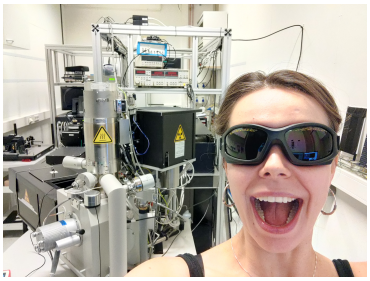

Nika van Nielen was born in Leiden (NL) to Russian and Dutch parents, and grew up moving around the world with her family. Together, they adventured through the Netherlands, Slovakia, Singapore, Cambodia, Russia, Nigeria, and Finland. She always wanted to become a physicist like her grandfather and her father.

After graduating from the International School of Helsinki in 2014, she did volunteer work in Cambodia and then traveled through India. In 2015, she moved to Wales to study Physics at Prifysgol Abertawe, where she met her partner and graduated with a first class degree. She then completed her master's degree in Advanced Matter and Energy Physics at the Universiteit van Amsterdam and the Vrije Universiteit, graduating cum laude in 2020. During her degree, she studied under prof. dr. A. Polman and immediately knew she wanted to work with him. She completed her master's thesis in his group at the research institute AMOLF, on generating vortex cathodoluminescence emission using chiral photon sieve structures. She then continued as a PhD student, working on advanced pump-probe cathodoluminescence techniques for materials analysis and PINEM. The results of this research are shown in this thesis.

To counteract years of back pain-inducing lab work, Nika loves to go bouldering and sweat at a techno bike class. She thinks that constant hand holding and horror movies cure stress, loves to play board games with friends, hike, listen to live music, adventure, and deeply believes in the following quote:

Happiness is only real when shared.

- Christopher McCandless

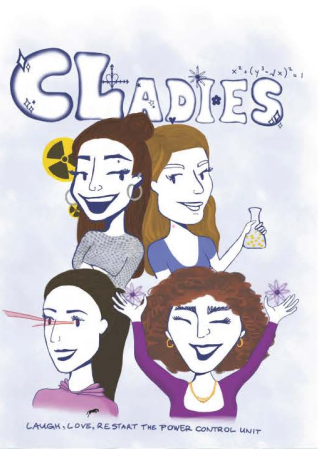
CL LADIES
LAUGH, LOVE, RESTART THE POWER CONTROL UNIT

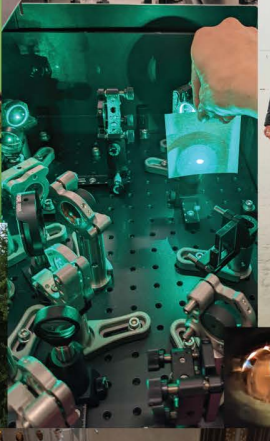


UNI PV

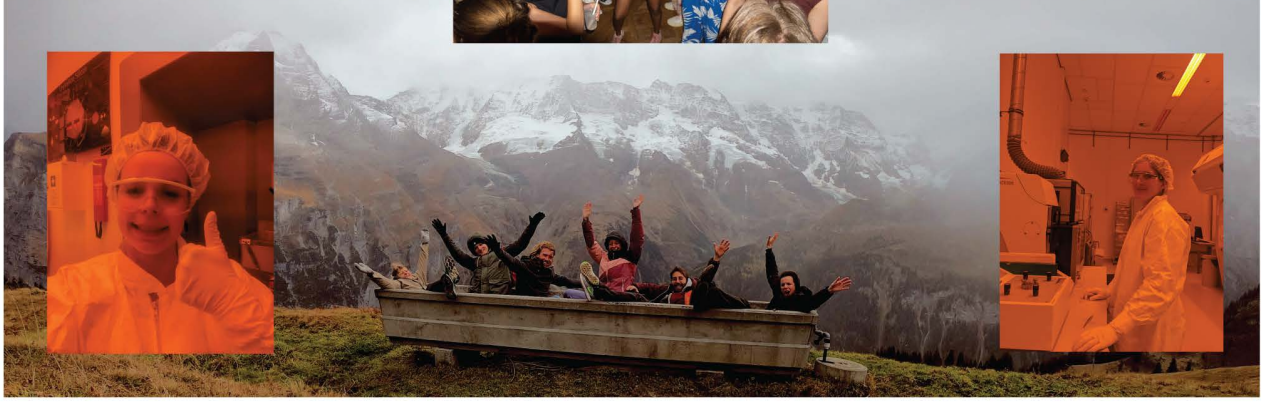

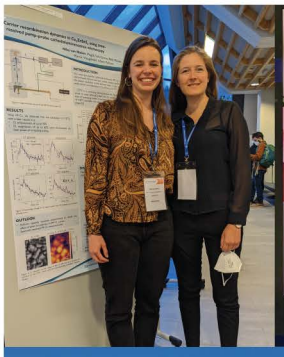




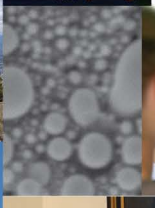







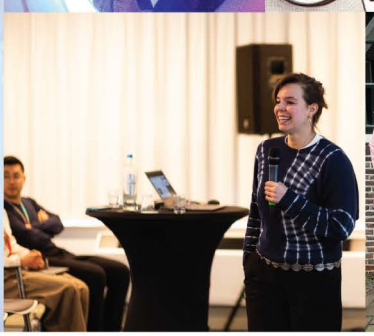






IBM